THE AERODYNAMIC EXCITATION OF TRAPPED DIAMETRAL ACOUSTIC MODES IN RECTANGULAR DUCTED CAVITIES

The Aerodynamic Excitation of Trapped Diametral Acoustic Modes in Rectangular Ducted Cavities

By

MICHAEL BOLDUC, B.ENG & MGT

A Thesis

Submitted to the School of Graduate Studies

In Partial Fulfillment of the Requirements

For the Degree

Master of Applied Science

McMaster University

Master of Applied Science (2015)
Mechanical Engineering

McMaster University
Hamilton, Ontario, Canada

TITLE: The Aerodynamic Excitation of Trapped Diametral Acoustic Modes in Rectangular Ducted Cavities

AUTHOR: Michael Bolduc, B.Eng&Mgt. (McMaster University)

SUPERVISORS: Professor Samir Ziada

NUMBER OF PAGES: xvii, 118

Abstract

The excitation mechanism of trapped diametral acoustic modes within a rectangular cavity-duct system is investigated both numerically and experimentally. The asymmetry inherent within the rectangular geometry introduces a preferred orientation, ensuring the excited diametral modes remain stationary. Three separate cavities are manufactured and tested. This included two asymmetric rectangular cross-sections and one symmetric square cavity.

Experimental results indicate that the aeroacoustic responses of the three cavities are dominated by the strong excitation of trapped diametral modes. Numerical simulations indicate that the resolved radial acoustic particle velocity distributions are non-uniform at the upstream separation edge where the formation of vortical structures is initiated. As the cavity became smaller, and more asymmetric, the trapped nature of the acoustic modes decreased with an accompanied increase in the radiation losses and reduction in pulsation amplitude.

Observations of the aeroacoustic measurements show evidence of three unique modal behaviours. The first case is the independent excitation of a single stationary mode where specific circumferential sections of the shear layer were excited and initiating the formation of vortical disturbances. These circumferential sections, and distribution of disturbances, were akin to the excited mode shape. The second case involved simultaneous excitation of two stationary modes. This suggested that the shear layer was exciting two modes simultaneously. Neighbouring circumferential sections, at the initial region of the shear layer, were being excited independently and at different resonant frequencies. Finally, a spinning trapped acoustic mode was observed in the symmetric square cavity. Due to the spinning nature, the excited circumferential portions and formation of vortices were non-uniform and rotated with the spinning acoustic mode. This resulted in the formation of a three-dimensional helical structure.

ACKNOWLEDGEMENTS

I would first like to thank my supervisor Dr. Samir Ziada for his guidance throughout the years. I remain entirely grateful for his advice and encouragement that has proved invaluable both within this study and within my educational career. For this I remain forever in his debt.

I would like to also extend my gratitude to Philippe Lafon for his additional counsel and suggestions within this current study. As well, I would like to thank all of my colleagues within the Flow Induced Vibration group at McMaster University, past and present, who would always lend a hand when in need. Through their expertise and help in building the experimental test set-up, I extend my gratitude to the technicians within the Mechanical Engineering Department, particularly Michael Lee, John Colenbrander, Mark MacKenzie, Joe Verhaeghe, and Ron Lodewyks.

Last but not least I would like to thank my family and friends, especially Victoria Tran, for their continuous support and motivation which allowed me to overcome the challenges that I encountered throughout these past few years.

NOMENCLATURE

c	Speed of sound	[m/s]
d	Diameter of jet	[m]
D	Pipe diameter	[m]
f	Frequency	[Hz]
f1	Resonant frequency of trapped acoustic mode 1	[Hz]
f2	Resonant frequency of trapped acoustic mode 2	[Hz]
f3	Resonant frequency of trapped acoustic mode 3	[Hz]
f4	Resonant frequency of trapped acoustic mode 4	[Hz]
h	Cavity depth	[m]
H	Cavity cross-sectional height	[m]
K	Adiabatic bulk modulus	[Pa]
L	Cavity length	[m]
$\mathscr{L}$	Pipe length	[m]
m	Diametral mode number for axisymmetric cavity	[]
M	Mach number	[]
n	Free shear layer mode number	[]
P	Acoustic pressure	[Pa]
$\mathscr{P}$	Acoustic power production	[W]
ρ	Density	[kg/m^3]
∇P	Pressure gradient	[Pa]
P^*	Dimensionless acoustic pressure	[]
R_{θ_m}	Reynolds number based on momentum thickness	[]
Re_D	Reynolds number based on pipe diameter	[]
St_{θ_m}	Strouhal number based on momentum thickness	[]
SPL	Sound pressure level ref: 20uPa	[dB]
St_L	Strouhal Number based on cavity length	[]

t	Time	[s]
U_0	Jet centerline velocity	[m/s]
$\vec{U}$	Mean flow velocity vector	[m/s]
$\overrightarrow{U_a}$	Acoustic particle velocity vector	[m/s]
$\overrightarrow{U}_{r_a}$	Radial acoustic particle velocity	[m/s]
$V(z)$	Velocity variation along shear layer	[m/s]
W	Cavity cross-sectional width	[m]
x	Axial distance	[m]
y	Downstream position from upstream corner	[m]
θ_m	Momentum thickness	[m]
θ	Phase along the acoustic cycle of spinning mode	[deg]
∅	Physical angle along the upstream cavity mouth	[deg]
ϕ	PIV temporal phase shifts along acoustic cycle	[deg]
$\vec{\omega}$	Vorticity vector	[1/s]
ω	Angular resonance frequency	[rad/s]
∀	Volume	$[m^3]$

TABLE OF CONTENTS

LIST OF FIGURES

LIST OF TABLES

CHAPTER 1
INTRODUCTION

1.1 Problem and Motivation

Self-sustained oscillations due to flow over cavities have been studied extensively within the literature due to large-amplitude pressure pulsations arising in numerous industrial applications including piping systems, fuselage openings, control valves, jet engines, turbo-compressors, and rocket engines.

The motivation of this study is the occurrence of strong acoustic resonance originating from gate valves present within Boiling and Pressurized Water Reactors (BWRs & PWRs) (Lafon et al., 2003). These gate valves are isolation valves situated along the main stream lines, Figure 1-1, and are used if an incident occurs along the piping (Lacombe et al., 2013). During operation, when the valve is open, the shear layer at the upstream edge may excite the acoustic modes within the enclosed domain, leading to self-excited acoustic resonance.

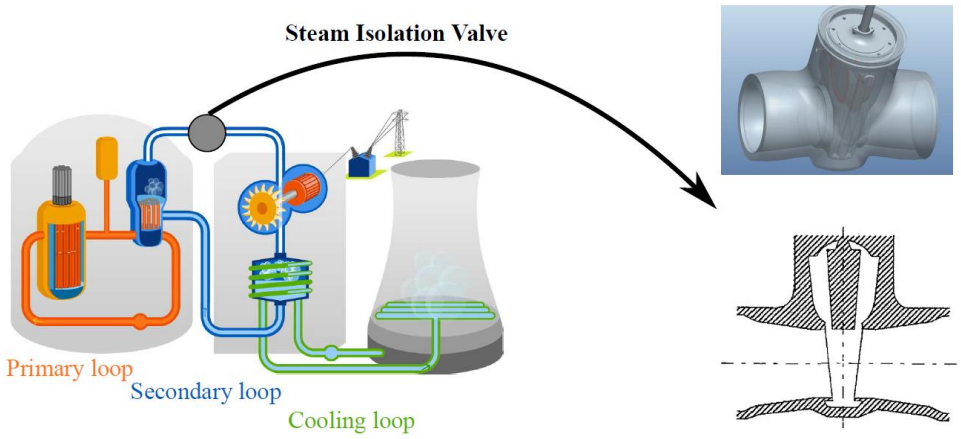

Figure 1-1: Schematic of a PWR plant and its isolation gate valve situated along the main steam line (Lacombe et al., 2013)

In cases of a confined cavity-duct domain, the acoustic modes within the valve may be excited at low flow velocities (M <0.3) and consist of very strong

pressure pulsations. These acoustic modes are referred to in the literature as being "trapped' as the acoustic energy is confined within the valve geometry with negligible radiation being emitted down the attached piping (Hein & Koch, 2008; Aly & Ziada, 2010). The excitation of these trapped acoustic modes can lead to disastrous results. In the tests conducted within this thesis, amplitude levels of 174dB (ref: 20uPa) were commonly measured at the anti-nodes of the excited acoustic modes. Within industry, these amplitude levels exceed the limits of noise regulations and pose a serious safety concern to workers on site (Smith & Luloff, 1999). Also, these strong pressure oscillations may lead to fatigue failure both within the valve and in nearby piping and supports (Ziada & Bühlmann, 1989; NRC, 2002).

As well, the pressure drop across the valve increases during acoustic resonance, an effect demonstrated in the experimental results found in Appendix A. The kinetic energy from the mean flow is now being used to sustain the strong acoustic resonance. This leads to undesirable economic effects as it reduces the overall efficiency of the plant. A BWR power plant consists of numerous steam lines, each consisting of its own isolation valves. Thus, the excitation of more than one of these isolation valves in unison is possible, potentially escalating each of these associated problems.

The general excitation mechanism is due to an interaction between flow instabilities at the upstream edge and the acoustic mode's resonant sound field. The instability of the shear layer causes the disturbances to amplify downstream into large vortical structures. These structures then impart energy into the resonant sound field, strengthening the acoustic pressure oscillations. The velocity fluctuations from the acoustic particle velocity then initiate the formation of larger disturbances at the upstream edge, closing the feedback cycle.

The excited acoustic modes within the gate valve domain are the transverse diametral modes. Unlike longitudinal acoustic modes, these mode shapes are

three-dimensional within the cavity geometry. This leads to a non-uniform interaction between the shear layer instability and the acoustic particle velocity. Previous studies investigating the excitation mechanism of trapped diametral modes (Aly & Ziada, 2010), their azimuthal behaviour (Aly & Ziada, 2011), the effect of mean flow (Aly & Ziada, 2012), and passive mitigation techniques (Bolduc et al., 2014) have focused on axisymmetric cavity-duct geometries. However, the existence of an asymmetric acoustic mode within an axisymmetric geometry resulted in the acoustic modes having no unique orientation. As such, they tended to spin about the pipe's axis at their resonant frequency.

The cavity geometries for industrial gate valves are generally not axisymmetric; therefore the diametral acoustic modes are stationary. The present study considers such a case, where the asymmetry of the rectangular cross-sectional geometry specifies one unique orientation for each of the excited diametral acoustic modes. This simplified model allows one to experimentally investigate the complex three-dimensional interaction between the non-uniform acoustic particle velocity distribution at the shear layer and its propagation of vortical structures. As well, the presented experimental results may be used to validate numerical simulations which are used to predict the aeroacoustic characteristics of these excited diametral acoustic modes.

1.2 Thesis Layout

This thesis is composed of four separate chapters. Chapter 2 presents a literature review on the excitation of trapped diametral acoustic modes. First, an overview of free shear layer instabilities and its interaction with the fluid-resonant feedback mechanism is covered. An assortment of self-sustaining cavity oscillations is then investigated before focusing on the current case of trapped diametral acoustic modes. A review of recent studies on trapped diametral modes within axisymmetric cavities is presented, including the influence of symmetry and current mitigation techniques. Finally, the objectives of the current study are stated.

Chapter 3 details the experimental facility and test setup used in investigating the excitation mechanism of trapped diametral modes within rectangular cavities. The test-setup consists of three separate cross-sectional cavities, one which is square while the other two are rectangular. Numerical simulations of the acoustic mode shapes and their radial acoustic particle velocity distributions are presented along with the instrumentations used.

Chapter 4 presents the experimental results utilizing the experimental facility from Chapter 3. The aeroacoustic responses of the trapped acoustic modes, for each of the three tested cavities, are presented and compared. Emphasis is then placed on the complex flow-acoustic coupling of three observed modal behaviours. The analysis consisted of comparing the resolved radial acoustic particle velocity to the corresponding vortical structures along the circumference of the shear layer. Qualitative flow visualization of these structures was done through phase-averaged Particle Image Velocimetry. Finally, Chapter 5 provides a summary of the work along with suggested improvements on current passive suppression methods.

CHAPTER 2
LITERATURE REVIEW

2.1 Introduction

The following chapter presents a literature review on the acoustic resonance of trapped diametral acoustic modes within cavities. The chapter begins with the general excitation mechanism of self-sustained cavity oscillations, including the interaction between the flow instability at the upstream cavity corner, and an upstream propagating feedback mechanism.

The fluid-resonant feedback mechanism is a result of the acoustic particle velocity imparting velocity fluctuations at the upstream separation edge of the cavity, initiating and strengthening disturbances into large vortical structures. This closes the feedback cycle. Depending on the acoustic mode shape, the acoustic particle velocity distribution and formation of disturbances can vary along the associated shear layer. Recent studies have focused on trapped diametral modes within axisymmetric cavities.

The investigated acoustic modes are the diametral modes confined within cavities. These confined modes are defined as trapped and consist of negligible radiation and high pulsation amplitudes. Unlike longitudinal modes, the acoustic properties of the diametral modes vary in the azimuthal direction. This leads to a non-uniform particle velocity distribution and excitation mechanism along the shear layer circumference. This non-uniformity may lead to different azimuthal behaviours depending on the inherent symmetry of its associated geometry, further complicating the excitation mechanism. Active and passive mitigation methods for diametral modes, when avoidance is not possible, are then discussed. Finally, objectives of the study are presented in regards to the current state of knowledge.

2.2 The Instability of Free Shear Layers

A fluid flow is characterized as unstable when an introduction of a small disturbance, or perturbation, may be amplified into large vortical structures as the flow is convected downstream. Flow instabilities are commonly found in free boundary layer flows including wakes, jets, and free shear layers/mixing layers.

The free shear layer, whose progression of disturbances is illustrated in Figure 2-1 (Chevray, 1984), is a result of the merging of fluid streams at two constant, yet independent, mean flow velocities. The amalgamation of these two velocities creates a velocity gradient, or shear, which has an inflexion point. As investigated by Tollmien (1935) and Rayleigh (1880), this inflexion point is a sufficient condition for flow instability in two-dimensional inviscid flows. The flow structure begins as a small disturbance, growing into organized vortical structures. These large scale structures then amplify in a nonlinear fashion, become three-dimensional, coalesce and break down into turbulence.

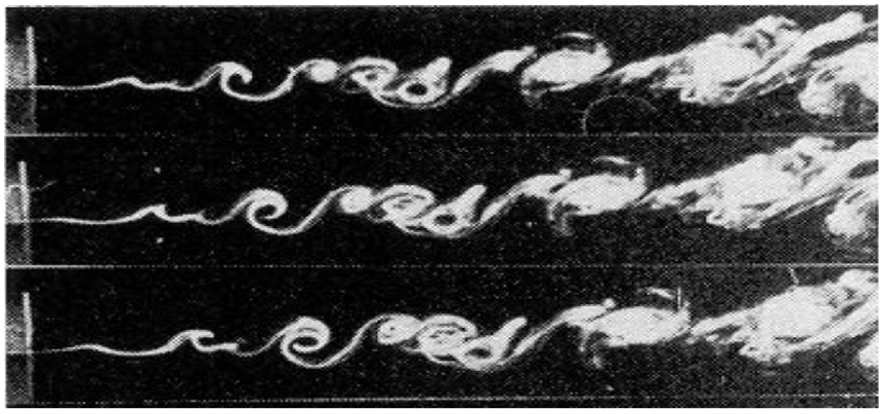

Figure 2-1: Development and breakdown of disturbances within a free shear layer (Chevray, 1984)

The linear stability inviscid model, proposed by Lord Rayleigh, successfully predicted the initial linear growth for small disturbances, as well as the frequencies at which the shear layer was unstable (Rayleigh, 1880). The linear inviscid instability model was exercised on a dimensionless hyperbolic-tangent

velocity profile, illustrated in Figure 2-2, by Michalke (1964, 1965). This free shear layer velocity profile is consistent with that of flow over a cavity, where the merging of two fluid streams (one with zero velocity) is due to the sudden separation at the upstream edge of the cavity mouth.

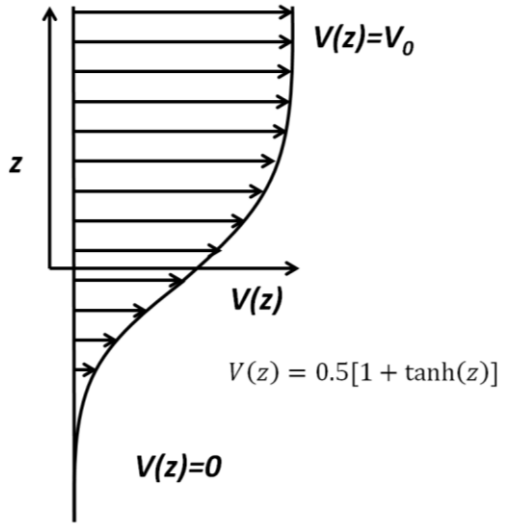

Figure 2-2: Hyperbolic-tangent velocity profile utilized by Michalke (1964, 1965) reminiscent of an unstable free shear layer within grazing cavity flows

Michalke analyzed both the temporal and spatial growth rates of the disturbances, demonstrating that only at a specific range of frequencies is the flow unstable. Those frequencies outside this range were stable. Likewise, experiments conducted on laminar planar and axisymmetric jets by Freymuth (1966), investigated the spatial growth within the linear region by varying specific parameters through the external excitation of a loudspeaker.

Figure 2-3 illustrates the influence of the external forcing amplitude on the initial growth rate, represented by the slope. Although defined as a linear trend, the initial growth rate is exponential, with the linearity being observed on a logarithmic scale. To analyze the growth rate of the disturbances, Freymuth utilized a hot-wire probe to measure the velocity fluctuations as the flow is convected downstream. Increasing the external disturbance amplitude, via the acoustic pressure, simply resulted in larger initial disturbances being situated

farther upstream. In each of these tests, however, the growth rate remained constant until the dimensionless velocity fluctuations saturated at an amplitude of ≈ 0.2, coinciding to the onset of the nonlinear growth regime.

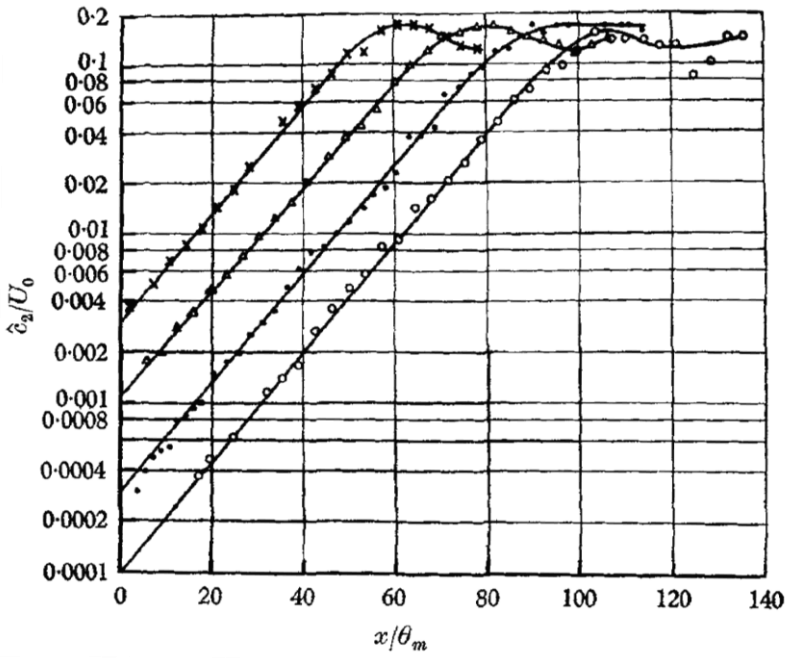

Figure 2-3: Effect of acoustic pressure on the downstream growth of velocity fluctuations from an axisymmetric jet, ○=70dB, ●=80dB, Δ=90dB, X=100dB, d=7.5cm, U_0=8.0m/s, R_{θ_m}=122, St_{θ_m}=0.0118 (Freymuth,1966)

Likewise, the effects of excitation frequency on the initial linear growth rate of the disturbance was also investigated, Figure 2-4. The frequency is represented via the dimensionless Strouhal number defined by:

$$St_{\theta_m} = \frac{fL}{U} \tag{2.1}$$

The characteristic length, L, is represented by the momentum thickness, θ_m, and the flow velocity, U, is represented by the jet flow velocity U_0. The results demonstrate that variations in the Strouhal number had a prevailing effect on the initial growth rate within the linear regime. The maximum rate of growth occurred at a Strouhal number of around 0.0167, with the growth rate decreasing with Strouhal numbers that further deviated from this value. These results were

consistent with the analysis reported by Michalke. It suggested that there is a specific band of frequencies at which the amplification of the initial disturbances is significant. If the frequency imparted on the flow was much higher or lower than this frequency range, the system would become damped and the associated flow would become stable.

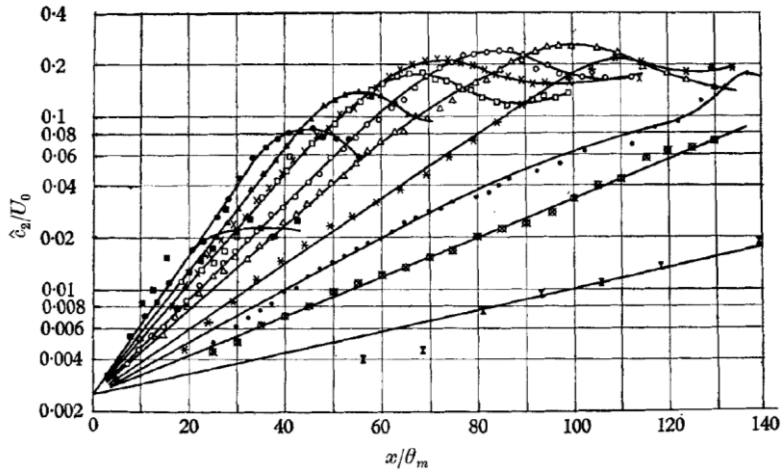

Figure 2-4: Effect of Strouhal Number on the downstream growth of velocity fluctuations of an axisymmetric jet, ⧗, St_{θ_m}=0.0020, ⊗, St_{θ_m}=0.0040, ●, St_{θ_m}=0.0050, ✳, St_{θ_m}=0.0070, Δ, St_{θ_m}=0.0080, ○, St_{θ_m}=0.0090, X, St_{θ_m}=0.0100,□, St_{θ_m}=0.0118, ▲, St_{θ_m}=0.0148, ●, St_{θ_m}=0.0176, ■, St_{θ_m}=0.0234 d=7.5cm, U_o=16.0m/s (Freymuth, 1966)

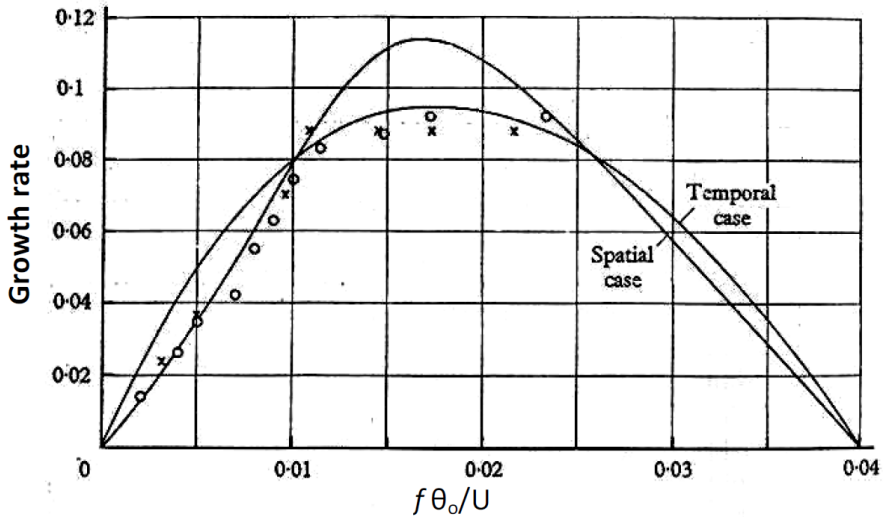

Figure 2-5: Comparison of numerical and experimental growth rates as a function of St_{θ_m} for axisymmetric,○, and planar, X, free jets (Freymuth, 1966)

A comparison of Freymuth's experimental results with Michalke's numerical analysis is shown in Figure 2-5, (Freymuth, 1966). As illustrated, the spatial theory showed a better agreement for lower Strouhal numbers and the temporal theory is preferred at higher Strouhal numbers. For both numerical and experimental results, the laminar shear layer is most unstable at a Strouhal number of around 0.0167. Past a Strouhal number of 0.025, it was not possible to excite the jet, hence the lack of experimental data.

The previously mentioned studies utilized linear theory to represent the initial exponential growth rate of small perturbations as they travel downstream. However, as the velocity fluctuations of the disturbance grow beyond 3.0% of the mean flow velocity, the linear theory becomes invalid and the amplification of the disturbance become highly nonlinear. This was observed by Miksad (1972) who detected the emergence of numerous subharmonic velocity oscillations being generated within the nonlinear regime and becoming amplified exponentially.

Initially, the fundamental mode was the most unstable and grew in a manner consistent to the previously discussed linear inviscid model. Once saturated at its maximum amplitude, its growth rate declined and the subharmonic growth rate became dominant. This growth of the subharmonic is due to a merging process of two consecutive vortices coalescing into one, resulting in velocity fluctuations at half the fundamental frequency (Ho & Huang, 1982). The presence of the remaining subharmonic components consists of a similar process differing by the amount of consecutive merging vortices.

2.3 Classification of Feedback Mechanisms

Cavity oscillations are caused by the interaction of the flow instability of the free shear layer and a feedback phenomenon, essentially an upstream propagating disturbance that amplifies and excites new disturbances at the upstream edge of the cavity. Self-sustained cavity oscillations follow a similar sequence of events as displayed in the flowchart in Figure 2-6.

Initially, perturbations are introduced within the shear layer, whether it is from an external excitation or from broadband turbulent fluctuations. Due to the flow instability, these disturbances roll up and amplify downstream eventually forming large vortical structures. Once the vorticity perturbations are convected by the mean flow to the downstream corner, a feedback phenomenon closes the cycle and introduces a new disturbance at the upstream edge. Depending on the underlying physics of the self-sustaining oscillation under investigation, the feedback mechanism may differ.

Rockwell & Naudascher (1978) categorized cavity oscillations into three groups, based on the nature of the feedback mechanism driving the oscillations. These were defined as fluid-dynamic, fluid-elastic, and fluid-resonant.

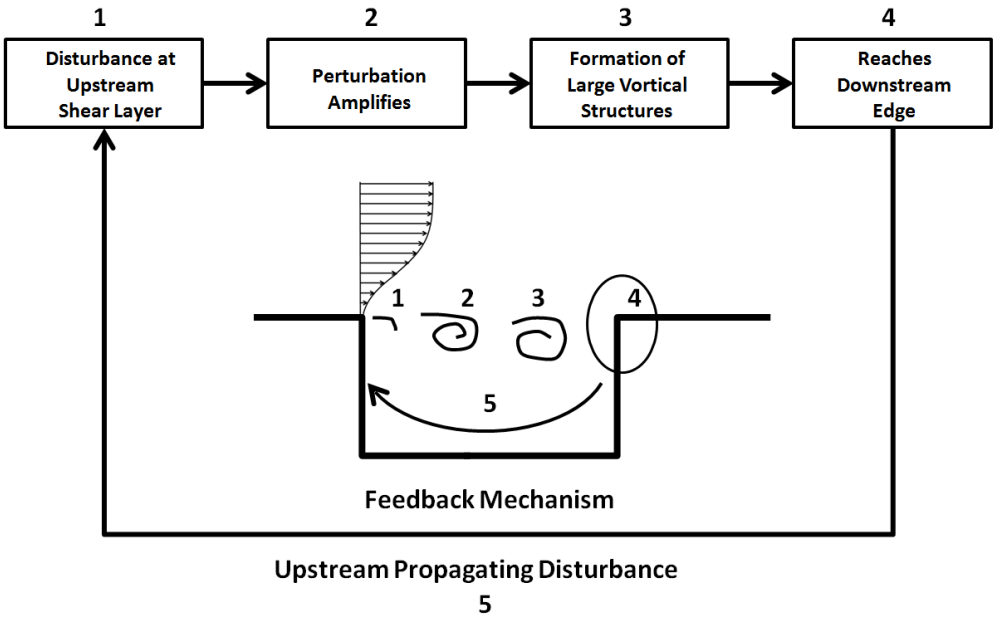

Figure 2-6: Flowchart illustrating the general sequence of events within self-sustained cavity oscillations

The fluid-dynamic feedback mechanism is due to the impingement of vortical structures on the downstream cavity edge and occurs in the absence of resonance effects. This interaction at the downstream edge generates acoustic waves which propagate upstream towards the shear layer. These pressure perturbations produce fluctuations of vorticity at the upstream shear layer,

enhancing the disturbances and closing the feedback cycle. Based on the events of this mechanism, the popular semi-empirical model initially proposed by Rossiter (1964) has successfully predicted the oscillation frequencies at moderate subsonic to supersonic velocities (Heller & Bliss 1975; Tam & Block 1978).

Fluid-elastic feedback occurs when the cavity walls are flexible and oscillate at a frequency within the most unstable frequency range of the free shear layer. The displacement of the walls and the shear layer oscillations synchronize closing the feedback cycle.

The fluid-resonant feedback mechanism arises from the coupling of the shear layer instability with the resonant sound field. The acoustic particle velocity fluctuations, belonging to an excited acoustic mode, interact with the shear layer and enhance the initial perturbations into large coherent vortical structures. The vortical structures are then convected downstream by the mean flow velocity, generating acoustic energy and sustaining the acoustic resonance. The fluid-resonant feedback mechanism generates very strong and coherent shear layer oscillations that can occur much closer to the upstream cavity edge in comparison to the fluid-dynamic mechanism (Rockwell, 1983).

Examples of self-sustaining cavity oscillations, corresponding to each of the three feedback mechanisms, are shown in Figure 2-7. Although designated into three distinct groups, it is possible to have a combination of these mechanisms concurrently within an application (Rockwell & Naudascher, 1978; Betts, 1972). Nonetheless, emphasis is placed on the fluid-resonant feedback mechanism as it is dominant in the excitation of the trapped diametral acoustic modes, the focus of this thesis.

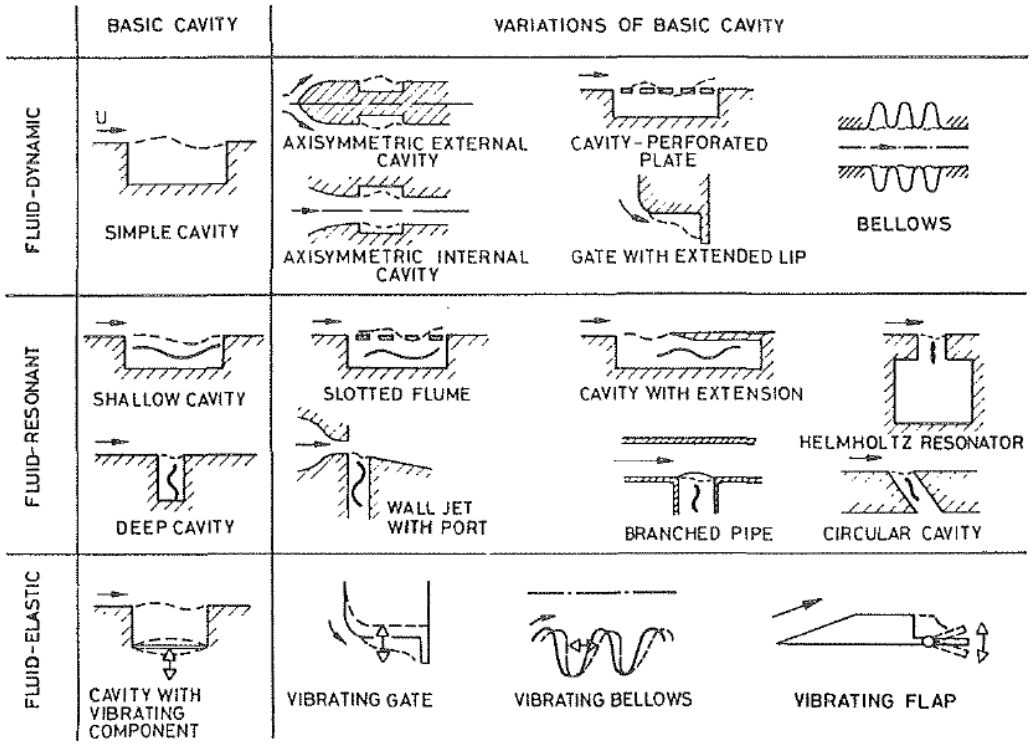

Figure 2-7: Common cavity oscillations categorized into the fluid-dynamic, fluid-resonant and fluid-elastic feedback mechanisms (Rockwell & Naudascher, 1978)

2.4 Acoustic Modes of Self-Sustaining Cavity Oscillations

The fluid-resonant feedback mechanism is highly dependent on the acoustic particle velocity and its interaction with the upstream shear layer. The distribution and strength of the acoustic particle velocity fluctuation is a direct result of the excited acoustic mode. A parameter that influences the shape of the excited acoustic mode is the comparison of the depth, h, to the length, L, of the cavity. Cavity geometries can be categorized into two types, shallow and deep, depending on this geometric ratio (Rockwell & Naudascher, 1978).

Self-sustaining acoustic resonance at low flow velocities of shallow cavities, $L/h>1$, often involve the excitation of longitudinal acoustic modes situated along the length of the cavity and the associated duct. Previous studies investigating oscillations of unconfined shallow cavities mostly focus on higher Mach numbers, $M>0.4$ (Rossiter, 1964; Heller & Bliss, 1975). This is due to the large amounts of

radiation present within the cavity domain. The system requires more energy from the grazing flow in order to overcome the radiation and to sustain the cavity oscillations (Tam, 1976).

However, shallow cavities have been observed to excite acoustic modes at lower subsonic Mach numbers when attached to a confined domain. The flow instability at the mouth of shallow cavity acts as a source to the excitation of acoustic modes inherent within the attached geometry. Experiments conducted by Huang & Weaver (1991) and Rockwell & Schachenmann (1980) have illustrated that shallow axisymmetric cavities can excite the longitudinal acoustic modes situated within its attached piping. In the case of deep cavity geometries, $L/h<1$, it is primarily the transverse acoustic modes within the cavity volume that are being excited by the shear layer instability.

Additionally, confined shallow cavities exposed to high flow velocities have been observed to excite the transverse acoustic modes within a cavity-duct domain (Keller & Escudier, 1983; Ziada et al., 2003). In the latter case, excitation of the transverse acoustic modes were observed at relatively low flow velocities, $M<0.3$. This introduction of confinement to a shallow cavity led to the local acoustic energy becoming bound within the geometric domain, resulting in strong pulsation amplitudes and negligible radiation. These acoustic modes are commonly referred to in literature as being "trapped" (Evans et al., 1994; Duan et al., 2007; Hein & Koch, 2008).

2.4.1 Trapped Acoustic Modes

The existence of unique acoustic modes consisting of zero radiation losses was first established by Evans & Linton (1991). These trapped acoustic modes emerge in wave guides when there in an abrupt change in fluid properties or in domain geometry (Evans et al., 1994). Within a confined cavity-duct system, the sudden change in geometry at the junction of the cavity and duct lowers the local cut-off frequency of the cavity to be below that of the duct. This introduces a new

resonant mode within the system. Since the duct has a higher cut-off frequency, the acoustic energy associated with the cavity does not propagate upstream and downstream along the wave guide/duct (Kinsler et al., 2000).Therefore, when the mode is excited, the acoustic energy becomes confined within the cavity domain resulting in negligible acoustic radiation and strong pulsation amplitudes.

The properties of these trapped modes were investigated numerically for two dimensional systems at zero-flow conditions including butterfly and ball-type valves (Duan et al., 2007). As well, further simulations indicated the existence of these trapped acoustic modes for cavity configurations housed in infinitely long cylindrical pipes (Hein & Koch, 2008). In these cases, the amplitude of the transverse wave decayed exponentially in the axial direction away from the cavity domain. Within confined cavity-duct geometries, (Keller & Escudier, 1983; Ziada et al., 2003), the excited trapped acoustic modes are the diametral, or cross-modes, of the cavity domain. In the rest of this thesis, these trapped cross-modes will be referred to as "diametral modes" even though the cavity geometry is not cylindrical in many cases.

The trapped acoustic modes are of practical importance for industrial applications. This is because they can be easily excited at relatively low flow velocities. This results in low acoustic losses and exceedingly dangerous noise levels. In particular, the abrupt geometric changes accompanying valve configurations have made them especially susceptible to strong acoustic excitation due to the resonance of trapped diametral modes. Ziada et al. (1989) observed the excitation of diametral modes housed within the valve chest of a by-pass control valve. Likewise, Smith & Luloff, (2000) observed strong acoustic resonance of the first diametral mode present at the throat of 25 separate gate valve configurations. As well, Lafon et al. (2003) observed the presence of large amplitude oscillations within a steam line that had originated from an open gate valve. Recent studies investigating the excitation of trapped diametral acoustic

modes have focused on simplified gate valve geometries, particularly axisymmetric cavity-duct domains.

2.4.2 Axisymmetric Cavities

Aly and Ziada, (2010) numerically and experimentally investigated the excitation mechanism of trapped diametral acoustic modes present within axisymmetric cavities attached to a piping domain. Tests were conducted on various cavity dimensions, Figure 2-8, altering the ratios of cavity length to depth (L/h) and cavity depth to pipe diameter (h/D). The attached piping remained the same for all variations, with an inner diameter of 152.4mm and a length, $\mathcal{L}$, of 450mm attached to both ends of the cavity.

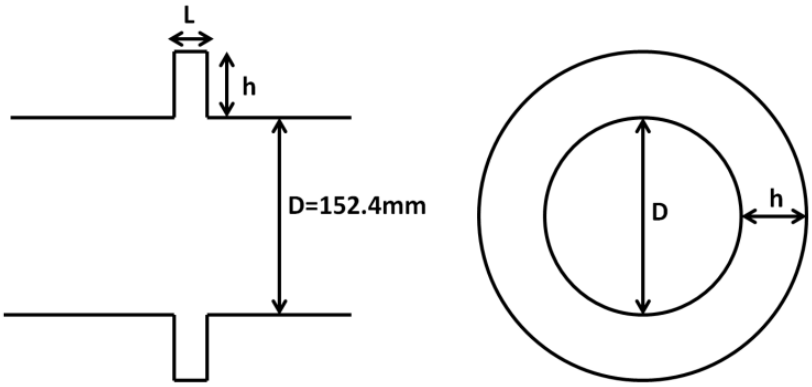

Figure 2-8: Schematic of axisymmetric cavity-duct domain with corresponding dimensions

An example of the first three resolved trapped diametral acoustic mode shapes for an axisymmetric cavity is displayed in Figure 2-9. The associated diametral mode shapes differ substantially to that of longitudinal acoustic mode, whose acoustic properties only vary in the axial direction. Along the cross-section A-A of the cavity, the acoustic pressure varies azimuthally along the cavity perimeter. The acoustic mode order, m, corresponds to the number of complete sine cycles along the circumference of the cavity perimeter as well as the number of nodal lines separating the anti-nodes, or regions of maximum acoustic pressure.

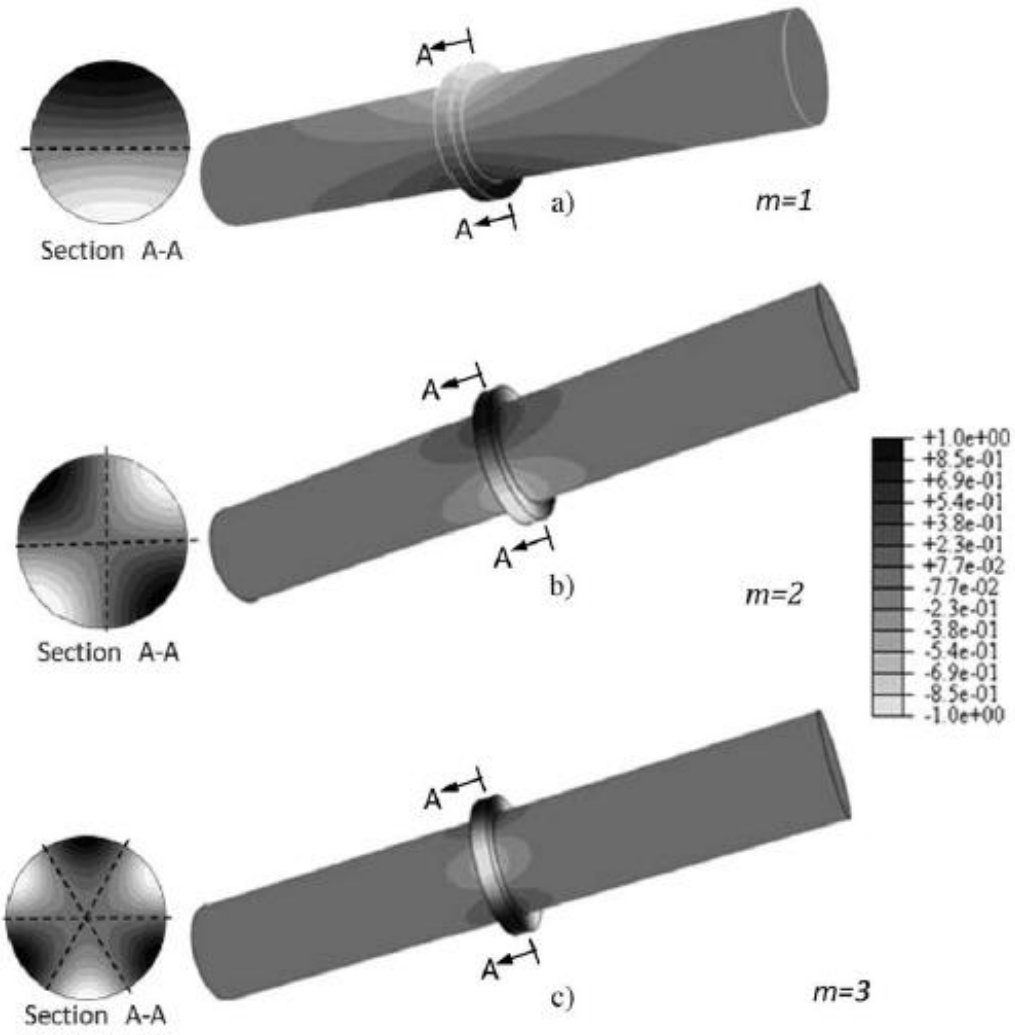

Figure 2-9: Trapped acoustic mode shapes for the first three diametral modes for the L/h=1, h=25.4mm, axisymmetric cavity (Aly & Ziada, 2010). The dotted lines represent the nodal lines.

As illustrated, the acoustic pressure and energy for each of the simulated mode shapes were highly localized within the cavity domain representing a nearly trapped acoustic mode. As the order of the mode increases, observations indicated that the acoustic energy becomes further confined to the cavity domain. Aly and Ziada conducted additional simulations by varying cavity dimensions, Figure 2-10, to explore the trapped nature of the simulated modes by observing the axial decay of the acoustic pressure for each cavity.

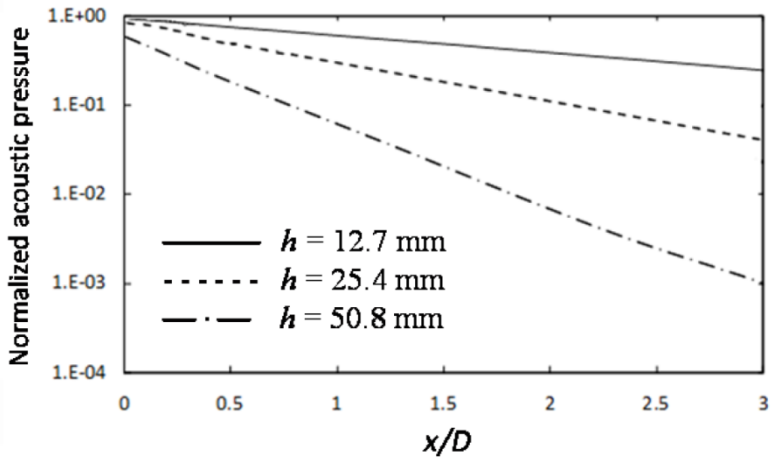

Figure 2-10: Exponential decrease in acoustic pressure of the first diametral mode with axial distance from the cavity domain for varying depths, h, for axisymmetric cavities (Aly & Ziada, 2010)

As indicated from the simulations, the acoustic pressure decreased exponentially in the axial direction away from the cavity, consistent to the numerical work of Hein & Koch, (2008). This decay represents the degree of confinement of acoustic energy within the cavity domain. A higher axial decay in acoustic pressure represents more acoustic energy being localized within the cavity domain, instead of radiating outwards from the ends of the pipes. Comparisons of the different cavity geometries show that the axial decay, and the trapped nature of the acoustic modes, increases as the cavity depth, h, gets larger. This is due to a larger variation between the resonant frequency of the acoustic mode and the cut-off frequency of the duct (Kinsler et al., 2000).

Aeroacoustic measurements were conducted for each of the cavity geometries at incremental flow velocities up to around 140m/s. Two aeroacoustic responses of equivalent length axisymmetric cavities, varying only by the depth, are displayed in Figures 2-11 and 2-12. The responses correspond to depths, h=12.7mm and h=50.8mm and represent the Sound Pressure Level of each of the four diametral acoustic modes along their velocity range of excitation.

The aeroacoustic responses of these axisymmetric cavities were clearly dominated by the presence of the simulated diametral trapped modes, which were

excited strongly at Mach numbers as low as 0.1. As the depth of the cavity increased, the pulsation amplitudes of the excited modes became substantially stronger, as indicated by the increase of SPL from 170dB to 180dB. This influence of depth on the aeroacoustic response is consistent with the increased trapped nature of the acoustic modes resolved from the numerical simulations. Additionally if the length of the cavity increased, with cavity depth remaining constant, the acoustic pressure decreased.

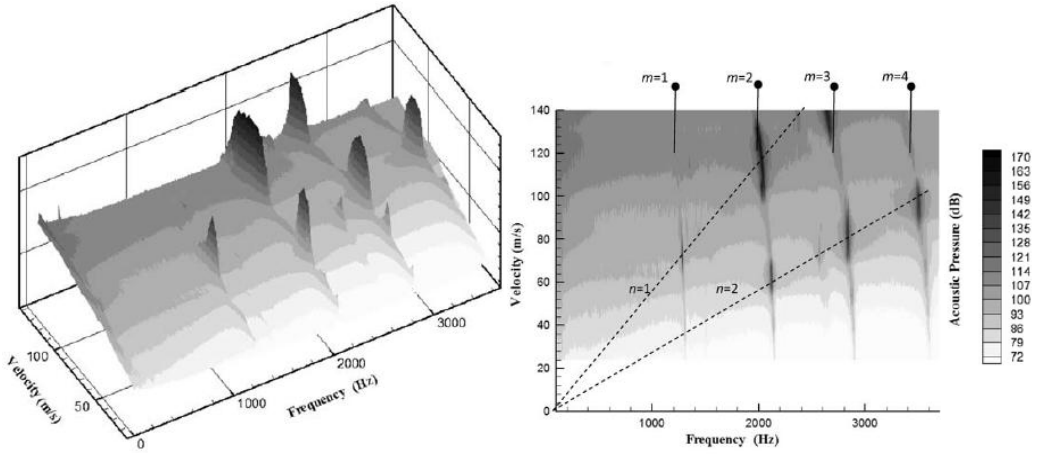

Figure 2-11: Waterfall SPL contour plot detailing the aeroacoustic response of the trapped diametral modes for the h=12.7mm, L/h=2 axisymmetric cavity (Aly & Ziada, 2010)

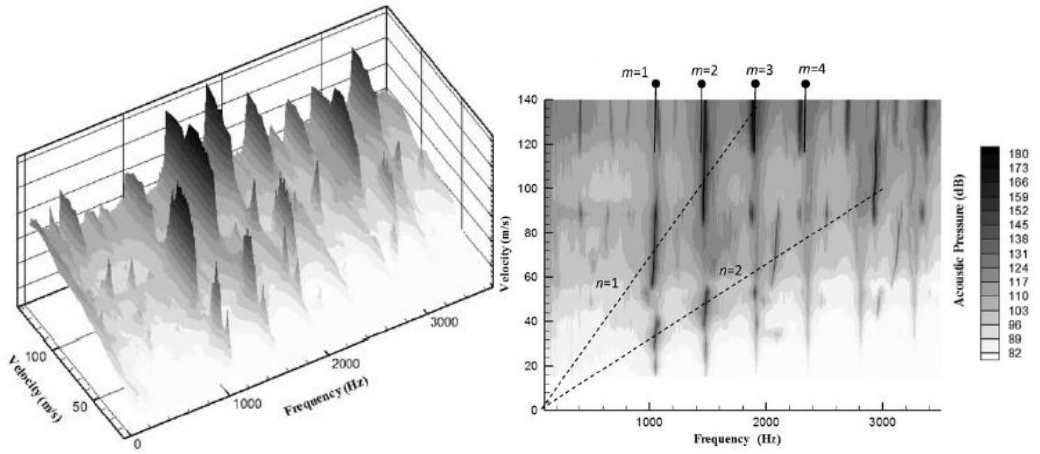

Figure 2-12 Waterfall SPL contour plot detailing the aeroacoustic response of the trapped diametral modes for the h=50.8mm, L/h=0.5 axisymmetric cavity (Aly & Ziada, 2010)

Additional variations of geometry, specifically in the vicinity of the cavity domain, can affect the trapped nature of the acoustic modes. Experimental tests conducted by Barannyk & Oshkai (2014) investigated the diametral modes within an axisymmetric cavity situated in the middle of a converging-diverging section attached to a larger diameter piping domain. This geometry is commonly found in control gate valve assemblies within industry. As the angle of the convergence-divergence section increased, the pulsation amplitudes of the acoustic modes decreased substantially. Observations of the simulated mode shapes indicated an increase in acoustic radiation through the attached piping, resulting in a reduction in the trapped nature of the acoustic modes.

The simulated mode shapes and resonant frequencies, Figure 2-9, were computed at zero flow velocity conditions. Further numerical simulations, (Aly & Ziada, 2012), investigated the effect of mean flow on both the resonant frequencies and mode shapes of the trapped diametral modes. Results indicated the resonant frequencies decreased slightly with a corresponding increase in Mach number. As well, the mode shape became more concentrated to the downstream edge of the cavity, modulated to that of convected flow velocity. Additional evidence illustrated that the acoustic particle velocity amplitude at the cavity mouth was largely influenced by this variation in the mode shape. However, both these variations in acoustic pressure and particle velocity were shown to be independent of the azimuthal angle.

2.5 Fluid-Resonant Excitation Mechanism

The fluid-resonant excitation mechanism is driven by the interaction between the flow instability at the upstream cavity edge and the acoustic particle velocity fluctuations introduced by the resonant sound field. These velocity fluctuations initiate the growth and amplification of the perturbations all along the shear layer circumference. Howe's aerodynamic theory of sound approximates the acoustic power production, $\mathscr{P}$, from the interaction between the parameters of the

flow field, via the vorticity vector, $\vec{\omega}$, and mean flow velocity vector, $\vec{U}$, with the resonant sound field, via the acoustic particle velocity, $\overrightarrow{U_a}$ (Howe, 1980).

$$\mathcal{P} = -\int (\rho \int \vec{\omega} \cdot (\vec{U} \times \overrightarrow{U_a})\, d\forall) dt \tag{2.2}$$

The determination on whether the acoustic resonance is self-sustaining depends on the sign of the integrated power over one acoustic cycle. If the amount of energy that is transferred to the resonant sound field is larger than that absorbed by the vortical structure along one acoustic cycle, then the integrated acoustic power is positive and resonance is self-sustaining. An illustration of this energy exchange is represented in Figure 2-13 (Ziada, 2010), corresponding to a transverse standing wave within a deep cavity.

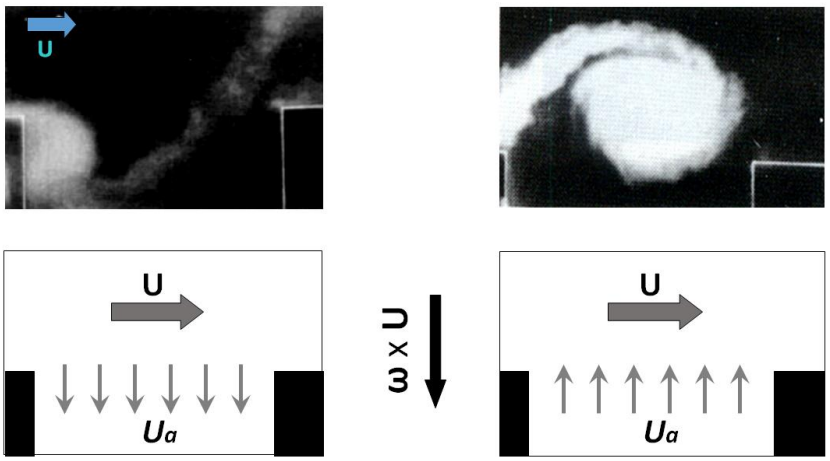

Figure 2-13: Illustration detailing the energy exchange between the flow field and the resonant sound field during an acoustic cycle of a transverse acoustic mode in a deep cavity (Ziada, 2010)

At the beginning of the acoustic cycle, during the initial vortex rollup, the acoustic particle velocity is directed towards the cavity walls. Here, the acoustic energy is being absorbed by the vortical structure, as depicted by its amplification. It is at this location, where the acoustic particle velocity is most *dominant* in the initiation and formation of the vortical disturbances. Further downstream, and later in the acoustic cycle, the acoustic particle velocity is now acting outwards towards the centerline of the pipe. At this point in the cycle, the vortical structure

is now generating acoustic energy to sustain the resonant sound field. In this example, the generation of acoustic energy is larger than that absorbed by the vortical structure, indicating a self-sustained oscillation. As will be discussed later in this review, this energy exchange may not be synchronized/uniform along the circumference of the shear layer depending on the excited mode shape and acoustic particle velocity distribution.

2.5.1 Hydrodynamic Modes or Free Shear Layer Modes

The described energy transfer between the propagating disturbances and acoustic particle velocity occurs all along the impingement/cavity length. In order for acoustic resonance to be sustained, a specific phase condition between these two components must be satisfied. This is to ensure that the vortical structure is amplified at the upstream edge and that it generates acoustic energy further downstream.

The fulfilment of this phase constraint can occur at different shear layer oscillation patterns, corresponding to a varying number of vortices being propagated along the cavity length. These oscillation patterns are defined free shear-layer modes, whose modal number, n, designates the number of vortices present along the cavity length during an acoustic cycle. These shear layer oscillations occur at well-defined frequencies, described by their dimensionless Strouhal number shown below, where f represents the respective oscillation frequency, L represents the cavity length, and U represents the mean flow velocity.

$$St_L = \frac{fL}{U} \tag{2.3}$$

In the previous case of the h=50.8mm, L/h=0.5 axisymmetric cavity, Figure 2-12, the trapped diametral acoustic modes were excited by the first two free shear layer modes, n=1 and 2, consisting of one or two vortices propagating along the cavity length. Figure 2-14 displays the dimensionless acoustic pressure for this

cavity geometry and its associated Strouhal number for each of the three diametral modes during its velocity range of excitation (Aly & Ziada, 2010).

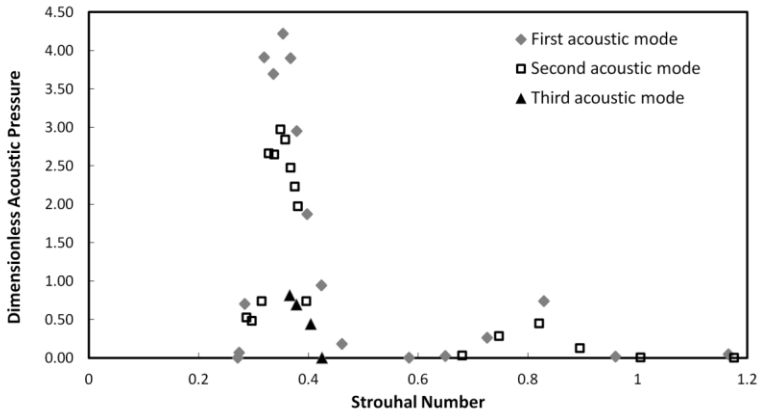

Figure 2-14: Relationship of dimensionless acoustic pressure and Strouhal number during the excitation of the three diametral trapped acoustic modes, h=50.8mm, L/h=0.5 axisymmetric cavity (Aly & Ziada,2010)

As indicated, the Strouhal numbers lie within two distinct ranges, corresponding to each of the hydrodynamic shear layer modes. The first shear layer mode occurs for a Strouhal number range 0.2-0.4, and the second occurs at a Strouhal number from 0.7-0.9. The Strouhal numbers remain fairly constant for each of the three associated acoustic modes. This is unlike studies involving the fluid-dynamic feedback where the Strouhal numbers vary inversely in relation to the Mach number (Tam & Block, 1978).

2.5.2 Distribution of Acoustic Particle Velocity

Based on Howe's aeroacoustic analogy, the generation, or absorption, of acoustic power $\mathcal{P}$ is most efficient when the three components of the triple product ($\vec{\omega}$, $\overrightarrow{U}$ and $\overrightarrow{U_a}$) are perpendicular to each other. In the cases consisting of an axisymmetric shear layer, the radial component of the acoustic particle velocity is the energy generating component. However, the distribution and magnitude of this component will vary depending on the cavity-duct geometry and the acoustic mode being excited.

In the case of longitudinal acoustic modes, the component of the acoustic particle velocity $\overrightarrow{U_a}$ is parallel to that of the mean flow velocity, $\overrightarrow{U}$. Through the triple product within Howe's analogy, the overall acoustic power generated and absorbed throughout the acoustic cycle would seem to be zero. However, studies conducted by Hourigan et al. (1990) on a longitudinal mode present in a duct with baffles, helped illustrate that the acoustic particle velocity included a perpendicular component to that of the mean flow, arising from the streamline curvature around the baffle. A similar behaviour is observed at the upstream and downstream edges of shallow cavities excited by longitudinal acoustic modes (Mohamed & Ziada, 2014). Since the acoustic properties only vary in the axial direction, the associated acoustic particle velocity distribution will be uniform along the shear layer circumference.

For the trapped diametral acoustic modes, however, the acoustic properties vary along the azimuthal orientation due to its asymmetric mode shape. Contour plots of the radial acoustic particle velocity distributions for the first three diametral modes located at the midpoint of the axisymmetric cavity with h=25.4mm, L/h=1, are shown in Figure 2-15.

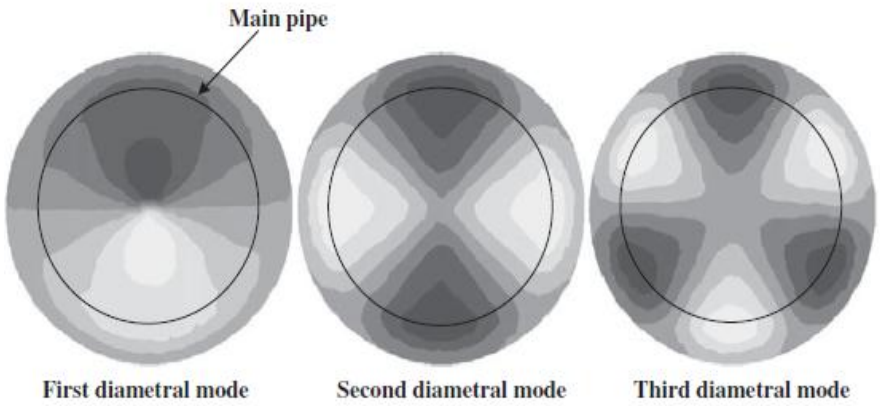

Figure 2-15: Radial acoustic particle velocity distribution of the diametral modes within an axisymmetric cavity with h=25.4mm, L/h=1 (Aly & Ziada, 2010)

As shown, the radial acoustic particle velocity distribution for each of the three excited diametral modes is non-uniform and akin to its corresponding mode shape. Also, the areas with the largest radial particle velocity fluctuations move outwards in the radial direction as the mode order increases.

These differences in the radial acoustic particle velocity distributions lead to two unique excitation mechanisms. For longitudinal acoustic modes, since the radial particle velocity is *uniform* along the whole circumference of the axisymmetric shear layer, the energy exchange and excitation of disturbances all along the circumference and length of the cavity shear layer is *synchronized*.

However, in the case of the diametral modes in Figure 2-15, the excitation mechanism, and energy exchange, is three-dimensional and much more complex. The radial acoustic particle velocity fluctuations are *non-uniform* along the shear layer circumference and different circumferential sections of the shear layer may be excited out of phase and at various amplitudes. The distribution of these particle velocity fluctuations is dictated by the relative position to the acoustic mode shape and its associated nodal lines.

2.6 Effects of Symmetry on the Diametral Modes

The excitation of an asymmetric diametral mode housed within an axisymmetric cavity configuration leads to non-preferred orientations of the simulated mode shapes displayed in Figure 2-9. The symmetry incorporated with the cylindrical geometry ensures that there are an infinite amount of mode shapes corresponding to each eigenvalue (resonant frequency) that is resolved from the Helmholtz equation (Morse, 1948).

In the case of the first acoustic mode, each of these mode shapes corresponds to a unique angular orientation of its nodal line. In most cases of degeneracy, the preferred mode shape would depend on the orientation where the system is initially excited, fixing the mode in a particular orientation (Kinsler et al., 2000; Morse, 1948). However, the axisymmetric shear layer is excited wholly

along the circumference of the upstream edge. This results in the acoustic mode to spin about its axis at a rate equal to its resonant frequency. This behaviour is referred to in literature as a fully spinning mode (Aly & Ziada, 2011).

In addition to the work done on axisymmetric cavities, previous investigations on spinning, or turning, azimuthal modes have been detected in axisymmetric geometries in applications involving stator/rotor interactions (Tyler & Sofrin, 1962) and transverse thermo-acoustic instabilities within annular combustion chambers as detailed in the review by O'Connor et al. (2015).

Experiments on trapped diametral acoustic modes within axisymmetric cavities observed fully spinning behaviour when the cavity was perfectly axisymmetric (Aly & Ziada, 2011). If a large amount of asymmetry was introduced into the cavity domain, then a preferred orientation would be introduced and the acoustic mode would remain stationary. This was observed in experiments conducted by Keller & Escudier (1983) where the orientation of stationary diametral modes within a confined axisymmetric cavity varied when the assembly was taken apart and reassembled. Likewise, if only a slight amount of asymmetry is introduced within the geometry, an intermediate "partially spinning" behaviour is observed (Aly & Ziada, 2011). Within annular combustors, asymmetry can be introduced through flame merging (through reduction in spacing) and introducing baffles, resulting in the partially spinning and fully stationary transverse modes (Worth & Dawson, 2013 & 2015).

A spinning mode can be visually represented along its acoustic cycle through the combination of two equivalent orthogonal stationary modes, Figure 2-16, with a 90° temporal phase shift. Depending on the relative amplitudes of these two orthogonal modes, different azimuthal behaviours are obtained. If this amplitude ratio is zero, A/B=0, the resultant mode is identical to the stationary orthogonal mode with non-zero amplitude, B. If the two amplitudes are equal, the resultant mode will be a fully spinning mode. If the amplitudes are not equal and

larger than zero, then the previously mentioned intermediate partially spinning mode is obtained.

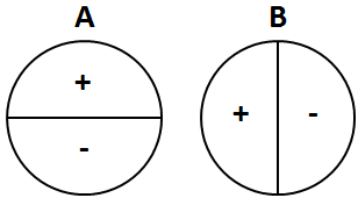

Figure 2-16: Schematic of two equivalent orthogonal modes with amplitudes A & B

This two orthogonal model has been utilized in different studies involving the representation of spinning modes within axisymmetric cavities (Aly, 2008), as well as in combustion chambers (Worth & Dawson, 2013; Salle et al., 2004 & 2006) for example. A graphical comparison of the spinning mode (left) and partially spinning mode (right) for an axisymmetric cavity at six equal interval phases through a half-cycle are displayed in Figure 2-17 (Aly, 2008).

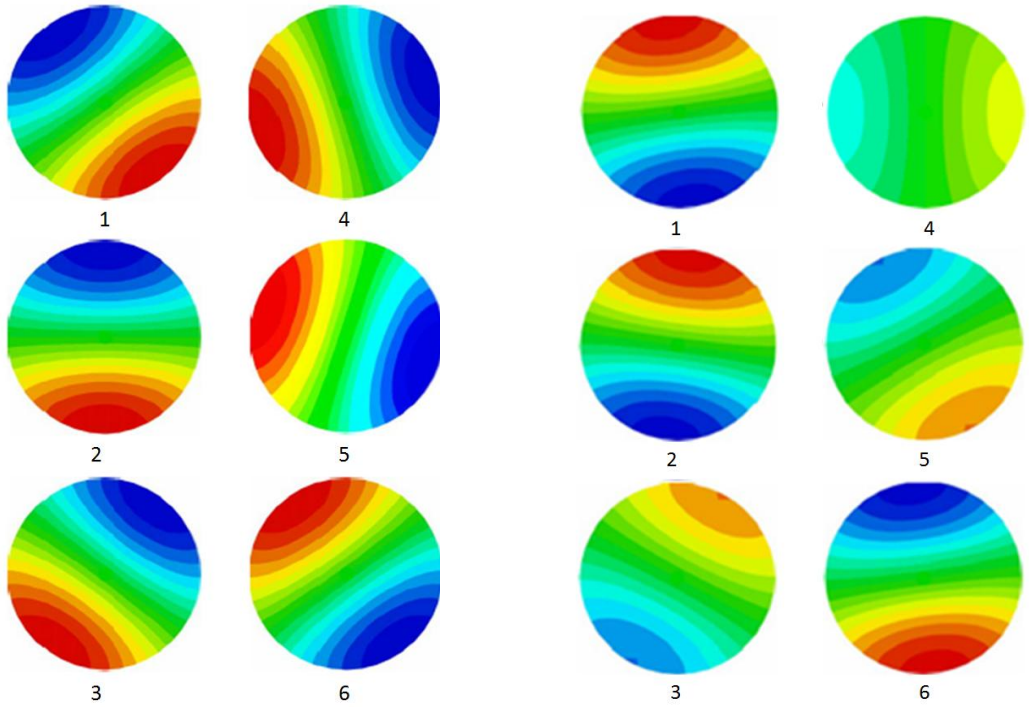

Figure 2-17: Comparison of the fully spinning, A/B=1, (left) and partially spinning, A/B=0.4, (right) acoustic modes within an axisymmetric cavity along six equal interval phases of its half acoustic cycle (Aly, 2008)

For both spinning modal behaviours, the nodal line of the mode rotates at the excited resonant frequency. In the case of the fully spinning mode (left) the acoustic pressure distribution remains constant about its rotating nodal line. However, for the partially spinning mode (right), this distribution varies in a sinusoidal manner along the azimuthal direction, similar to that of a stationary diametral mode. This variation in acoustic pressure along one full cycle is determined by the relative ratio of A/B.

The presence of spinning diametral modes has also been observed in other symmetric geometric domains including the numerical work by Selle et al. (2004 & 2006) on a simplified square cross-sectional combustion chamber. At the chamber entrance, the inlet burner consisted of two coaxial swirlers, one axial and one diagonal. Analysis utilized compressible LES to solve the turbulent flow and acoustics simultaneously, and Helmholtz solvers to resolve the mode shapes according to a defined flow field.

LES Simulations conducted under reacting conditions observed turbulent fluctuations being dominated by high-frequency oscillations of a transverse spinning acoustic mode. This oscillation frequency, f=1198Hz was equivalent to the resonant frequency of two resolved simulated orthogonal acoustic modes illustrated in Figure 2-18.

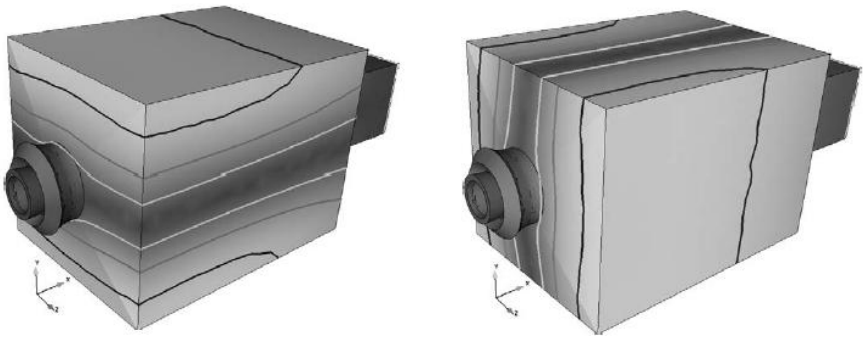

Figure 2-18: Two resolved equivalent orthogonal modes whose resonant frequency, f=1198Hz, was detected through turbulent fluctuations (Selle et al.,2006)

From the symmetry inherent within the square geometry, there were two orthogonal mode shapes corresponding to the same resonant frequency. This provides no preferential orientation to the excitation of either of the two acoustic modes, and similar to the axisymmetric domain, results in a spinning behaviour.

Utilizing the two mode orthogonal mode, the acoustic mode shape and the *axial* acoustic particle velocity along one acoustic cycle were resolved and visually represented. The influence of the acoustic mode was then compared to the simulated flame structure from LES. These results are taken at a field-of view shown in Figure 2-19, and are represented along half an acoustic cycle in Figure 2-20.

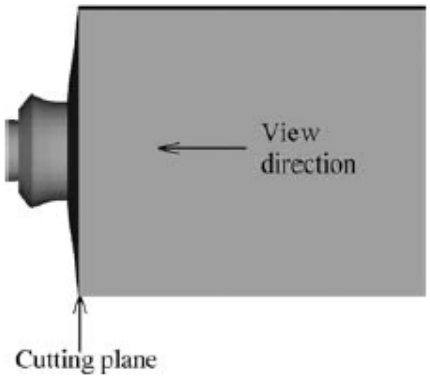

Figure 2-19: Cross-sectional view used in the visualization of the acoustic spinning mode (Selle et al.,2006)

As shown, the acoustic mode rotates about the cavity at its resonant frequency. The acoustic particle velocity contour is non-uniform along the burner mouth and is 90° out of phase with the acoustic pressure distribution. This is quite different to the uniform excitation of the shear layer associated with the longitudinal mode. Instead, only specific sections of the shear layer are being excited at a time and these sections are now rotating about the circumference of the burner. As such, the resolved flame structure is of a helical type and is akin to the particle velocity fluctuations acting along the upstream edge.

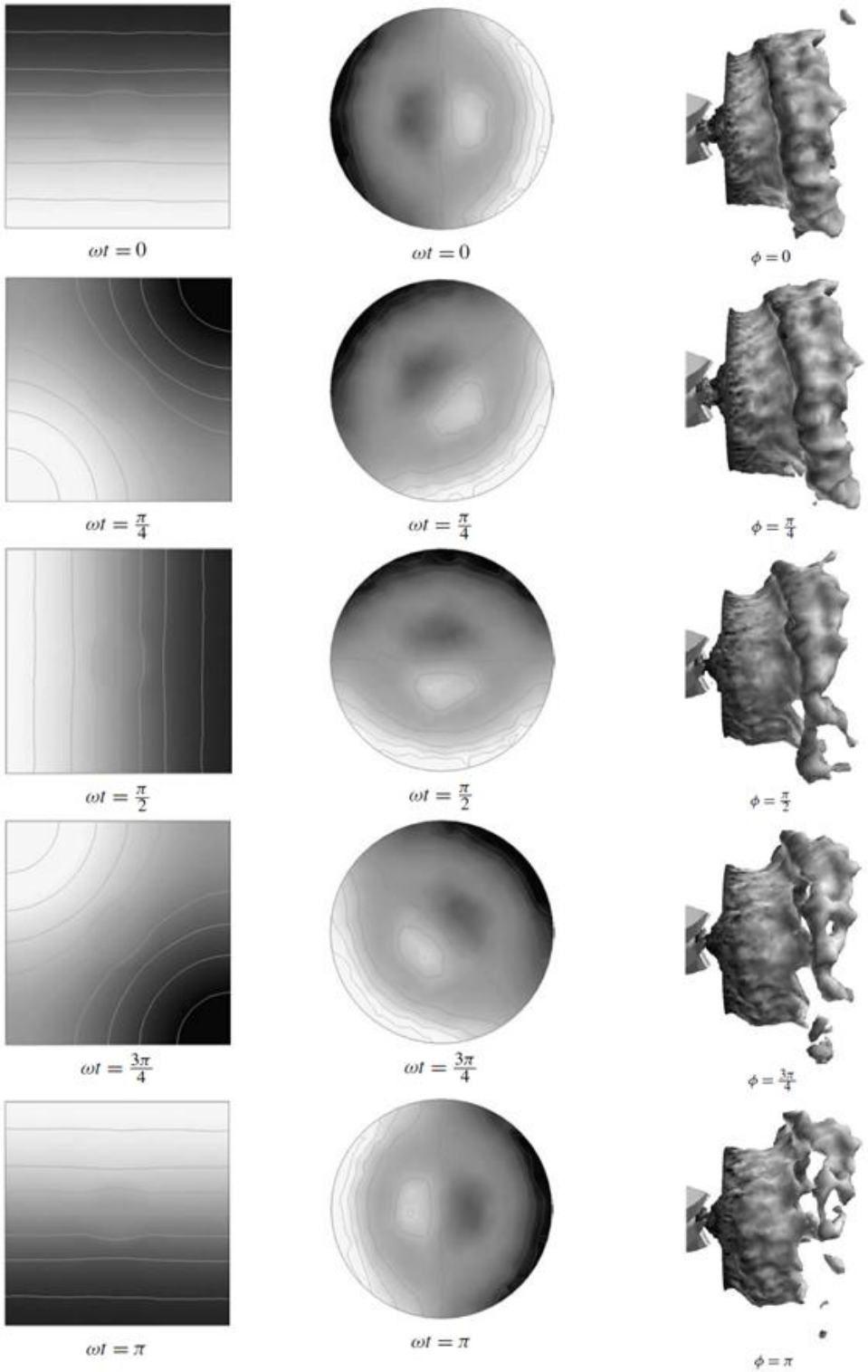

Figure 2-20: Simulated mode shape (left), axial acoustic particle velocity (middle), and helical structure (right) during half an acoustic cycle of the spinning acoustic mode (Selle et al.,2006)

2.7 Noise Control of Trapped Diametral Modes

The suppression of acoustic resonance from grazing flows over cavities has been investigated extensively within literature. These mitigation techniques are implemented when acoustic resonance is undesirable and avoidance is not possible. Control methods are generally categorized as being either active or passive.

Active control involves applying external energy into the system and involves methods such as oscillating flaps and pulsed fluid injection (Cattafesta et al., 2003). The cost of installation and its separate components make active control generally impractical within industrial applications, particularly in the case of a confined cavity domain. Nonetheless, it has been successfully implemented in reducing the acoustic resonance of trapped diametral modes in laboratory settings. Ziada et al. (2003) utilized a synthetic jet generated from two loudspeakers positioned at the upstream cavity corner. The externally applied acoustic pressure successfully cancelled out the interaction with the acoustic particle velocity, suppressing the acoustic resonance.

Many studies have focused on passive remedial means, involving geometric modifications situated at the upstream edge of the cavity. The focus of these modifications is to influence the initiation and formation of vortical structures from the interaction with the resonant sound field. Experiments conducted by Smith & Luloff (2000) investigated the effects of chamfering the upstream edge in reducing acoustic resonance within gate valves. This provided an overall reduction in acoustic pressure; however the acoustic mode shapes within the valve were not indentified and the influence of the chamfers on the global aeroacoustic response was unreliable.

Recently, Bolduc et al. (2014) investigated passive modifications at the upstream edge of the axisymmetric cavities used in the previous studies by Aly & Ziada (2010, 2011, 2012). Schematics of these modifications are illustrated in

Figure 2-21. The dimensions utilized for these experiments were based on previous studies involving the mitigation of longitudinal acoustic modes (Bruggeman et al., 1991; Karadogan & Rockwell, 1983; Knotts & Selamet, 2003; Nakiboğlu & Hirschberg, 2010).

The first geometric modifications consisted of chamfering and rounding the upstream cavity edge, which both delayed the acoustic resonance to higher velocity ranges. This was a direct result of altering the effective impingement length the vortices travel along the cavity. With the length changing, and the resonance Strouhal number remaining constant, the velocity at which acoustic resonance occurs increases. However, the rounding managed to increase the pulsation amplitudes, consistent with mitigation studies of closed side-branches (Bruggeman et al., 1991).

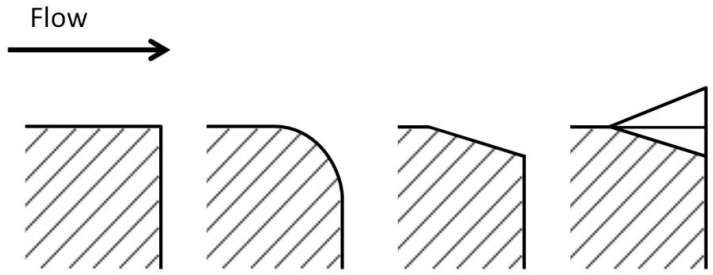

Figure 2-21: Schematic of geometric modifications at the upstream cavity edge. From left to right, sharp edge, rounding, chamfering, and saw-tooth spoiler (Bolduc et al., 2014)

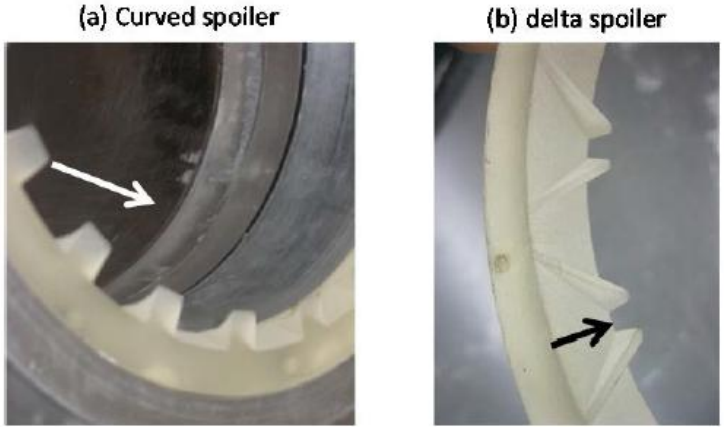

Figure 2-22: Photograph illustrating upstream geometric modifications of the curved and delta spoilers at the shear layer (Bolduc et al., 2014)

In addition, assortments of spoiler geometries were examined. These included various saw-tooth spoilers, a curved spoiler and a unique delta spoiler shown in Figure 2-21 and 2-22. These spoilers were situated all along the circumference of the shear layer, due to the spinning nature of the acoustic mode, and were designed to introduce additional three-dimensional vorticity and turbulence to reduce the coherence of the vortical structures. This in turn, would reduce the flow-sound coupling of the propagating disturbances with the resonant sound field.

The introduction of these spoilers reduced the pulsation amplitude of the acoustic modes significantly, but had an undesirable economic outcome. Depending on the spoiler size, the flow blockage introduced a significant amount of pressure drop within the system. This effect would need to be minimized in order to maintain maximum efficiency within the operations of BWR and PWR plants.

2.8 Objectives

The previous studies investigating the excitation of trapped diametral acoustic modes within cavity-duct domains have focused on axisymmetric geometries. These geometries lead to spinning modal behaviours due to there being no preferred orientation. There has been little attention on asymmetric rectangular cross-sectional cavity-duct domains, which results in the trapped diametral modes being fixed in one unique orientation. This effect of symmetry is investigated in regards to its modal behaviour, trapped nature, and aeroacoustic response.

As well, inspection of rectangular cavity geometries provides some practical benefits over the previous axisymmetric cases. Through removal of the complex spinning nature of the acoustic modes, this provides a simpler model for validation of numerical simulations. Currently, the experimental results obtained from this study are being used to improve CFD codes in the prediction of onset

excitation velocities, pulsation amplitudes, and the acoustic modes for simplified gate valve geometries. Through improvement of numerical simulations, this may provide a means to a better understanding of the excitation mechanism and a design tool for future applications.

The excited acoustic modes are the transverse diametral (cross) modes confined within the cavity. The acoustic properties of these diametral modes vary in the azimuthal direction. Thus, the radial acoustic particle velocity and excitation of the shear layer is non-uniform along the circumference. As well, these associated modes are trapped and consist of very strong acoustic resonance. Despite this complex excitation mechanism, orderly flow structure must occur in order to generate sufficient acoustic energy to maintain these strong pulsation amplitudes. Thus far, little work has been done on understanding this three-dimensional flow-sound coupling between the non-uniform acoustic particle velocity and its propagating structures.

Understanding this excitation mechanism of these complex acoustic modes will expand upon the state of knowledge in the potential of noise suppression techniques that not only mitigate acoustic resonance but do so with minimal pressure drop.

In summary, there are two main objectives within this study:

Investigate the effects of velocity and asymmetry on the excitation mechanisms and trapped nature of the acoustic modes within rectangular cavities.

Investigate the three-dimensional flow-acoustic coupling between the non-uniform acoustic particle velocity of the excited diametral modes and the corresponding downstream propagating structures.

CHAPTER 3
EXPERIMENTAL APPARATUS

This chapter focuses on the experimental facility and test setup that was designed and utilized to investigate the flow-excited acoustic resonance of trapped diametral modes within a rectangular cavity-duct domain. Section 3.1 details the test facility and piping, which is consistent with previous studies involving the excitation of diametral modes in axisymmetric cavities (Aly & Ziada, 2010, 2011, 2012; Bolduc et al.,2013). However, the asymmetric rectangular cavities, Section 3.2, were designed and manufactured to introduce a preferred orientation for the excited diametral modes. Section 3.3 examines the asymmetric acoustic mode shapes and the trapped nature of the acoustic modes, leading to the resolved acoustic particle velocity distributions in Section 3.4. Finally, Section 3.5 details the instrumentations used throughout the measurements.

3.1 Test Facility

A schematic of the test-facility and its components is shown in Figure 3-1. The open loop wind tunnel consists of a 10 blade centrifugal blower powered by a 50hp electric motor. The inlet flow velocity is altered by the rotational speed of the blower through a variable speed control unit. The velocity was altered in a separate room to avoid extended exposure to the high sound pressure levels.

Measurements were conducted up to the maximum capacity of the blower at a Reynolds number of $Re_D = 1.4x10^6$ based off the duct diameter and the velocity measured at the bell-mouth end. The cavity test setup is installed to the inlet, transitioning to an axisymmetric diffuser, until reaching the centrifugal blower. The design of the diffuser was selected from CFD simulations to determine applicable dimensions (Aly, 2008). To ensure the test setup does not move when the flow velocity is changed, chains and a flexible hose to isolate the blower velocity were installed.

1	Test Setup
2	Chains
3	Axisymmetric Diffuser
4	Centrifugal Blower
5	Control Unit
6	Electric Motor
7	Settling Chamber
8	Wind Tunnel Outlet

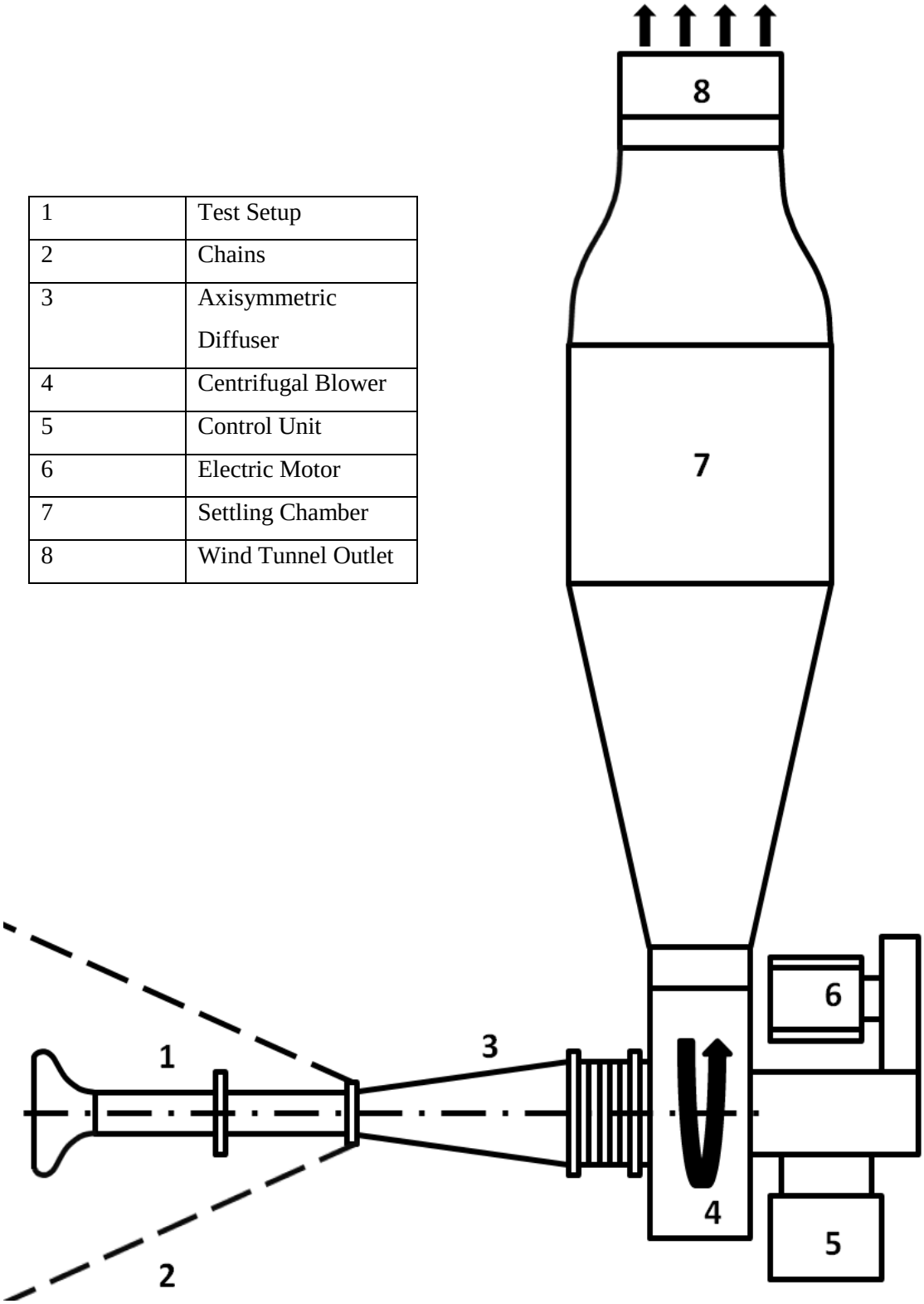

Figure 3-1: Schematic of Test Facility and its components.

3.2 Test Setup

The test section was designed specifically to analyze the excitation of diametral modes within a rectangular cavity. An illustration of the cavity-duct setup is shown in Figure 3-2. The system consists of three main components: the upstream/downstream piping, the cavity domain, and the bell mouth inlet. The inlet and the piping system remained consistent to the investigations of axisymmetric cavities conducted by Aly & Ziada (2010, 2011, 2012). However, three new rectangular cross-sectional cavities were designed, manufactured, and installed.

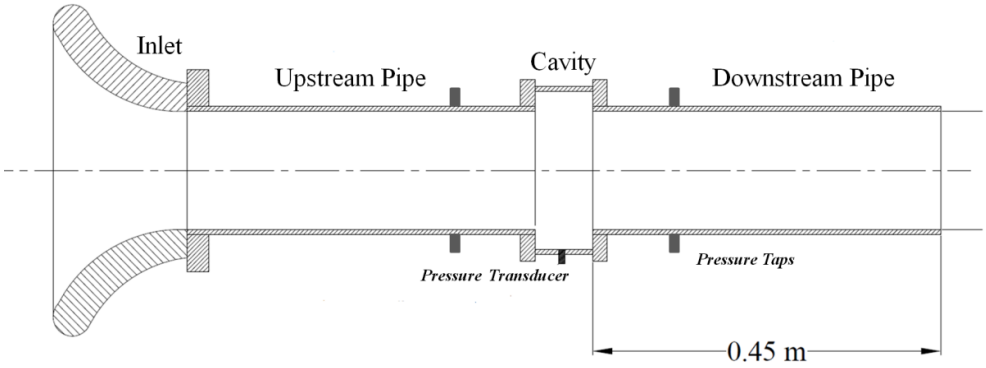

Figure 3-2: Schematic of Test Setup (Aly & Ziada, 2010)

Upstream and downstream of the cavity consisted of two L =450mm long clear acrylic pipes. The inner diameter of these pipes, D, was 150mm and had a thickness of 6.25mm. Numerical simulations, discussed in Section 3.3, illustrate that the ample lengths of the pipes do not alter the acoustic mode shapes. At the terminations of the pipes are two flanges to connect the cavity domain to the piping system. O-rings and gaskets were used in between the flanges and the pipes to ensure proper sealing and to minimize acoustic losses from the system.

Two sets of eight pressure taps were installed at 45˚ intervals along the circumference of the piping system. The taps were located 30cm upstream and downstream from the cavity edges to measure the static pressure drop across the cavity domain. This large number of pressure taps along the circumference was

chosen to ensure that the average static pressure was a good representation of the pressure drop whether the excited diametral mode was spinning or stationary.

The inlet of the system consisted of a smooth bell mouth. It had a parabolic contraction to ensure that the mean velocity profile was uniform within the pipe and that the turbulence intensity was minimized. A non-uniform velocity profile, particularly along the upstream shear layer, may result in unwanted disturbances influencing the excitation of the diametral modes. Thus, much care was placed to ensure the contraction was as smooth and uniform as possible

3.2.1 Cavity Geometry

Three separate cavities were manufactured and tested. A generalized schematic of the cavity geometry is shown in Figure 3-3. All manufactured cavities had a length of L=25.4mm and constant height of H =254mm. The difference in geometry is due to variations in the width, W, where only slight variations from unity (W/H=0.9-0.95) were considered for the two rectangular cavities. The dimensions of the manufactured cavities are listed in Table 3-1.

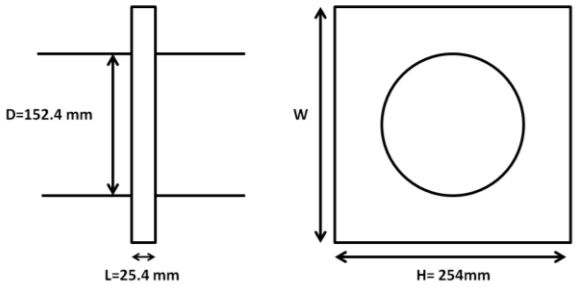

Figure 3-3: Schematic of cavity dimensions and geometry

Table 3-1: Dimensions of three manufactured cavities, L=25.4mm and H=254mm

Type	*W/H*	*H* (mm)	*W* (mm)
Square	1	254	254
Rectangular 1	0.95	254	241.3
Rectangular 2	0.9	254	228.6

The reference dimensions for the square cavity were selected by reviewing the aeroacoustic responses of axisymmetric cavities (Aly & Ziada, 2010). The chosen L=25.4mm and *W*=*H*=254mm square geometry is close to the axisymmetric cavity with L/h=0.5, h/D=1/3, which produced strong resonance of the first three modes. The dimensional comparisons and aeroacoustic response are shown in Figures 3-4 and 3-5.

This axisymmetric cavity held preferential characteristics in its aeroacoustic response when compared to its counterparts. As observed in Figure 3-5, there was evidence of numerous diametral trapped modes being excited at lower velocity ranges providing a means to compare and observe the excitation mechanisms of *multiple* diametral modes within the capacity of the blower. The excitation at lower flow velocities also reduces the likelihood of complications arising from the use of Particle Image Velocimetry including the buildup of seeding particles and the required time delay between consecutive images.

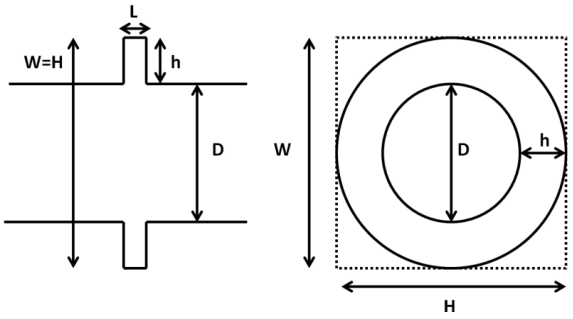

Figure 3-4: Dimensional comparisons between axisymmetric and present square cavity (dashed).

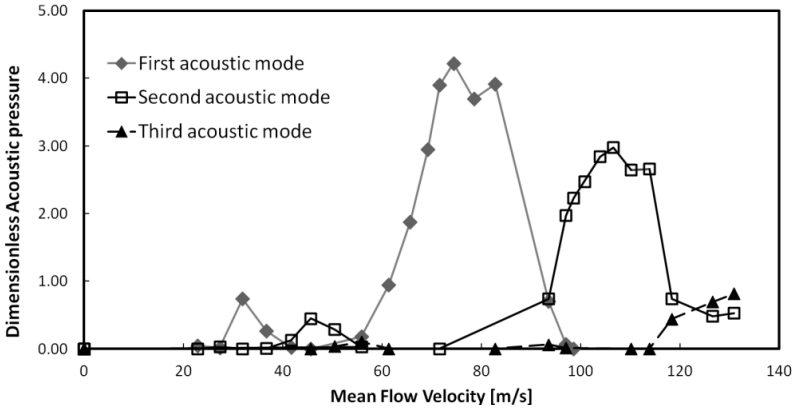

Figure 3-5: Dimensionless aeroacoustic pressure response for axisymmetric cavity, L/h=0.5, h/D=1/3 (Aly & Ziada, 2010)

The geometries of the two rectangular cavities were selected to introduce asymmetry to the reference square cross-section. Only slight deviations from the square cavity were considered, (W/H=0.9 & 0.95), introducing two orthogonal resonance modes that have comparable, yet slightly offset frequencies (0% for the square and 9% for rectangular cavity 2). Comparisons of the three cavity geometries would provide insight on the effects of asymmetry on both the aeroacoustic responses and the behaviours of the excited diametral modes.

3.2.2 Test Section Assembly

The cavities are constructed from two sets of acrylic side walls which are assembled together using clamps, threaded rods, gaskets and silicon to ensure proper sealing and to produce the assembly which is illustrated in Figure 3-6. For the three manufactured cavities, three similar pairs of side walls were used for the constant 254mm height. To alter the varying cavity width, W, another three pairs for the top and bottom were installed depending on the desired cavity geometry. The dimensions of these sets of side-walls are detailed in Figures 3-7 and-3-8 and Table 3-2. As well, additional holes were machined into the cavity walls to allow dynamic pressure transducers to remain flush to the inner cavity wall coinciding with the anti-nodes of each of the investigated diametral modes.

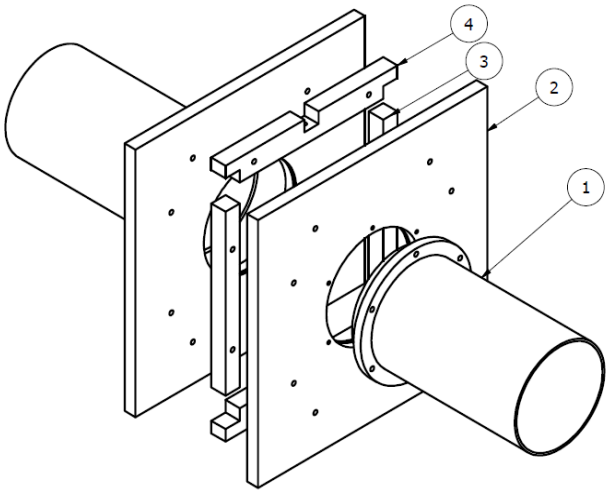

1	Piping
2	Flange
3	Constant side wall
4	Variable top wall

Figure 3-6: Detailed exploded assembly of test section

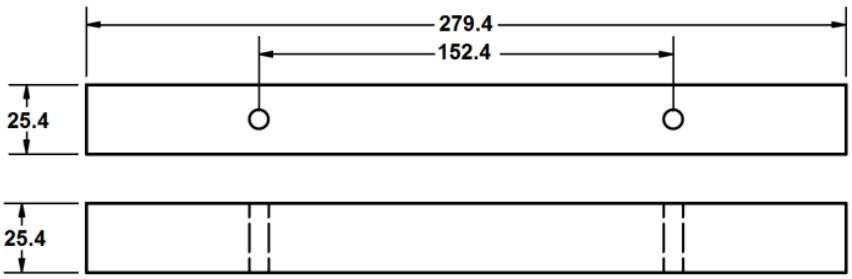

Figure 3-7: Dimensions (mm) of Constant side wall used in all three cavities

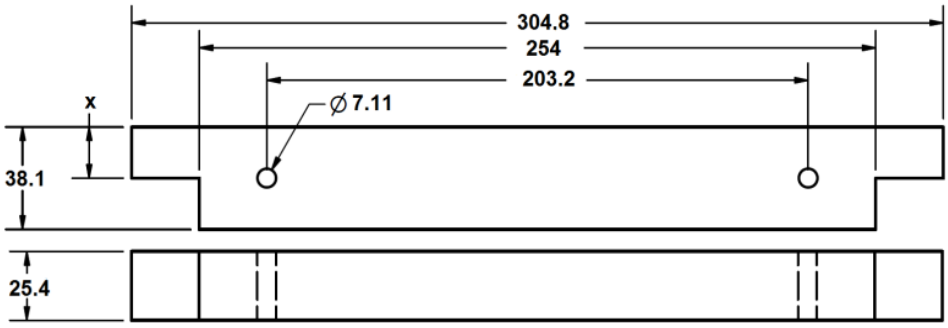

Figure 3-8: Dimensions (mm) of Variable top and bottom walls with varying dimension X

Table 3-2: Dimensions (mm) of variable x corresponding to the three separate manufactured cavities

Type	*W/H*	*W* (mm)	X (mm)
Square	1	254	25.4
Rectangular 1	0.95	241.3	19.05
Rectangular 2	0.9	228.6	12.7

To attach the side lengths to the upstream and downstream piping, and to clamp the cavity in place, two acrylic square flanges were manufactured on a CNC milling machine. Eight holes with transition fits were machined into the flanges coinciding with holes positioned in the side lengths and clamped using threaded rods. The CNC was also utilized to remove any potential non-uniformity at the upstream and downstream corners of the cavity in accordance to the piping. This procedure allowed proper and consistent alignment of the cavity with the pipe diameter. O-rings, gaskets and silicon sealing were applied on the interfaces between the cavity, flanges, and piping to remove any potential sources of leakage. This overall assembly of the test setup provided easy transition between cavity geometries, proper sealing, and optical clarity for flow visualization.

3.3 Numerical Simulations

3.3.1 Simulation and Mesh Configuration

The distribution of acoustic pressure, *P*, for the three-dimensional trapped diametral acoustic modes can be resolved through the three-dimensional wave equation:

$$\frac{1}{c^2}\frac{\partial^2 P}{\partial t^2} - \nabla^2 P = 0 \tag{3.1}$$

where *c* is the speed of sound, and ∇ represents the Laplacian represented below in Cartesian coordinates:

$$\nabla^2 = \frac{\partial^2}{\partial x^2} + \frac{\partial^2}{\partial y^2} + \frac{\partial^2}{\partial z^2} \tag{3.2}$$

The oscillating pressure field of the acoustic modes is a harmonic function in time, *t*, and can written as:

$$P\,(x, y, z, t) = \bar{P} e^{i\omega t} \tag{3.3}$$

where $\bar{P}$ is the spatial distribution of the acoustic pressure and ω is the angular resonance frequency of the mode. Substituting equation (3.3) into equation (3.1) the Helmholtz equation is obtained:

$$\nabla^2 \bar{P} + \frac{\omega^2}{c^2}\bar{P} = 0 \tag{3.4}$$

Commercial FEA software ABAQUS was utilized to numerically solve this eigenvalue problem at zero flow conditions. The resultant eigenfunctions represent the dimensionless acoustic pressure distribution (the mode shapes), and the eigenvalues are the corresponding resonant frequencies. The computational mesh is composed of three-dimensional linear tetrahedral elements consisting of four nodes. The domain is composed of air with properties at room conditions with a density $\rho = 1.23\,\frac{kg}{m^3}$ and an adiabatic bulk modulus, K=142000Pa.

Realistic boundary conditions were utilized to fully represent the physical problem. For a fully trapped mode, the end effects would have no influence on the acoustic pressure distribution within the cavity domain. As such, the acoustic pressure was set to zero at the terminations of the pipe to represent free ends with negligible radiation. As well, solid wall conditions at the surfaces were defined to ensure that pressure gradient was zero at these boundaries.

Additional simulations verified the pipes were of ample length, with any additional length having no influence on the trapped mode shapes and resonant frequencies. Figure 3-9 demonstrates the variation in resonant frequency with changes in pipe length per diameter, L/D, for the first resolved mode in the *W/H*=0.9 rectangular cavity. After two pipe diameters, both upstream and downstream, the pipe length has a negligible effect, around 0.001%, on the resonant frequency. Therefore, a final length of three pipe diameters was used in the computation, consistent to the experimental setup.

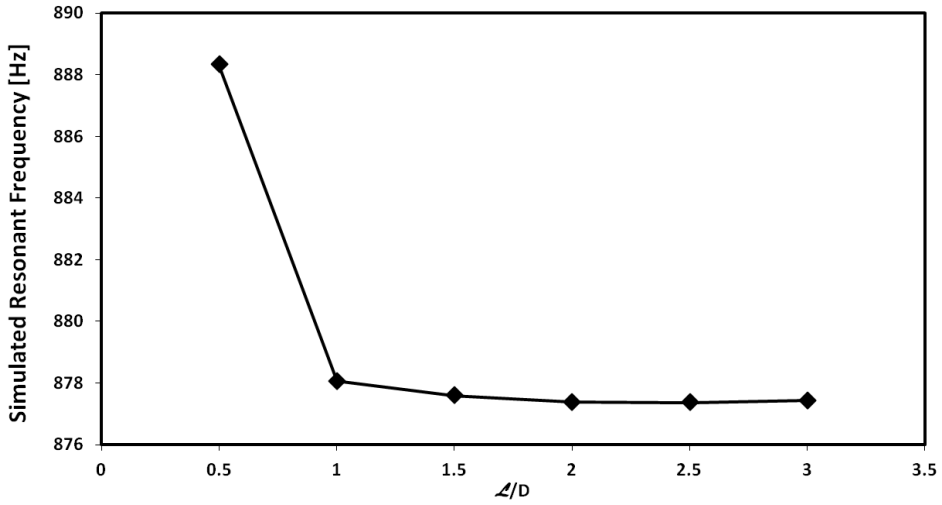

Figure 3-9: Influence of pipe length per diameter (L/D) on simulated resonant frequency, *W/H*=0.9, first acoustic mode

The convergence of the *W/H*=0.9 cavity's first resonant frequency, with an increase in elements, is shown in Figure 3-10. As the number of elements increased from $8x10^5$ to $1.0x10^6$, the resonant frequency varied slightly by

0.035%. Thus a conservative number of elements, $2.3x10^6$, consisting of a global element size of 0.00275mm were used within the simulation. This large number of elements ensured that there was a sufficient amount of nodal points along the circumference of the upstream shear layer for the eventual resolved acoustic particle velocity distribution. At the junctions of the upstream and downstream ducts with the cavity domain, sharp edges were also rounded with a radius of 0.6mm to remove any singularities.

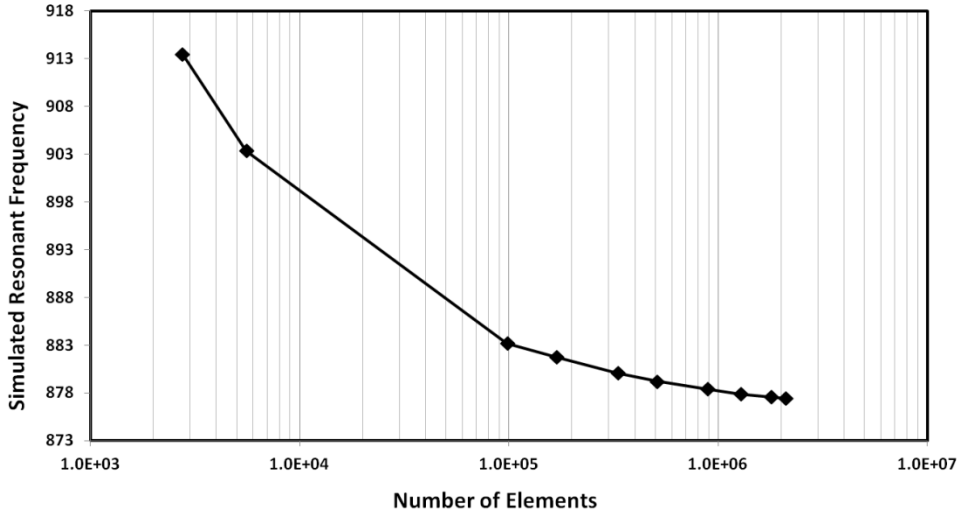

Figure 3-10: Convergence of first resonant frequency with increasing number of elements, *W/H*=0.9 rectangular cavity

3.3.2 Simulated Trapped Diametral Acoustic Modes

The resolved acoustic mode shapes for the *W/H*=0.9 rectangular cavity are presented in Figure 3-11. The cross-sectional views are situated within the middle of the cavity where the dashed lines represent the nodal lines. These four acoustic trapped modes are classified from *f1-f4* in sequence of increasing resonant frequency and onset excitation flow velocity. As shown, the acoustic modes are non-uniform along the cavity perimeter.

The first two trapped modes are orthogonal to one another and consist of a single nodal line and a half wavelength along their respective side length. The first mode is associated with the longer side, *H*, and consists of a larger half

wavelength and lower resonant frequency than the second mode which occurs along the smaller dimension, *W*. The third and fourth modes have two nodal lines, which are the symmetry axes in the third mode and the rectangular diagonals in the fourth mode. These latter acoustic modes consist of four anti-nodes situated along the inner perimeter of the cavity.

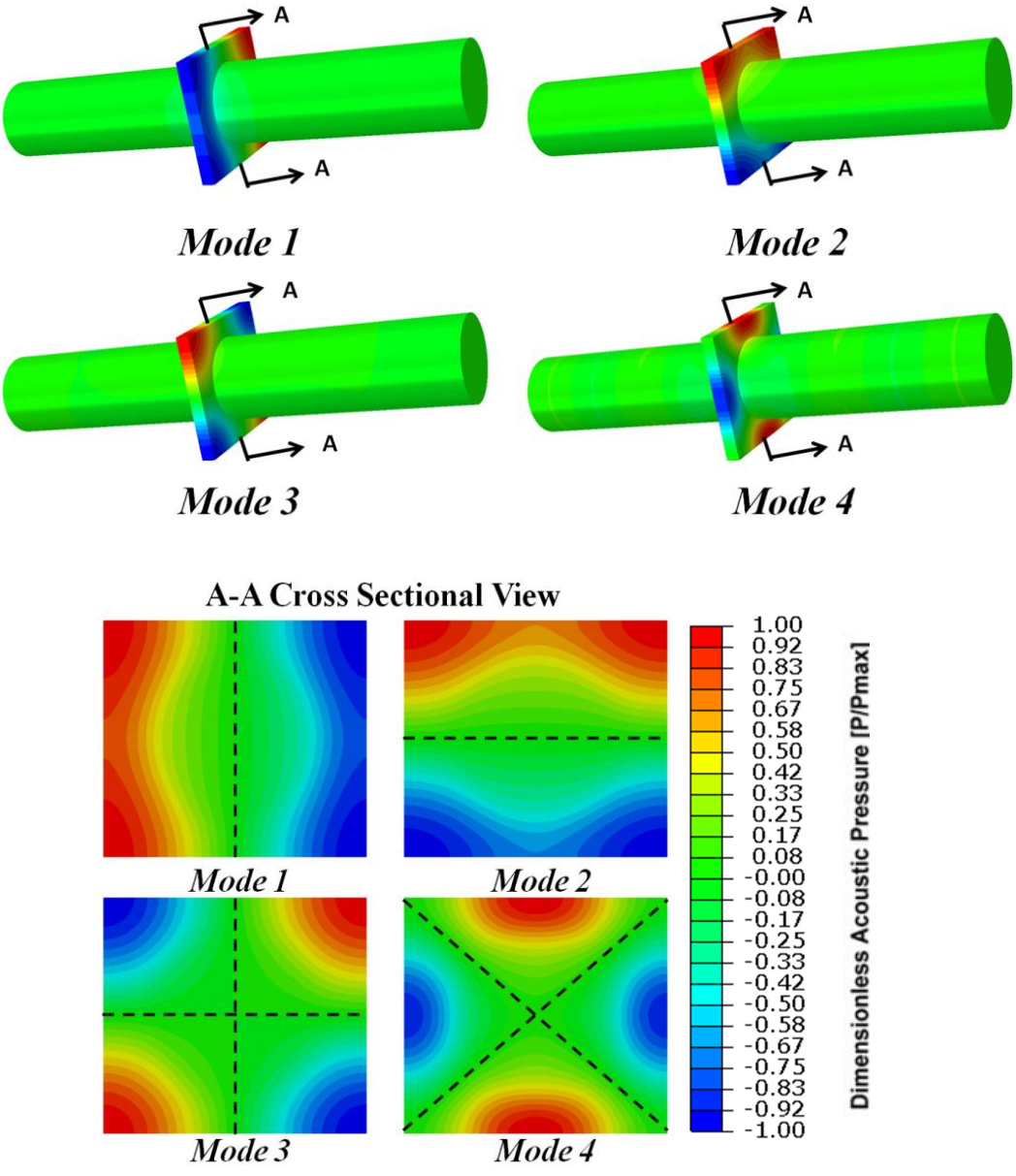

Figure 3-11: Resolved mode shapes of the four trapped acoustic modes at the center of the rectangular, *W/H*=0.9, cavity

The four acoustic modes are trapped with the acoustic energy being highly localized within the cavity domain and the pressure amplitude exponentially decaying in the axial direction. This is consistent to simulations previously conducted for the trapped modes within axisymmetric cavities (Aly & Ziada, 2010). Locally, the confinement of acoustic energy becomes greater in the outwards radial direction from the attached piping. This observed behaviour is most prominent within the first two acoustic modes where the mode shape tends to get modulated by the curvature of the piping. Instead of the anti-node pressure being present all along the cavity's height or width, the maximum pressure pulsations are situated within the corners of the cavity and decrease towards the midpoints of the side lengths.

As one of the cavity sides gets smaller, the radial distance between the cavity perimeter and the piping gets shortened. This results in increased acoustic radiation into the upstream and downstream pipes, which weakens the trapped nature of the mode. This behaviour may be observed through comparisons of the first and second mode shapes in Figure 3-11. For the first mode, larger pressure pulsations are located within the middle of its side lengths, due to the height, *H*, having a larger radial distance from the piping curvature than the width, *W*, which is associated with the second acoustic mode. As *W/H* approaches unity, these two orthogonal simulated mode shapes become equivalent. A similar behaviour is also observed when comparing the mode shapes of the fourth acoustic mode for the three cavity geometries

These four trapped diametral modes are strongly excited in each of the three tested cavities. An additional fifth trapped mode was also detected within experiments and simulations, consisting of six anti-nodes along the cavity perimeter. However, because of its additional complexity and that its full resonance range was beyond the maximum capacity of the blower, this mode is not addressed here. It is important to note that the main objective of this study is to investigate the interaction between the resonant sound field and flow field for

simplified geometric mode shapes. The simulated resonance frequencies of the four acoustic modes are given in Table 3-3 for the three investigated cavities.

Table 3-3: Simulated resonant frequencies of the four trapped acoustic modes for the three cavity geometries

	Resonant Frequencies (Hz)			
W/H	***f*1**	***f*2**	***f*3**	***f*4**
1	855	855	1027	1500
0.95	866	903	1059	1550
0.9	878	954	1097	1610

The trapped nature of the acoustic mode depends on the ratio of the resonant frequency to the cut-off frequency of the attached piping. As this ratio decreases, more acoustic energy is confined within the cavity and less is radiated axially down the piping (Kinsler et al., 2010). The first two calculated cut-off frequencies of the pipes, 1307Hz and 2166Hz, correspond to one and two nodal lines. The first resonant frequencies, *f1* and *f2* (855-954Hz), consist of one nodal line and are much lower than those associated with the first cut-off frequency. Likewise *f3* and *f4* (1027-1610Hz) consist of two nodal lines and are significantly lower than the second cut-off. Since these acoustic modes of the cavity are inherently three-dimensional, changing the dimension of one side of the cavity (e.g., width *W*) has a slight effect on the resonance frequency of the mode along the other dimension, *H*, as illustrated through the small variations in the first resonant frequency.

For the square cavity, since *H* is equal to *W*, the associated wavelengths and resonant frequencies of the first two orthogonal modes are identical. This is commonly referred to in literature as a degenerate mode (Kinsler et al., 2010) (Morse, 1948). From the symmetry inherent within the square cross-sectional geometry, the solution of the Helmholtz equation resolves two separate eigenfunctions coinciding to one distinct eigenvalue, providing no preferential orientation to the excitation of either of the two orthogonal modes. The excitation of this degenerate mode results in a unique spinning behaviour that will be discussed in detail within the experimental results.

3.4 Acoustic Particle Velocity

The excitation mechanism is due to a flow-acoustic coupling between the resonant sound field, via the acoustic particle velocity, $\overrightarrow{U_a}$, the flow field, via the vorticity vector, $\vec{\omega}$, and the mean flow velocity vector, $\vec{U}$. Howe's aerodynamic theory of sound approximates the acoustic power production, $\mathcal{P}$, from the interaction between each of these variables (Howe, 1980).

$$\mathcal{P} = -\int(\rho \int \vec{\omega} \cdot (\vec{U} \times \overrightarrow{U_a})\, d\forall) dt \tag{3.5}$$

As demonstrated in the above expression, the generation, or absorption, of acoustic power $\mathcal{P}$ is largest when all three components of the triple product ($\vec{\omega}$, $\overrightarrow{U}$ and $\overrightarrow{U_a}$) are orthogonal to one another. In the current case involving an axisymmetric shear layer, illustrated in the schematic Figure 3-12, it is the radial component of the acoustic particle velocity which is orthogonal to both the shear layer vorticity, $\vec{\omega}$, and mean flow velocity, $\overrightarrow{U}$. The radial velocity fluctuations, due to the resonance of the acoustic mode, initiate the formation of disturbances along the circumference of the upstream separation edge.

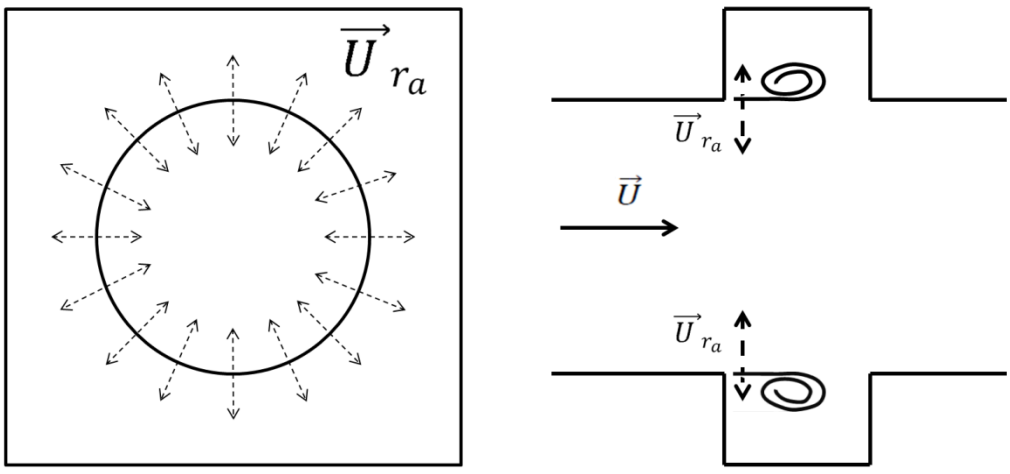

Figure 3-12: Simplified schematic of a uniform radial acoustic particle velocity vector distribution, $\overrightarrow{U}_{r_a}$, represented by dashed vectors. This initiates the formation of disturbances at the upstream axisymmetric separation edge.

The simplified schematic in Figure 3-12 displays a uniform distribution of radial acoustic particle velocity along the shear layer circumference at the cavity upstream edge. This distribution, consistent to that of a longitudinal acoustic mode, would result in a synchronized triggering of the whole shear layer circumference. The resultant formation of disturbances would be uniform and would consist of a toroidal vortex, or vortex ring, propagating downstream.

However, in the present study, the simulated diametral trapped acoustic modes are non-uniform and asymmetric about the cavity. As such, the associated radial acoustic particle velocity along the shear layer circumference will vary. Assuming an adiabatic process, the distributions of acoustic particle velocity of each of the simulated diametral modes can be resolved from the three-dimensional pressure gradient, ∇P, via Euler's equation:

$$\rho_o \frac{\partial \overrightarrow{U_a}}{\partial t} = -\nabla P \tag{3.6}$$

Assuming simple harmonic motion, the acoustic particle velocity, $\overrightarrow{U_a}$, may be rearranged as follows:

$$\overrightarrow{U_a} = \frac{-\nabla P}{\omega \rho_o} \tag{3.7}$$

For each of the simulated acoustic modes, the three-dimensional pressure gradients, ∇P, were determined through the acoustic pressure distributions in their FEA simulations. A code developed specifically for three-dimensional linear tetrahedral 4-node elements was utilized and validated against closed-form solutions. From the above method, a three dimensional distribution of the acoustic particle velocity is resolved.

Emphasis is placed at the upstream edge of the shear layer, where the formation of vortical structures is initiated by the radial acoustic particle velocity. Thus, the radial component can be extracted from the three dimensional velocity

vectors along the separation edge. However, to avoid potential singularities at the edges of the cavity and piping, all presented distributions are located slightly offset, 0.2mm, from the upstream separation edge.

3.4.1 Radial Acoustic Particle Velocity Distributions

Figure 3-13 presents normalized contour plots from the initial simulated acoustic mode shape to the extracted radial acoustic particle velocity vectors along the shear layer circumference near the cavity upstream corner. These figures are associated with the second acoustic mode of the *W/H*=0.9 rectangular cavity with the cavity corner being represented by the circular line. As clearly displayed, unlike the longitudinal mode, the radial acoustic particle velocity distribution is non-uniform along the shear layer circumference and its distribution is akin to its asymmetric mode shape.

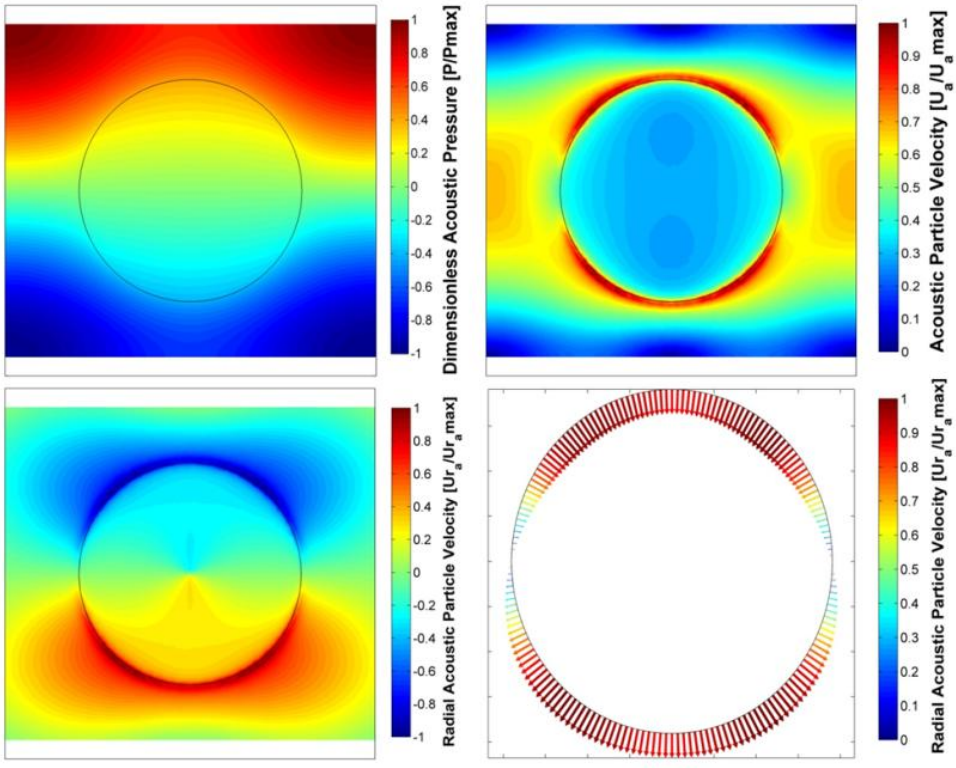

Figure 3-13: Dimensionless (Top Left) Acoustic pressure distribution, (Top Right) Acoustic particle velocity magnitude, (Bottom Left) Radial acoustic particle velocity distribution, (Bottom Right) Radial particle velocity along shear layer circumference (all figures correspond to 0.2mm downstream from the inlet of the *W/H*=0.9 rectangular cavity)

Likewise, the radial acoustic particle velocity distributions of the remaining three acoustic modes and their acoustic pressure distributions are shown in Figure 3-14. Similar to the second acoustic mode, the radial acoustic particle velocity closely resembles the acoustic mode shape. The points of *zero radial velocity fluctuations* correspond to the nodal pressure lines, and the *maximum radial velocity* amplitudes coincide to the anti-nodes of the associated mode. As well, the radial acoustic particle velocity oscillations occur along specific circumferential portions of the shear layer separated by their nodal points. The first two acoustic modes consist of two circumferential sections, and the third and fourth corresponding to four. Further investigation of the non-uniform acoustic velocity distribution and their effect on the development of vortical disturbances will be focused upon within the experimental results.

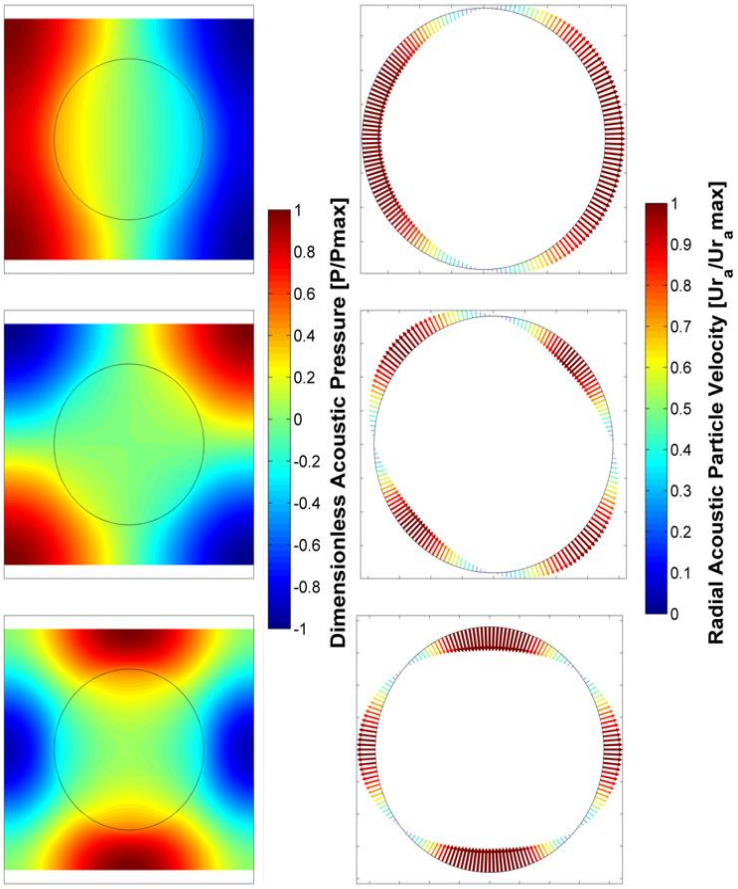

Figure 3-14: Normalized acoustic pressure distribution and corresponding radial acoustic particle velocity along the upstream cavity mouth for the *W/H*=0.9 rectangular cavity

3.4.2 Effect of Geometry

The dimensionless radial acoustic particle velocity distributions for the *W/H*=0.9 rectangular cavity are displayed in Figure 3-15 as a function of angle Ø along the shear layer circumference at the upstream cavity corner and in the counter-clockwise direction.

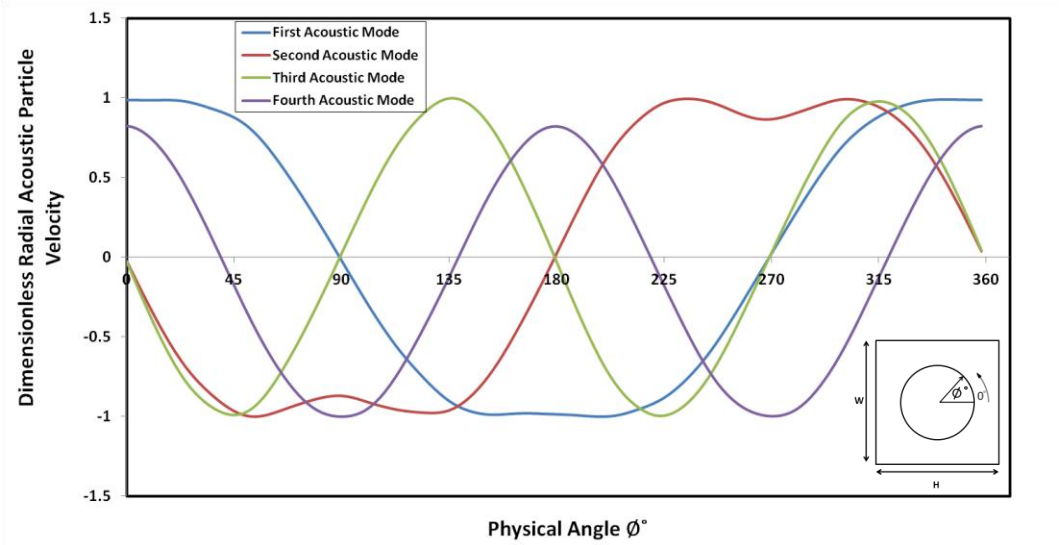

Figure 3-15: Dimensionless Acoustic Particle velocity distributions of the four acoustic modes for the rectangular, *W/H*=0.9, cavity. All cases correspond to the upstream cavity corner

Due to the asymmetry present within the *W/H*=0.9 rectangular cavity, disparity between the radial acoustic particle velocity distributions is observed between the two orthogonal modes. For the first acoustic mode corresponding to the larger height, *H*, the radial particle velocity remains fairly constant along its two circumferential sections in the ranges of 135-225° and 315-45 °with a slight drop in amplitude at the midpoints of the side lengths at 0° and 180°. However, in the case of the second acoustic mode, which is situated along the smaller width, *W*, the drop in acoustic particle velocity occurring at 90° and 270° is much more significant with an overall reduction of 15%.

The discrepancy between the two distributions are a result of the second acoustic mode being less trapped and closer to the piping circumference, leading

to a reduction in the pressure gradient and resultant radial acoustic particle velocity. Similar behaviour is observed through comparing the distributions of second acoustic mode for each of the three simulated cavity geometries, shown in Figure 3-16.

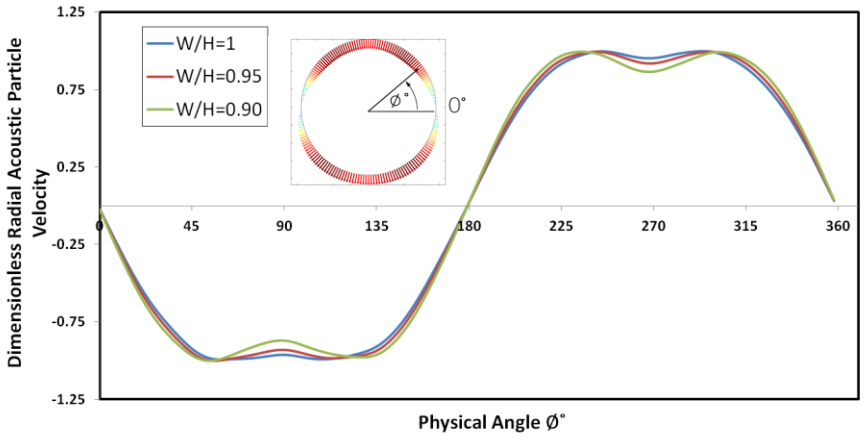

Figure 3-16: Comparison of dimensionless radial particle velocity distribution for the second acoustic mode as a function of angle, Ø, along the upstream cavity corner of the three cavity geometries

Once again, the reduction in acoustic particle velocity around 90° and 270° becomes larger as the cavity becomes smaller and more asymmetric. Nonetheless, this behaviour is not observed for all four trapped modes with changes in cross-sectional geometry. Comparisons of the particle velocity distributions of the third acoustic mode are shown in Figure 3-17.

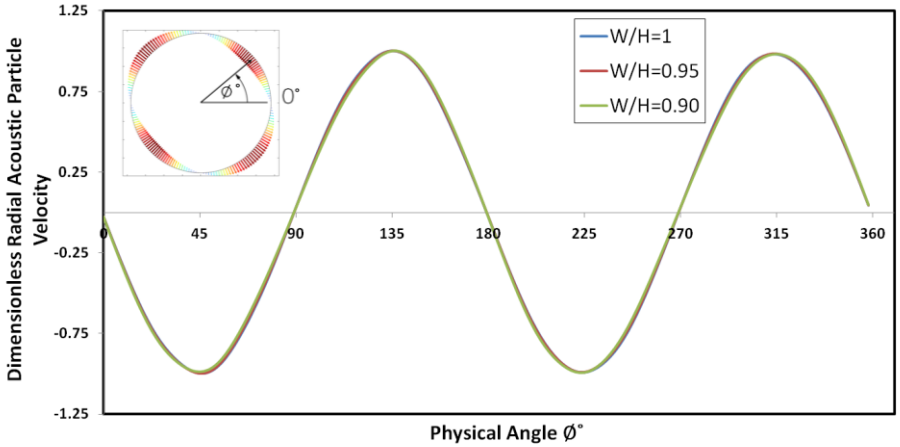

Figure 3-17: Comparison of dimensionless radial particle velocity distribution for the third acoustic mode as a function of angle, Ø, along the upstream cavity corner of the three cavity geometries

As can be seen in Figure 3.17, with the introduction of asymmetry and a reduction in cross-sectional geometry, the dimensionless acoustic particle velocity distribution remains constant. The acoustic mode shape consists of the anti-nodes being situated within the corners of the cavity. With slight variations in *W*, the acoustic mode shape and trapped nature is not greatly influenced. This type of behaviour is also observed from the first acoustic mode, Appendix A, where the mode shape is associated to the constant height, *H*.

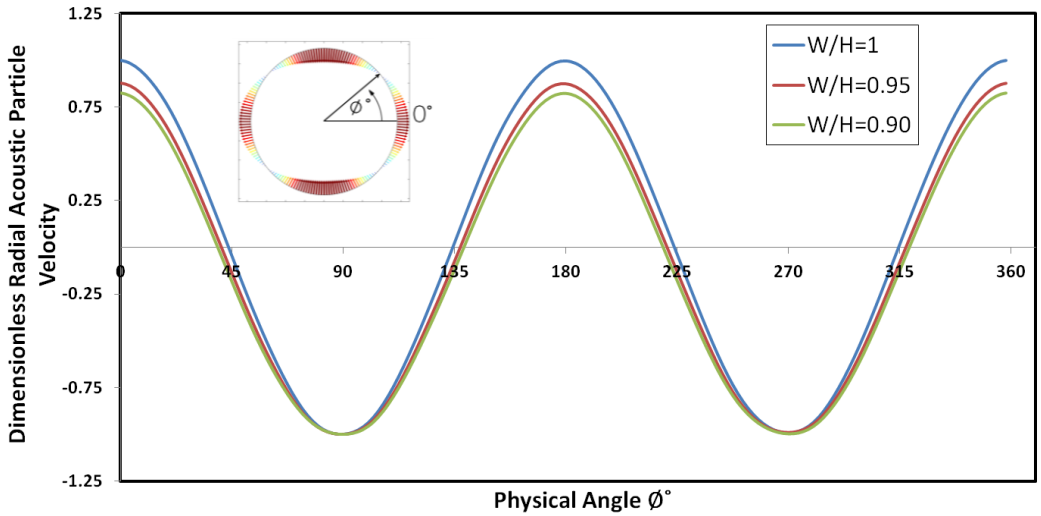

Figure 3-18: Comparison of dimensionless radial particle velocity distribution for the fourth acoustic mode as a function of angle, Ø, along the upstream cavity corner of the three cavity geometries

The distributions of the fourth acoustic mode with variations in geometry are displayed in Figure 3-18.The fourth acoustic mode shape, corresponding to the anti-nodes within the centers of the perimeter, is greatly influenced by changes in geometry. In the case of the square cavity, the anti-nodes are situated at the same radial distance away from cylindrical duct wall and have equivalent dimensionless acoustic particle velocity amplitudes. With a reduction in the width, and the introduction of asymmetry, the radial distance between the two pairs of anti-nodes and the duct wall alters. This causes the reduction in the dimensionless radial acoustic particle velocity within the ranges of 315-45˚ and 135-225˚ as displayed in Figure 3-18.

3.5 Instrumentation

3.5.1 Dynamic Pressure Transducers

Four PCB piezoelectric dynamic pressure transducers were installed flush along the cavity interior. The locations of these transducers are placed within the anti-nodes of the four trapped acoustic modes, as shown in Figure 3-19. The first two pressure transducers, PT1 & PT2, were installed at the middle of the width, *W*, and height, *H*, coinciding to the anti-nodes of the fourth acoustic mode. The remaining two dynamic pressure transducers, PT3 & PT4, are located within two corners of the cavity coinciding to the anti-nodes of the first three acoustic modes. These four transducers are used simultaneously during measurements to ensure that the maximum acoustic pressure amplitude and a relative phase distribution were obtained during the excitation of each of the four trapped acoustic modes.

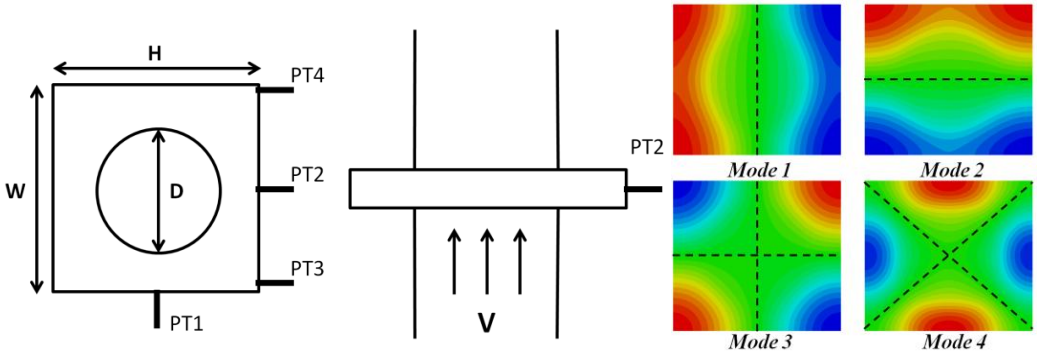

Figure 3-19: Location of four installed dynamic pressure transducers (PT1-4) in comparison to the four simulated mode shapes

The dynamic pressure transducers are equipped with an acceleration compensation sensing element to reduce the influence of vibrations on the signal. The sensitivity of the transducer is 7.3mV/kPa and has a resonance frequency of 250kHz. Data analysis is conducted through a 4-channel National Instruments NI-9233 data acquisition card with 24-Bit resolution attached to a Kistler type 5134 Coupler.

3.5.2 Pitot Tube

A pitot-tube is positioned at the centerline of the pipe and measures the dynamic head directly after the bell-mouth inlet. It is connected to a Validyne diaphragm DP15-42 differential pressure transducer and calibrated using a Ralston DPPV-0000 pump and Crystal S33-36/300PSI external pressure calibrator consisting of a 0.05% reading accuracy and attached to a Validyne Model CD23 Digital display. To avoid the pitot-tube influencing the downstream flow field and the excitation of the four acoustic modes, the velocity measurements were conducted separately from the acoustic measurements, where the pitot-tube was removed during the latter.

3.5.3 LDV

The upstream velocity profile was measured at 1.5 pipe diameters upstream from the mouth of the cavity using backscatter Laser Doppler Velocimetry (LDV). The TSI LDV system consisted of a Melles Griot Series 543 Argon laser producing output in the violet to green spectral regime. The laser beam was emitted into a fiberlight Multicolor Beam Separator, Model FBL-2, separating the light into three specified wavelengths corresponding to each velocity component. The light is then transferred through fiber optics to the measurement probe. The measurement probe emits two beams, for each velocity component, and measures the scattered light intensity through a photo detector. In backscattering LDV measurements, the same lens is used to focus the two intersecting laser beams as well as to collect the scattered light. The system consists of a PDM 1000 Photo Detector Module and a FSA 4000 Multibit Signal Processor. Measurements were done through Flowsizer software supplied by TSI.

Laser Doppler Velocimetry was utilized to obtain the streamwise velocity profile at both pre-resonance and resonance conditions for the square cavity. The measurements were taken at the centerline of the pipe to avoid refractions from the pipe curvature. As measurements became closer to the inner pipe diameter, direct reflections became dominant. To account for these reflections, the

measurement probe was rotated 5 degrees to allow closer measurements near the boundary layer. These rotated results were compared and found to be consistent to the non-rotated measurements which were performed to obtain the mean velocity profile. Within the non-rotated results, the turbulence intensity was approximately 2.5% at the centerline of the pipe for both pre-resonance and resonance conditions.

A self-evaporating seeding material, BIS(2-ethylhexyl) sebacate, having a technical grade of 90% and a particle diameter of 1μm was used for the LDV measurements. The measurements were zeroed at the wall location coinciding with a high data rate signal of zero flow velocity. This zeroing procedure was repeated to ensure consistency. Measurements start from 1.0 mm, as tests closer to the wall encountered difficulty in obtaining a sufficient data rate and burst efficiency. This was due to high reflections and lack of seeding particles. The measurements were conducted at intervals as small as 0.01mm through utilizing an isel Transverse Controller with a minimum step size of 0.00625mm.

3.5.4 Particle Image Velocimetry (Qualitative Flow Visualization)

The non-uniform excitation of the shear layer, as depicted by the radial acoustic velocity distribution, forms a highly three-dimensional transient flow field. Flow visualization consisted of phase-locked two-dimensional particle image velocimetry (PIV). The objective of these measurements was not to obtain a full quantitative representation of the three-dimensional flow field, but to visualize the downstream propagation of disturbances at specific circumferential sections along the shear layer and compare it to the distinct acoustic modal behaviours that were being observed. All measurements were conducted on the square, W/H=1, cavity due to three unique modal behaviours observed throughout its response, including simultaneous excitation of two acoustic modes and a spinning behaviour of degenerate modes. The PIV experimental setup was supplied by TSI and consisted of a New-Wave Solo 120 XT pulsed Nd: YAG

laser emitting a laser plane at 532nm at the maximum output of 120mJ/pulse. Two separate orthogonal measurement planes located at the midpoint of the height , *H*, and the width, *W*, were utilized as shown in views A-A and B-B within Figure 3-20. A PowerView (sign) 4-MegaPixel 12 bit camera with a resolution of 2048X2048pixel is positioned orthogonal to the emitted laser plane, taking rapidly consecutive images to acquire the domain's flow field.

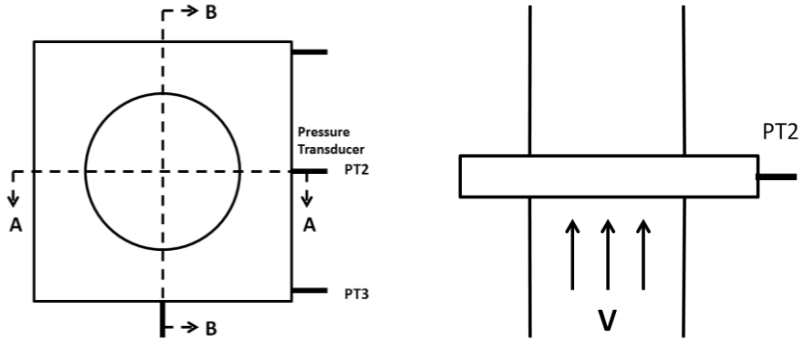

Figure 3-20: Schematic illustrating the two orthogonal measurement planes denoted by views A-A and B-B

Two orthogonal measurement domains were selected to compare the phases of the disturbances at 90˚ intervals along the shear layer circumference. The midpoints of the cavity were chosen due to ease of optical access as well as the locations coinciding with the anti-node of the fourth acoustic mode and the nodal lines for the third acoustic mode. An isometric view of the PIV setup, including the laser sheet and a cross-sectional image of the A-A measurement domain, is shown in Figure 3-21.

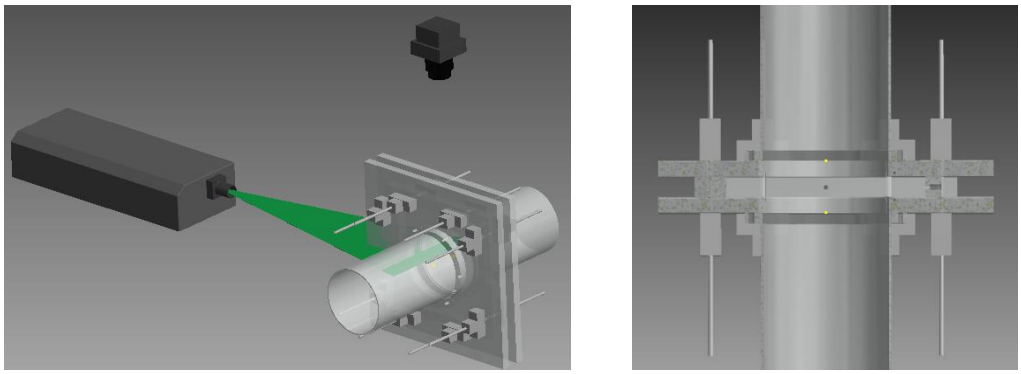

Figure 3-21: Isometric model illustrating the PIV test setup and A-A measurement plane

To remove unnecessary reflections present within the cavity, threaded rods obstructing the view were removed and replaced with external clamps and pipe edges were coated with black vinyl to remove any additional reflections arising from the curvature of the pipe. A self-evaporating seeding material, BIS(2-ethylhexyl) sebacate, having a technical grade of 90% and a particle diameter of 1μm, was used to reduce seeding buildup within the cavity. The seeding material was emitted using a six-nozzle Laskin aerosol generator and applied outside the suction of the test setup to mix with the ambient air.

At the higher flow velocities, an excessive build up of seeding material would occur on the walls of the cavity interior. This would blur out the images, as well as refract the light plane when entering the cavity. Care was taken to reduce this buildup for the higher order modes, allowing quick measurements in succession as well as cleaning the acrylic periodically from the seeding material.

Throughout the raw measurements, the downstream travelling vortices are clearly outlined by the absence of seeding particles within their core. This behaviour is due to the strong vorticity from the excessively strong excitation of the acoustic trapped modes. The formed vortices add a centripetal force, causing the seeding particles to be directed outwards in the radial direction depleting its central core (Durst, 1981). This trend occurs in all of the measured cases and causes problems when calculating the velocity/vorticity vectors within the core of the disturbances due to there being no particles to correlate between the two consecutive images.

The vector fields were resolved from INSIGHT 3G software supplied by TSI. The fields were processed using a multi-step deformation scheme starting with an interrogation region of 32x32 to a final grid size of 16x16. As well, a local median vector validation processor in conjunction with a local mean recursive filling validation method was utilized to interpolate the vectors within the core of the vortices. The interrogated holes are sorted by the number of valid

neighbour vectors. This process first fills the holes with the most valid neighbour vectors. From these now resolved vectors, the holes with the second most validated neighbours are then filled and so forth. Once again, the purpose of this investigation is merely visualizing the development of vortical structures from the excited acoustic modes. It is not to measure these flow parameters quantitatively within a two-dimensional plane, as the flow field is highly three-dimensional within the whole cavity.

Phase-averaging consisted of capturing and averaging a minimum of 250 instantaneous flow fields at equal interval phases in an acoustic cycle. The images were triggered off by one of two dynamic pressure transducers depending on the acoustic mode under investigation. For analysis involving the degenerate spinning mode and the fourth acoustic mode, triggering was done using the time signal of PT2 which is located in the middle of the width, *W*. Likewise, the time signal of PT3 was utilized during the excitation of the third acoustic mode due to its location within its anti-node. Triggering off the acoustic cycle was done using a custom build triggering circuit, and the synchronization of the laser pulses was carried out using a TSI LaserPulse synchronizer Model 610035. To allow for the phase shift over the oscillation cycle a time delay was added between the trigger and the laser pulse to ensure proper measurements at equal phase increments.

The excitation of the trapped acoustic modes is highly tonal and, in most cases, filtering the signal was unnecessary. However, in the simultaneous dual excitation of two modes, the measured time signals from the four transducers were complex and consisted of numerous spectral components. Thus, an Alligator Technologies USBPBP-S1 Butterworth band pass filter with adjustable cut-off frequencies was implemented to decompose the time signals into two separate sinusoidal signals. These two components corresponded to the resonant frequencies of each of the two acoustic modes. Phase-averaged PIV was then conducted along the acoustic cycle of each of these two simultaneously excited acoustic modes, comparing their downstream propagating structures.

CHAPTER 4
RESULTS AND DISCUSSION

4.1 Introduction

The following chapter presents the experimental results of the three investigated rectangular cavity geometries, utilizing the test facility detailed in Chapter 3. Comparisons of the three aeroacoustic responses are conducted in Section 4.2. First, the main characteristics of each of the three cavity geometries are presented. The effects of asymmetry (*W/H*) on the excitation of each of the four independent modes are then examined in accordance to their simulated mode shapes from Chapter 3. As well, the pressure drop across the cavities in comparison to their aeroacoustic responses is investigated. The upstream flow characteristics during both pre-resonance and resonance conditions are documented in Section 4-3.

Through observations of the acoustic spectra and instantaneous time signals, three unique modal behaviours were encountered. These include the excitation of stationary modes independently and simultaneous, as well as a spinning mode within the symmetric square cavity. Section 4.4, investigates the complex interaction between the resonant sound field and the propagation of vortical structures in each of the three observed behaviours. Analysis of the resonant sound field was done through resolved radial acoustic particle velocity distributions at the upstream edge of the cavity. While qualitative flow visualization, utilizing two-dimensional phase-averaged PIV, is applied to compare these acoustic particle velocity distributions with the corresponding initiation and propagation of vortical structures.

4.2 Aeroacoustic Measurements

4.2.1 Measurement Procedure

The aeroacoustic measurements consisted of simultaneously recording the time signals of the four separate dynamic pressure transducers (PT1-PT4) and resolving their corresponding RMS acoustic spectra. These acoustic pressure spectra were recorded at mean flow velocity divisions up to the maximum capacity of the blower. The sampling rate for the time signals was 25kHz, and the acoustic spectra consisted of averaging fifty, 1 second long samples with a final resolution of 1Hz. An example of one such spectra, measured for the *W/H*=0.9 rectangular cavity at a flow velocity of 83m/s, is shown below in Figure 4-1.

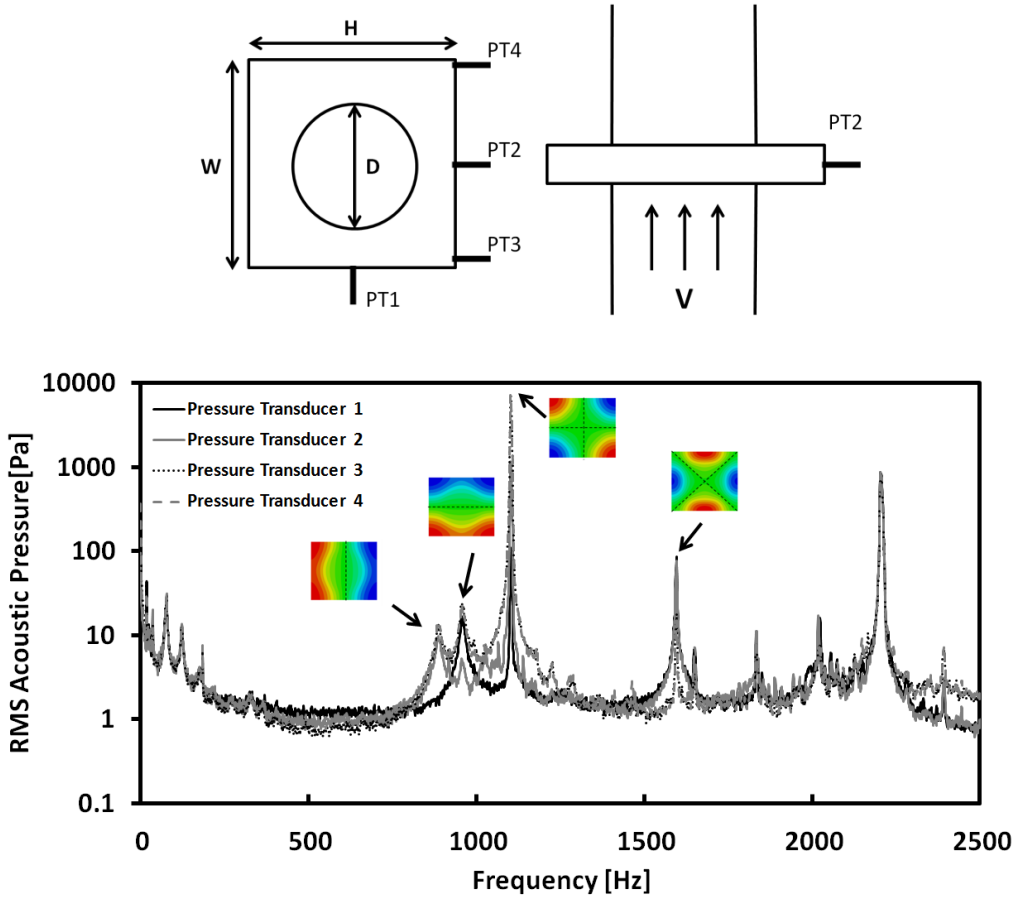

Figure 4-1: Acoustic pressure spectra of each of the four dynamic pressure transducers for the rectangular *W/H*=0.9 cavity, 83m/s

As clearly shown, the four dynamic pressure transducers measure separate pulsation amplitudes depending on their spatial position in accordance to the excited acoustic mode shape. For the above case, the third acoustic mode, *f3*=1102Hz, is prevalent and the anti-nodes are positioned within the corner of the cavity, corresponding to the location of PT3 and PT4. Thus, these pressure transducers record larger pulsation amplitudes than PT1 and PT2, which are likewise located within the node. Nonlinear effects are also observed as indicated by the sharp peak of the harmonic, 2*f3*=2204Hz, for all four transducers.

Through evaluation of the four pressure signals simultaneously, a full aeroacoustic representation of the four trapped acoustic modes can be deduced. Figure 4-2 is a Sound Pressure Level contour plot (reference 20μPa) for the *W/H*=0.9 rectangular cavity. The plotted SPL value is that recorded by the transducer which gives the largest pressure fluctuation at each frequency. This process was repeated for each flow velocity measurement up to the maximum capacity of the blower.

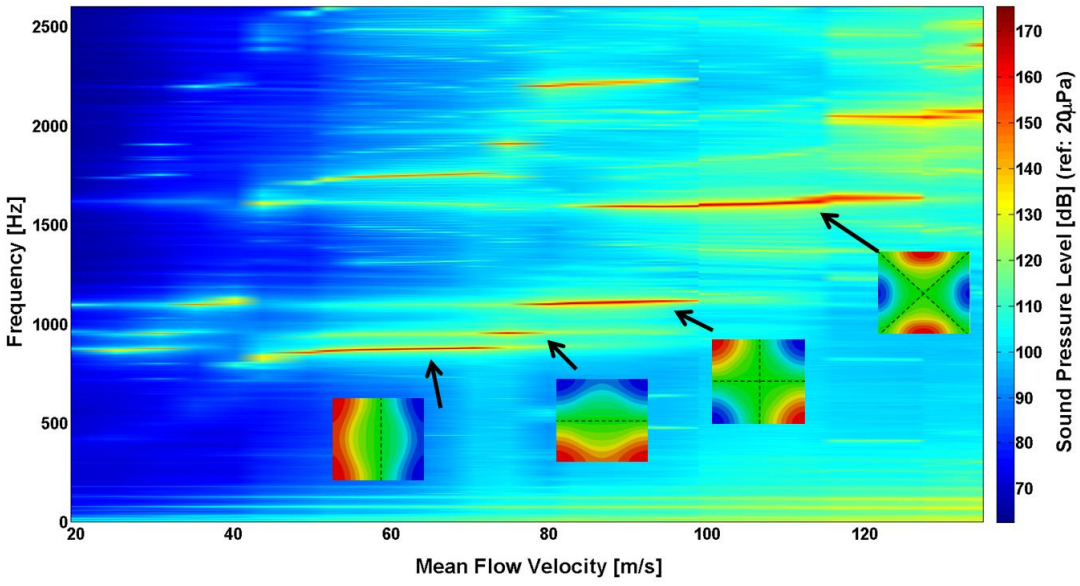

Figure 4-2: SPL contour plot of the aeroacoustic response for the rectangular, *W/H*=0.9, cavity

As clearly indicated, the aeroacoustic response of the *W/H=0.9* cavity is highly dominated by the tonal excitation of the four trapped diametral modes. The recorded pulsation amplitudes are very strong with a maximum measured SPL of 175dB from the excitation of the first acoustic mode. This prevailing behaviour of the four acoustic trapped modes occurs for all three tested cavities, with the strongest overall excitation of 177dB arising from the excitation of the degenerate and the fourth acoustic mode within the square cavity.

As discussed earlier, an additional fifth acoustic mode was observed both in simulations and experiments. This mode is not investigated in detail due to additional complexity from its modal shape. At flow velocities near the maximum capacity of the blower, the response becomes even more complicated as multiple higher order acoustic modes are excited simultaneously and the response distorts into a more broadband behaviour. The resonant frequencies of these four trapped acoustic modes are in good agreement to those resolved from numerical simulations, as shown in Table 4-1. The recorded experimental frequency is the average along its excitation range, due to slight variations as the mean flow velocity is altered. This agreement between simulations and experiments is consistent for all three tested cavities.

Table 4-1: Comparisons of experimental resonant frequencies to simulated resonant frequencies for the four trapped modes in the *W/H*=0.9 rectangular cavity

	Resonant Frequencies (Hz)			
	f1	***f2***	***f3***	***f4***
Simulation	878	954	1097	1610
Experiment	872	952	1104	1605

4.2.2 General Behaviour of the Trapped Diametral Modes

Figures 4-3 and 4-4 present comparisons of the four trapped diametral acoustic modes for the *W/H=0.9* rectangular cavity, detailing their pulsation amplitudes and resonant frequencies along their flow velocity range of excitation. The recorded acoustic pressure is the maximum RMS value simultaneously recorded from the four separate dynamic pressure transducers at each of the resonant frequencies.

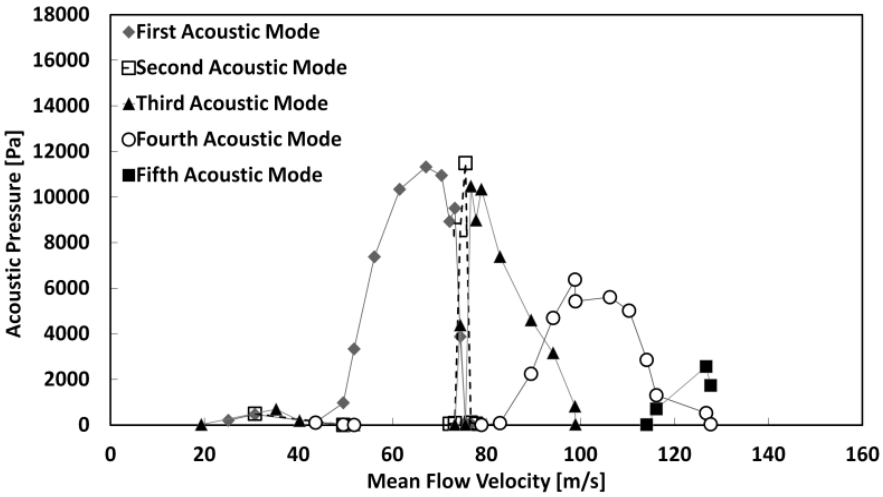

Figure 4-3: Aeroacoustic response of the *W/H=0.9* cavity, detailing pulsation amplitudes of each of the four dominant trapped acoustic modes

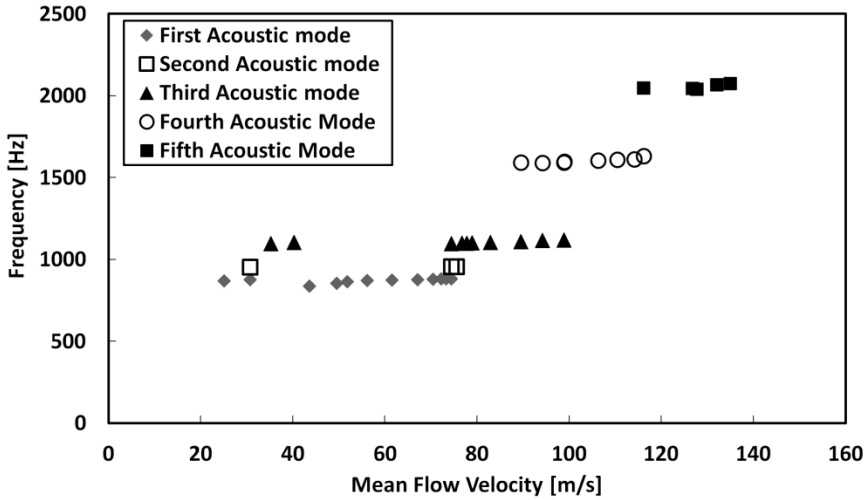

Figure 4-4: Associated resonant frequencies corresponding to the above dominant pressure pulsations, indicating jumps in resonant frequency with increase in flow velocity

As displayed in the above figures, the trapped acoustic modes are excited along two separate flow velocity ranges. The first three modes are weakly excited within the range of 20-40m/s and all four trapped modes are strongly excited within the range of 50-130m/s with significantly higher pulsation amplitudes. Along each of these velocity ranges, the frequency jumps from one acoustic mode to the next in sequence of its defined modal number. These frequency jumps occur with an increase in flow velocity. This behaviour is a common characteristic found within flow-excited acoustic resonance present within cavities (Schachenmann & Rockwell, 1982).

The two velocity ranges represent two different hydrodynamic modes of the shear layer instability exciting the trapped acoustic modes. The free shear layer modal number, n, designates the number of vortices (wavelengths) present along the cavity length during an acoustic cycle. From inspection of the aeroacoustic response, the four trapped acoustic modes are excited by the first two (n=1, 2) free shear layer oscillation modes corresponding to one or two vortices being convected downstream the length of the cavity. These oscillations only occur at predefined frequencies, determined by their respective dimensionless Strouhal number defined as:

$$St_L = \frac{fL}{U} \tag{4.1}$$

where f represents the resonant frequency, L represents the cavity length (constant at 25.4mm), and U represents the mean flow velocity. Figure 4-5 presents the Strouhal number of each of the four trapped modes during the two velocity ranges of excitation. Likewise, Figure 4-6 presents the dimensionless acoustic pressure of these modes at the corresponding Strouhal numbers. The dimensionless acoustic pressure is the RMS acoustic pressure, P, normalized by the dynamic head ($1/2\rho U^2$).

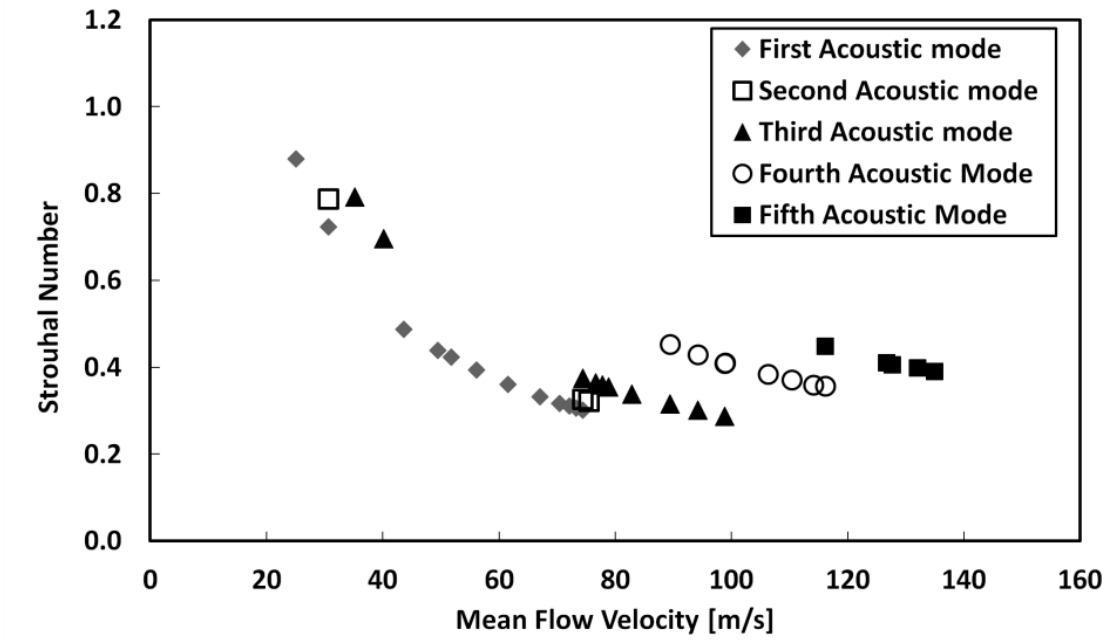

Figure 4-5: Strouhal number as a function of the mean flow velocity during the dominant excitation of the four trapped acoustic modes of the cavity with *W/H*=0.9

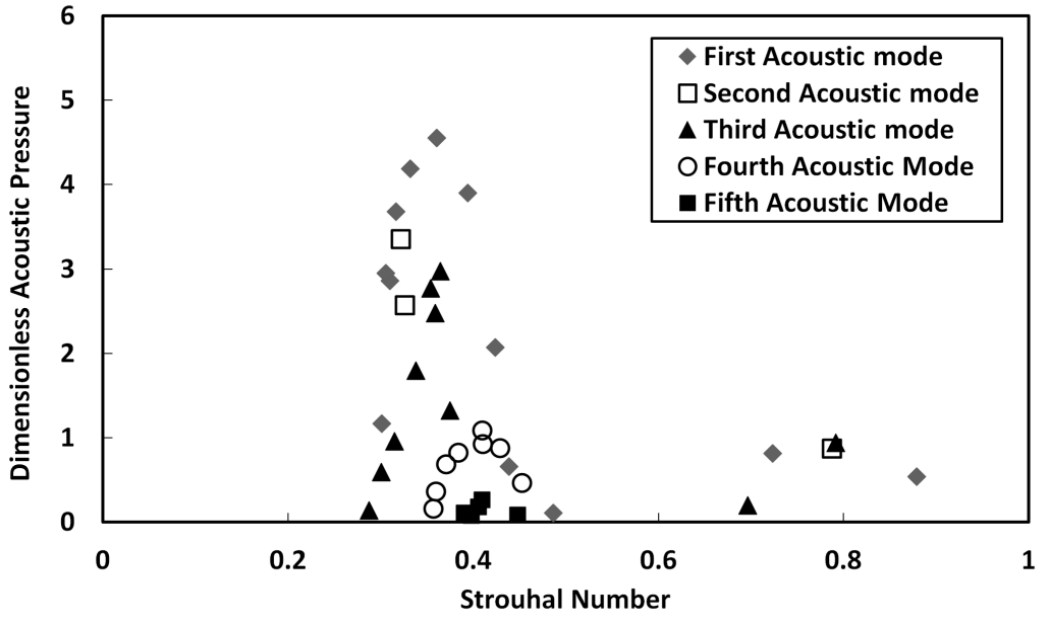

Figure 4-6: Dimensionless acoustic pressure of the dominant acoustic modes as a function of the Strouhal number for the cavity with, *W/H*=0.9.

As clearly shown from the above plots, the two flow velocity ranges of excitation represent two distinct ranges of Strouhal numbers. The first range, St=0.3-0.5, corresponds to the first shear layer mode and represents the

propagation of one vortical structure along the cavity length. This shear layer mode excites the trapped modes at the flow velocity range of 50-140m/s and coincides with the very strong pressure pulsations observed in Figure 4-3. The four trapped modes are also excited from 20-40m/s by the second shear-layer mode, with a Strouhal number range of St=0.7-0.9. However, it generates comparably weaker acoustic resonance as observed from the significant difference in the maximum dimensionless acoustic pressure at the two Strouhal numbers.

These two Strouhal number ranges are consistent for all three tested cavity geometries, as shown in a similar plot for the square cavity in Figure 4-7. However, depending on the relative strength of each of the excited acoustic modes, the individual Strouhal number range may slightly vary. As shown in Figure 4-6 and 4-7, the Strouhal range of the fourth acoustic mode is significantly larger than that of the *W/H*=0.9 cavity. This is due to the excitation of the fourth mode being stronger and occurring over a longer velocity range. Nonetheless, the onset Strouhal number for the fourth mode, corresponding to the onset excitation velocity, remains constant for all tested cavities with a value around St=0.5.

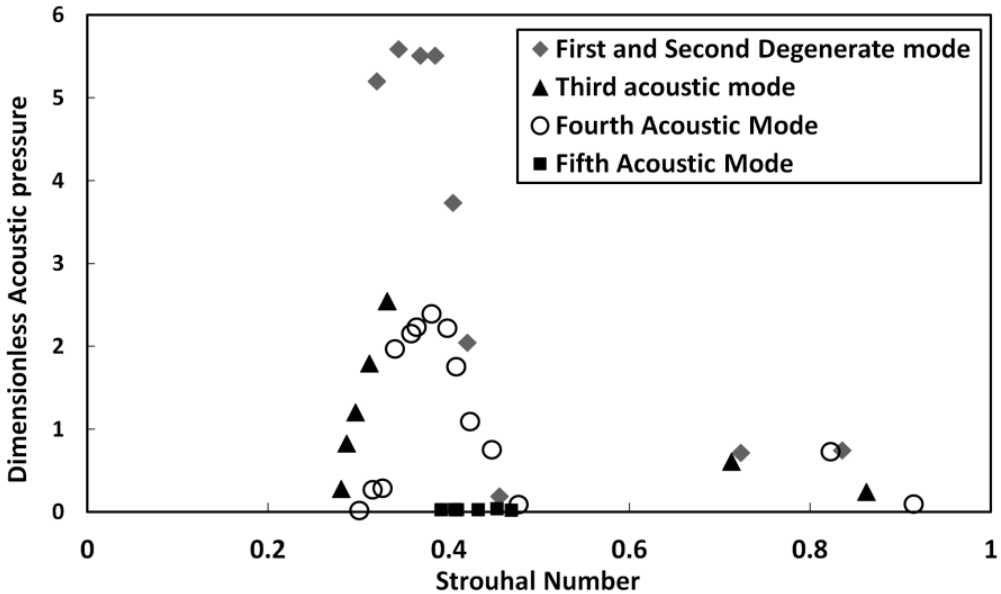

Figure 4-7: Dimensionless acoustic pressure of the dominant acoustic modes as a function of the Strouhal number for the square, *W/H*=1, cavity

Figures 4-8, 4-9, and 4-11 illustrate the aeroacoustic responses of the three cavity geometries. For each of the three cases, strong acoustic resonance occurs within the flow velocity range of 50-130m/s triggered by the first shear layer mode. Only one trapped mode is usually excited and the switching to higher order modes occurs abruptly. However, simultaneous excitations of the third and fourth acoustic modes occur for all cavities in the velocity range of 80-100m/s. Within the lower velocity range of resonance (20-40m/s), where the excitation is caused by the second shear-layer mode, much smaller pulsation amplitudes are recorded and the excitation of the four trapped modes tends to be intermittent.

4.2.3 Effect of Geometry on Aeroacoustic Response

In the rectangular asymmetric geometries, Figures 4-8 and 4-9, the resonance of the second acoustic mode tends to be suppressed by the neighbouring resonance of the first and the third acoustic modes. Although the resonant frequencies of the first and the second modes are only slightly offset, around 50-100Hz, the excitation of the first mode is predominant along the majority of the velocity range from 50-80m/s. Then suddenly the second acoustic mode rises to high pulsation amplitudes at around 11000-12000kPa before it is soon after overcome by the excitation of the third mode.

During the switching of these acoustic modes, from 70-80m/s, only one mode is excited at a time which is represented by the dashed lines within these figures. This suppression effect is even more pronounced for the W/H=0.9 cavity, Figure 4-9, where smaller velocity increments were taken in order to inspect the resonance of the second acoustic mode.

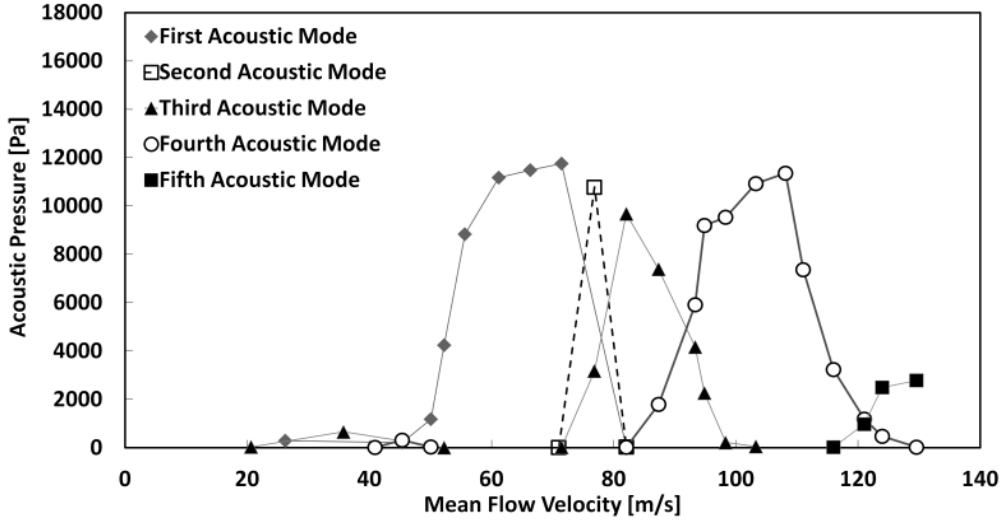

Figure 4-8: Aeroacoustic response detailing the excitation of each of the trapped modes for the rectangular, *W/H*=0.95, cavity

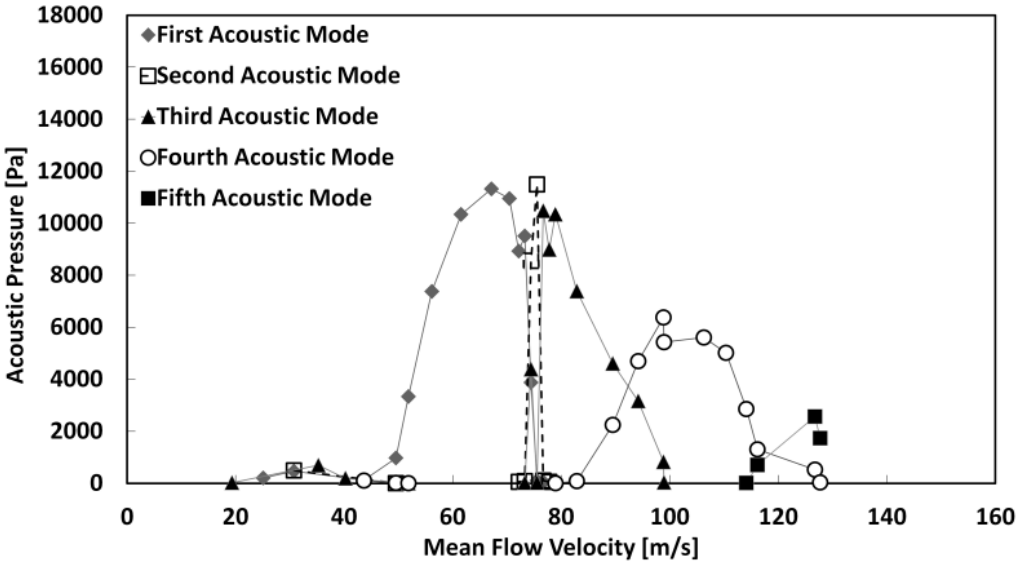

Figure 4-9: Aeroacoustic response detailing the excitation of each of the trapped modes for the rectangular, *W/H*=0.9, cavity

At the lower velocity ranges of the cavity with *W*/*H*=0.9, (25-35m/s), corresponding to the second shear-layer mode, the first and the second acoustic modes are excited simultaneously. Due to only a 50-100Hz difference in resonant frequencies, this dual excitation creates a beating phenomenon at the corner pressure transducers at a beating frequency equal to the difference of the two

resonant frequencies. The normalized time signals of the beating phenomenon are shown in Figure 4-10 for the *W/H*=0.9 cavity at 31m/s. This simultaneous excitation, however, only occurs when the acoustic pressure amplitudes are quite small, at around 500Pa, in comparison to the much stronger amplitudes, 11500Pa, found at higher flow velocities. Due to these low excitation levels, emphasis will be placed on the strong resonance caused by the first shear-layer mode.

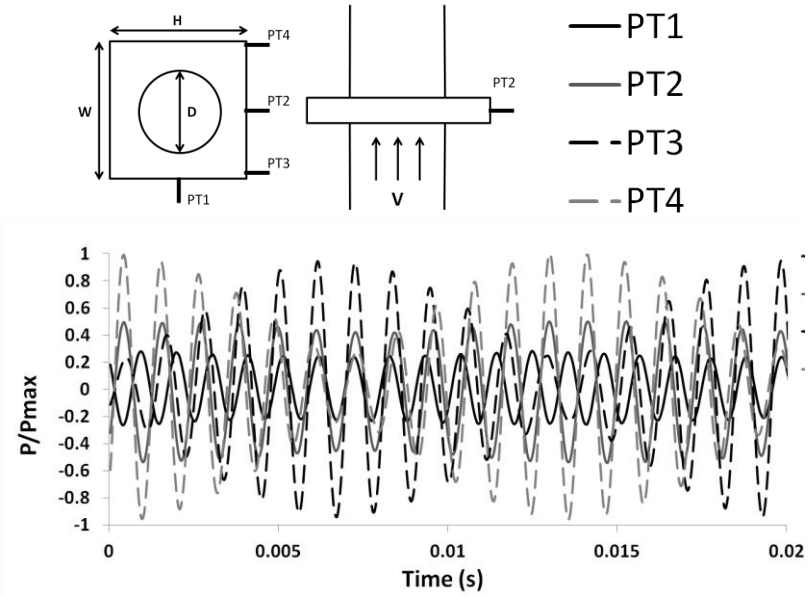

Figure 4-10: Dimensionless pressure signals indicating beating at the corner pressure transducers, *W/H*=0.9 cavity, 31m/s

In the case of the square cavity, Figure 4-11, the first and second orthogonal modes are degenerate as they have the same resonant frequency. As will be investigated within the next section, the resonance of this acoustic mode was observed to be spinning due to the inherent symmetry present within the cavity cross-sectional geometry. The square cavity recorded the largest pulsation amplitudes of approximately 14500Pa from either excitation of the degenerate or the fourth acoustic mode. Despite having similar frequencies and dimensions to the first two modes within the rectangular cavities, the degenerate mode has a significant increase in acoustic pressure. This increase in acoustic energy through degeneracy was also observed by Aly through the installation and removal of a splitter plate within an axisymmetric cavity (Aly & Ziada, 2011).

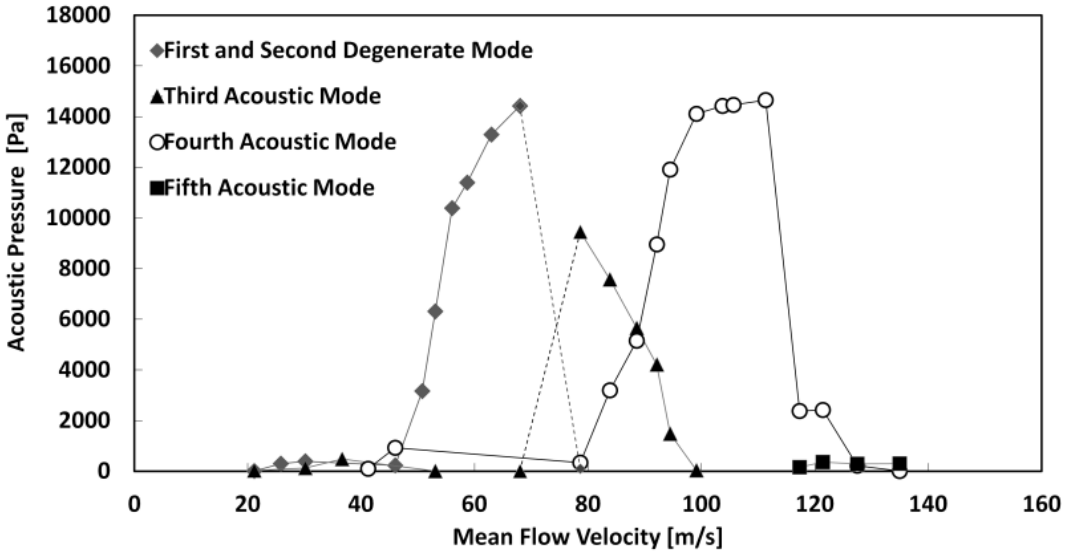

Figure 4-11: Aeroacoustic response detailing the excitation of each of the trapped modes for the square, *W/H=1*, cavity

Figures 4-8, 4-9 and 4-11 illustrate some general trends of the excitation of the trapped modes as the cross-sectional cavity dimensions are altered. With the exception of the degenerate mode, the acoustic pressure amplitudes of the first three acoustic trapped modes remain nearly constant with minor variations in the cavity geometry. For these mode shapes, the acoustic energy is predominantly confined within the corners of the cavity and is hardly affected with small variations in the width. This results in only slight changes in pressure amplitudes for the first two modes and insignificant changes in the third.

However, in the case of the fourth acoustic mode, the anti-nodes are located at the midpoint of the cavity side lengths. As the cavity becomes smaller, through reduction in *W*, the acoustic energy becomes less confined within the cavity domain resulting in an increasingly less trapped acoustic mode. This is observed through the large 9000Pa drop in acoustic pressure as the cavity width *W* is reduced from *W/H*=1 to *W/H*=0.9. This reduction in the confinement of acoustic energy has also been observed through comparisons of the simulated mode shapes and acoustic particle velocity distributions previously discussed in Chapter 3.

4.2.4 Effect on Pressure Drop

In gate valve applications, the strong excitation of the trapped diametral modes can lead to undesirable consequences including an increase in pressure drop across the valve, leading to lower overall plant efficiency. To investigate this effect on the current cavity geometries, eight static pressure taps located along the piping circumference 30cm upstream and downstream from the cavity corners were installed to account for the asymmetric nature of the modes. Figure 4-12 presents the pressure drop across the square, *W/H*=1.0, cavity during its aeroacoustic response.

As shown, the pressure drop across the cavity increases substantially during the strong acoustic resonance of the four trapped diametral modes. Particularly large peaks occur at 50-70m/s and 100-120m/s coinciding to excitation flow velocities of the predominant degenerate and fourth acoustic mode shown in Figure 4-11. This rise in pressure loss is due to the kinetic energy now being used to sustain the large acoustic resonance of the trapped modes. This behaviour is observed in all three cavity geometries, see Appendix A. As the cavities become smaller, and the resonance of the trapped modes becomes weaker, the pressure drop reduces in comparison.

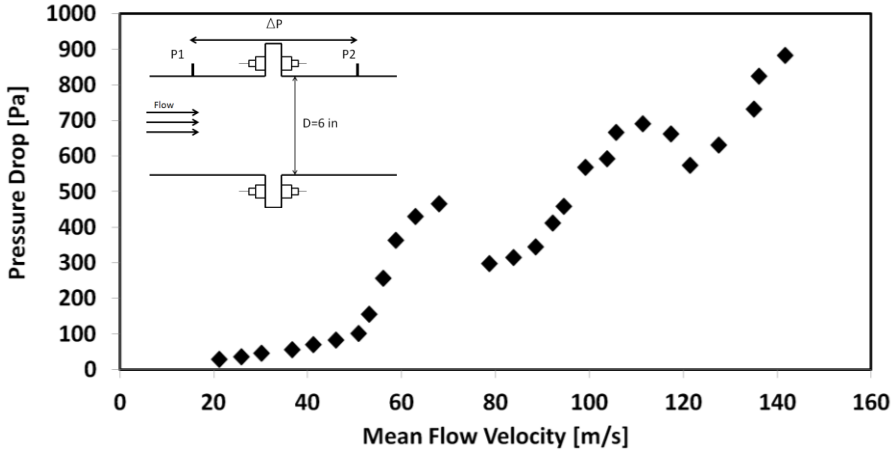

Figure 4-12: Static pressure drop across the square, *W/H*=1.0, cavity during its aeroacoustic response

4.3 Upstream Flow Conditions

The upstream boundary layer for the square cavity was measured using Laser Doppler Velocimetry (LDV). Two sets of measurements were conducted at pre-resonance, 36.5m/s, and resonance, 61m/s, conditions at one pipe diameter from the upstream shear layer. In both sets of measurements, the cavity centerline turbulence intensity normalized by the mean velocity measured at the bell mouth exit, is approximately 2.5%. Both resolved velocity profiles were flat with a boundary layer thickness of approximately 20mm. The mean velocity profile for the pre-resonance case, 36.5m/s, is shown in Figure 4-13 and the resonance case, 61m/s, is displayed in Figure 4-14.

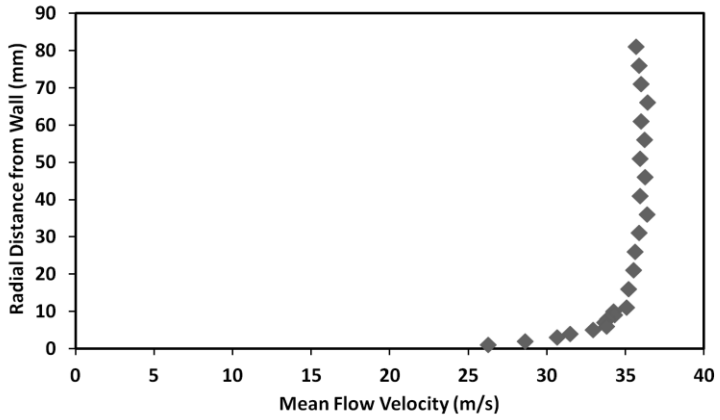

Figure 4-13: Radial profile of mean flow velocity measured one pipe diameter upstream of square cavity at pre-resonance conditions, 36.5m/s

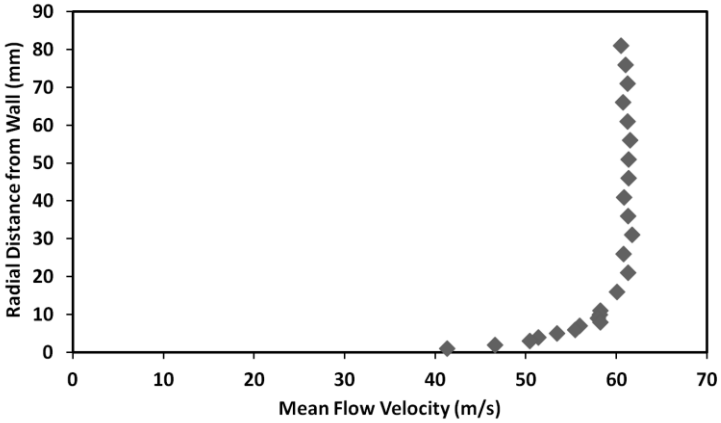

Figure 4-14: Radial profile of mean flow velocity measured one pipe diameter upstream of square cavity at resonance conditions, 61m/s

4.4 Modal Behaviours

Through observations of the experimental results, three distinct behaviours of the acoustic modes were encountered and investigated in regards to the interaction between the resonant sound field and the downstream propagating disturbances. These modal behaviours are classified as the following

1) *Excitation of a Single Stationary Trapped Diametral Mode*

2) *Simultaneous Excitation of Two Stationary Modes at Separate Frequencies*

3) *Simultaneous Excitation of Two Equivalent Orthogonal (Degenerate) Modes*

These three unique excitation mechanisms were studied through both the experimental results and numerical simulations. First, the modal behaviours were categorized through observations of the instantaneous time signals of each of the four dynamic pressure transducers. Numerical simulations were then conducted to resolve the resonant sound field and corresponding radial acoustic particle velocity distributions. Finally, the influence of the resonant sound field on the formation of vortical structures was investigated through two-dimensional qualitative phase-averaged PIV (Particle Image Velocimetry).

Due to the complex interaction between the acoustic particle velocity and the three-dimensional flow field, focus is placed on the shear layer near the cavity upstream corner where the development and propagation of the vortical disturbances is initiated. The following modal analysis was conducted on the square cavity, whose response is shown in Figure 4-11. This geometry was chosen due to the existence of all three described modal behaviours.

4.4.1 Excitation of a Single Stationary Trapped Diametral Mode

In most instances, the trapped acoustic modes are stationary, excited independently, and occur at separate flow velocities. As the mean flow velocity increases, the excited acoustic modes switch in sequence of their defined modal number. Due to the asymmetry inherent within the rectangular geometries, each of the first two acoustic modes has one unique mode shape, resulting in a stationary behaviour. This is different from the degenerate acoustic mode whose behaviour will be analyzed in Section 4.4.3.

As well, the higher order third and fourth acoustic modes are also stationary with the corners and the midpoints of the side lengths being the only possible orientation for their anti-nodes and nodal lines. Investigation on the independent excitation of stationary modes is conducted on both the third and fourth acoustic mode present within the square cavity. The fourth mode's dimensionless acoustic pressure and radial acoustic particle velocity distribution at the upstream cavity corner is displayed in Figure 4-15.

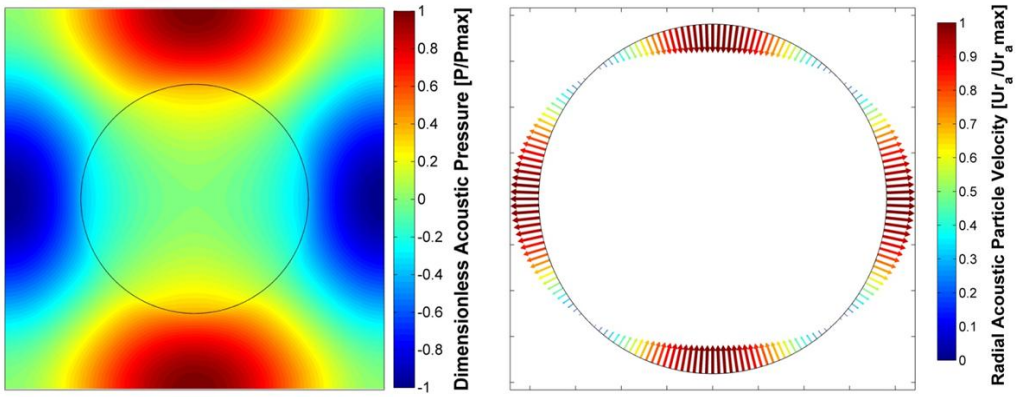

Figure 4-15: Normalized acoustic pressure and radial acoustic particle velocity distribution of the fourth acoustic mode at the upstream cavity corner, *W/H*=1, square cavity

As shown, the radial acoustic particle velocity distribution is *non-uniform* and is akin to its modal shape. The amplitude of the velocity fluctuations along the circumference corresponds to the relative azimuthal position of the acoustic pressure. Thus, the radial velocity fluctuations are *maximum* at the locations of the

anti-nodes and *zero* at the nodal lines. This separates the radial particle velocity fluctuations into four circumferential sections. This varying azimuthal distribution causes a non-uniform triggering of the shear layer and development of vortical structures.

To investigate this non-uniform formation and propagation of disturbances, two-dimensional qualitative PIV was utilized. Due to the flow field and particle velocity distribution being highly three-dimensional along the shear layer circumference, four sections along the shear layer were investigated. These domains are physically separated by 90˚, and the field of view projections are represented by the dashed lines in Figure 4-16 (left). The projection of the 0˚ domain along the cavity length is shown in Figure 4-16 (right) as an example. This projection technique is exercised for the remaining PIV measurements within this chapter.

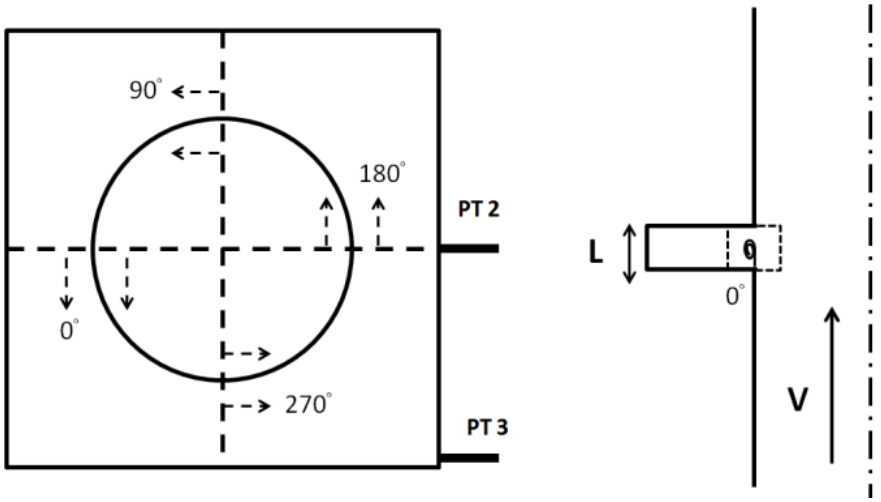

Figure 4-16: Schematic illustrating the four projected measurement domains and their respective field-of-view for PIV flow visualization. Phase-averaging through all tests was done through triggering by pressure transducers PT2 and PT3

In regards to the fourth acoustic mode, the four projected measurement domains coincide with the maximum radial acoustic particle velocity fluctuations. Those domains physically separated by an angle of 180˚ are in phase (with the

same velocity fluctuation amplitude and radial direction) and those domains that are orthogonal are completely out of phase (same fluctuation amplitudes but in opposite radial directions).

The PIV measurements, Figure 4-17, consist of phase-averaging 250 instantaneous vorticity fields at 90˚ temporal phase shifts, ϕ, along the fourth mode's acoustic cycle. Synchronization and triggering of the PIV was done via the instantaneous time signal of pressure transducer PT2. Measurements were conducted at a mean flow velocity of 104m/s and at the fourth mode's resonant frequency of 1480Hz. The four projected measurement domains are labelled by their defined physical angle (0˚, 90˚, 180˚, and 270˚) and illustrate the propagation of disturbances along the normalized cavity length (y/L) from the upstream to downstream cavity corners.

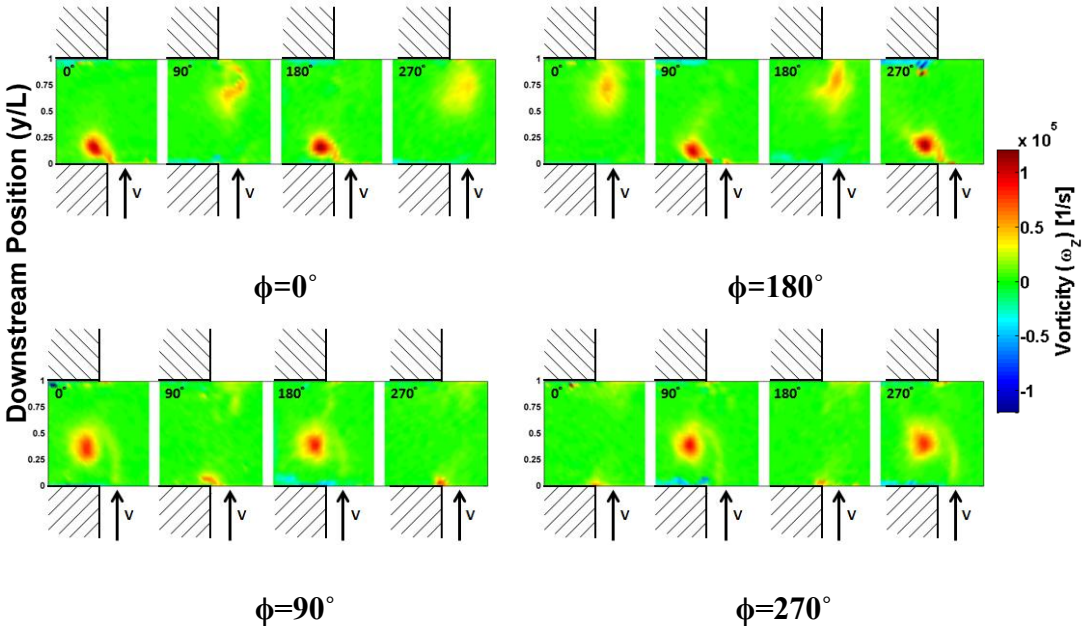

Figure 4-17: Phase-averaged vorticity fields during the excitation of the fourth acoustic mode for four instants during the acoustic cycle separated by 90˚ phase shifts, ϕ, *f4*=1480Hz, 104m/s

As illustrated by the average vorticity fields, the propagation of disturbances are non-uniform and akin to radial acoustic particle velocity distribution detailed

in Figure 4-15. Those domains that are separated by a physical angle of 180˚ show the formation of two parallel vortices which are in phase and at the same downstream distance along the cavity length, y/L. Those planes that are orthogonal to one another show two vortices completely out of phase by 180˚. This latter behaviour is evident through side-by-side comparisons of the ϕ = 0˚ and 180˚ vorticity fields.

A similar analysis was conducted on the third acoustic mode whose mode shape and radial acoustic particle velocity distributions are shown in Figure 4-18. Once again, the radial acoustic particle velocity distribution is akin to the acoustic pressure, with the anti-nodes corresponding to the maximum radial velocity fluctuations. The same four PIV measurement domains were used; however, these measurement locations now coincide within the nodes, where the radial acoustic particle velocity fluctuations are zero.

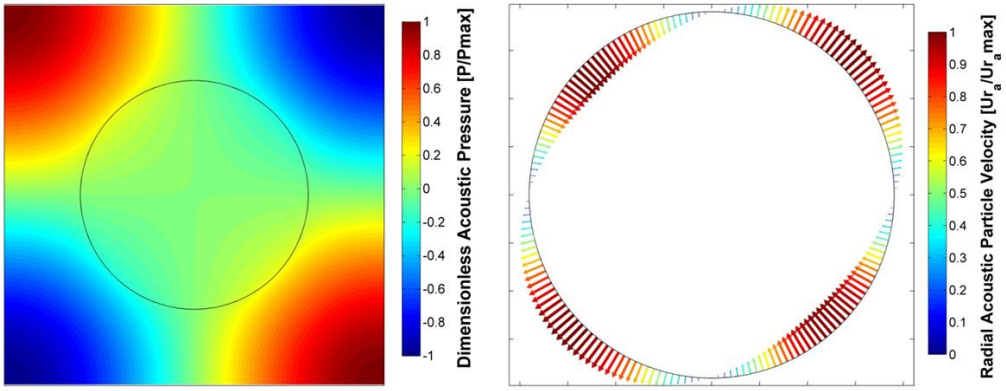

Figure 4-18: Normalized acoustic pressure and radial acoustic particle velocity distribution of the third acoustic mode at the upstream cavity corner, *W/H*=1, square cavity

Phase-averaged PIV was conducted at four separate temporal phase shifts, ϕ, separated by 90˚ along the third mode's acoustic cycle. Measurements were synchronized and triggered off the corner dynamic pressure transducer PT3 which is situated within the anti-node of the third mode. The measurements are

presented in Figure 4-19 and were conducted at a mean flow velocity of 81m/s and a resonant frequency of 1027Hz.

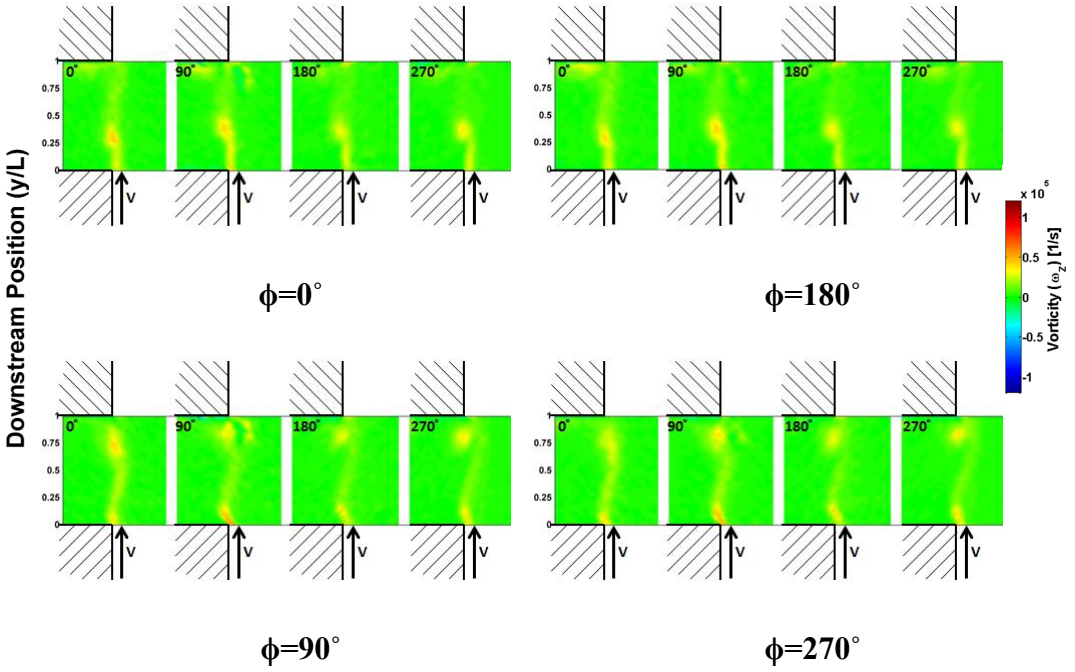

Figure 4-19: Phase-averaged vorticity fields during the excitation of the third acoustic mode for four instants during the acoustic cycle separated by 90° phase shifts, ϕ, *f3*=1027Hz, 81m/s

As illustrated from the phase-averaged vorticity fields, despite the measurement domains being situated at shear layer sections coinciding with zero radial velocity fluctuations, there is evidence of vortices being triggered and convected downstream. The vorticity magnitudes of these disturbances, however, are comparably much lower than that found from the excitation of the fourth acoustic mode. The vortex shedding in each of the four measurement domains are in phase and propagate down twice every acoustic cycle. This indicates that the shedding frequency coincides to the first harmonic of the third mode's resonant frequency and not at the fundamental.

The pressure transducer used to synchronize measurements along the acoustic cycle, PT3, is situated at the anti-node of the excited mode; however the measurement domains are located within the nodes coinciding to the positions of

pressure transducers PT1 and PT2. The acoustic spectra of PT2 and PT3 are shown in Figure 4-20. As expected, PT3 is dominated by the large pulsation amplitudes at the resonant frequency, *f3*=1027Hz. However, PT2's prevailing component is the first harmonic, 2*f3*=2054Hz.

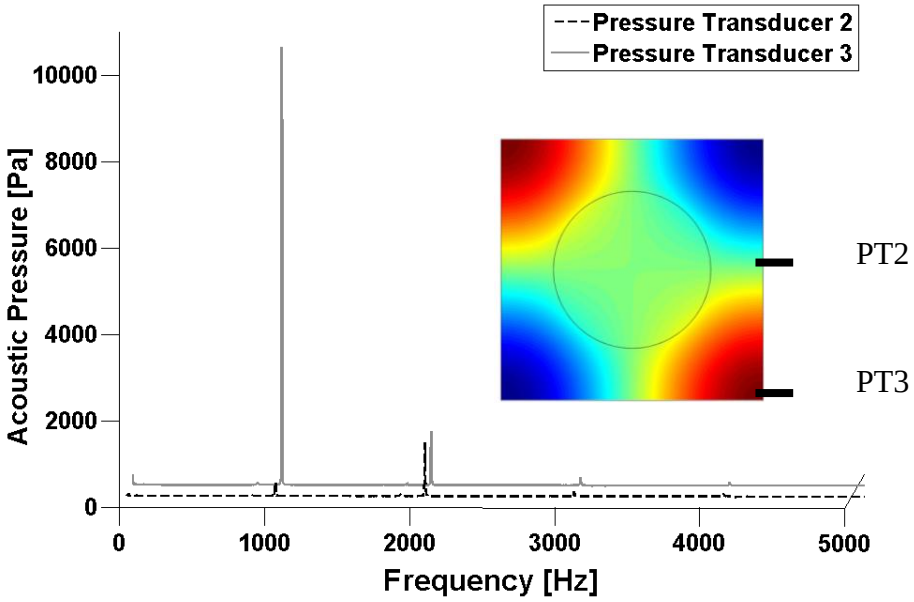

Figure 4-20: Acoustic spectra of pressure transducer PT2 and PT3 during the excitation of the third acoustic mode, 81m/s

This prevailing behaviour of the harmonic frequency is due to nonlinear effects becoming significant during the strong excitation of the acoustic modes. Although the fundamental frequency becomes insignificant at the node, the harmonic component is still prominent. This causes the shear layer at the node, being influenced by the acoustic pressure, to now being excited at the harmonic frequency initiating the formation of downstream propagating disturbances at twice the resonant frequency. Observations of the instantaneous time signals verify that the pressure signals of PT1 and PT2 are completely in phase, consistent to the in-phase formation and propagation of vortices in each of the four measurement domains. A similar behaviour is observed from the independent excitation of the fourth acoustic mode where the pressure transducer signals in the corner, located within the nodes, are dominated by the first harmonic frequency.

From observations of the previous two cases, the non-uniform radial acoustic particle velocity distribution results in a complex three-dimensional triggering of vortical structures along the shear layer circumference. The strong excitations of these trapped acoustic modes prove that a *uniform synchronized* excitation over the whole shear layer circumference is *not necessary* to maintain orderly and coherent vortical structures that sustain strong flow-acoustic coupling and produce strong acoustic resonance exceeding 170dB.

4.4.2 Simultaneous Excitation of Two Modes at Separate Frequencies

In the flow velocity range of 80-100m/s, simultaneous excitation of the third and fourth trapped acoustic modes is observed for all three tested cavities. Time averaged spectra at 92m/s for the *W/H*=1 square cavity, Figure 4-21, shows comparable pulsation amplitudes of each of the two excited acoustic modes.

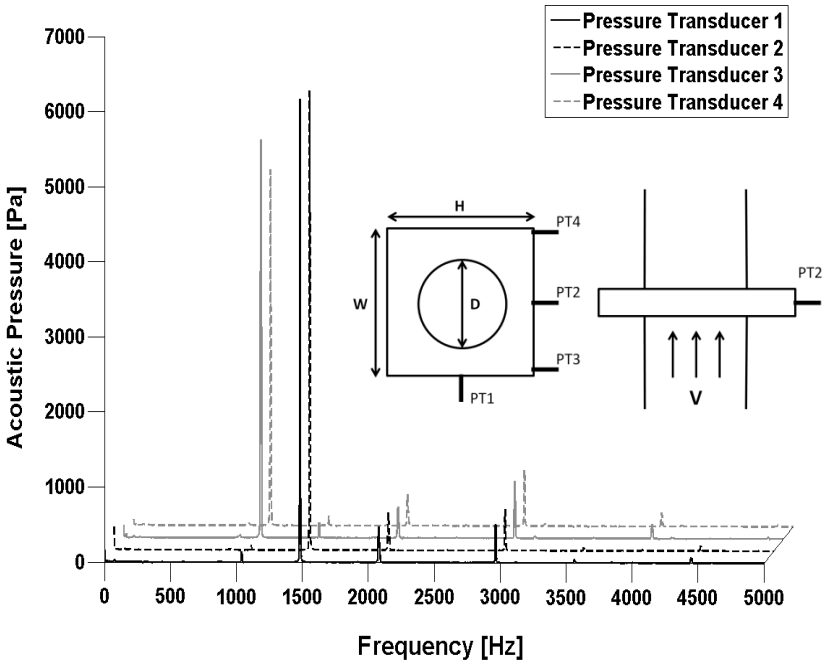

Figure 4-21: Time averaged acoustic spectra of the four pressure transducers during simultaneous excitation of the third and fourth acoustic mode for the square cavity at 92m/s

As observed from the relative amplitudes of the spectral peaks, the four dynamic pressure transducers are measuring different amplitudes of the third and

fourth acoustic modes depending on their measuring position in the mode shape. The first two pressure transducers, PT1 & PT2, located at the middle of the sidewalls, are measuring the maximum amplitude of the fourth acoustic mode, f_4=1490 Hz, while sensing negligible pressure amplitudes of the third acoustic mode, f_3 = 1033 Hz. This is because they are located at the anti-nodes of the fourth mode and the nodes of the third mode. Similarly the third and fourth transducers, PT 3 & PT4, are measuring the third acoustic mode with negligible amplitudes of the fourth. Normalized instantaneous time signals corresponding to the acoustic spectra are presented in Figures 4-22 for PT2 and Figure 4-23 for PT3.

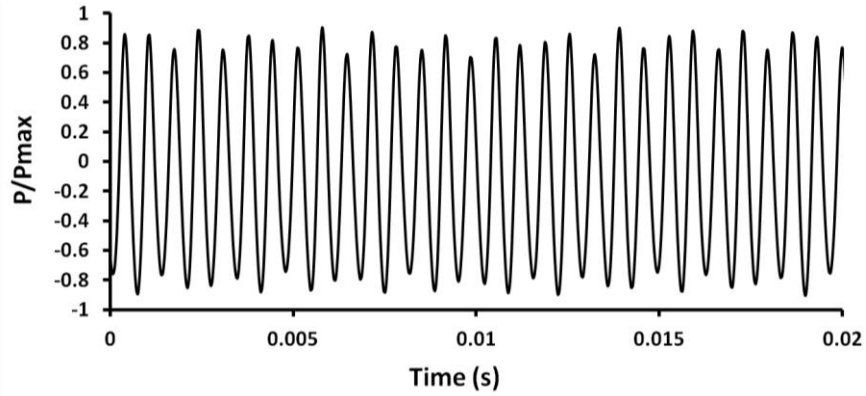

Figure 4-22: Instantaneous time signal of PT 2, depicting sinusoidal oscillations at *f*4=1480Hz

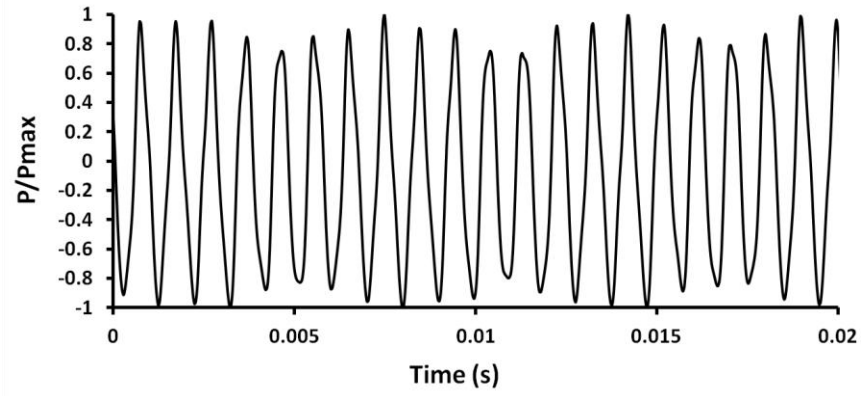

Figure 4-23: Instantaneous time signal of PT 3, depicting sinusoidal oscillations at *f3*=1033Hz

The two time signals in the previous figures are recorded simultaneously and are both normalized by the maximum recorded pressure from Figure 4-23. As illustrated from the spectra, the two pressure signals have comparable amplitudes and consist of a combination of the resonant frequencies and harmonics of the two excited modes as depicted by their complex and nonlinear signals. Nonetheless, the dominant sinusoidal component is the resonant frequency of the fourth mode for PT 2 and the third mode for PT3. The evidence of these pressure transducers recording different resonant frequencies at the same instant illustrates that these modes are not switching but rather excited concurrently. This behaviour suggests that the shear layer is able sustain the excitation of multiple modes simultaneously.

The normalized acoustic pressure and radial acoustic particle velocity distribution of the two simultaneously excited acoustic modes are shown in Figure 4-24. As discussed previously, the radial acoustic particle velocity distribution is broken down into separate circumferential sections at which the radial acoustic particle velocity fluctuations excite the shear layer oscillations. Comparing these two distributions shown in Figure 4-24, circumferential portions which are exposed to high acoustic particle velocity fluctuations by the third acoustic mode are exposed to significantly smaller radial velocity fluctuations from the fourth mode, and vice versa.

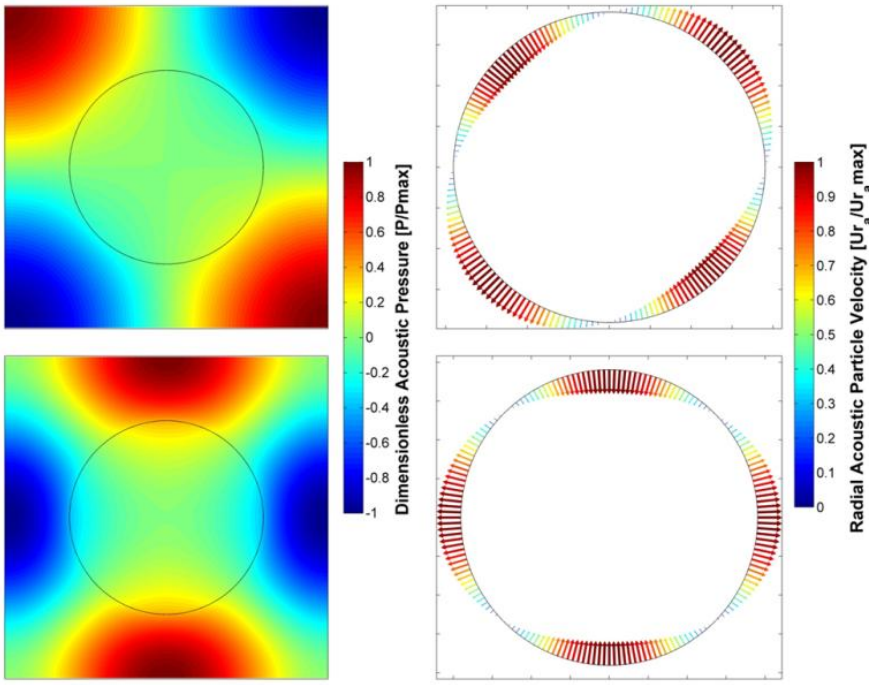

Figure 4-24: Dimensionless acoustic pressure and radial acoustic particle velocity distributions for the simultaneous excitation of the third and fourth acoustic mode

This dual excitation mechanism suggests that not only specific circumferential portions of the shear layer are oscillating, but separate portions are oscillating independently and at distinct resonant frequencies. This creates a very complex excitation mechanism, consisting of eight separate circumferential sections whose neighboring portions are oscillating at different frequencies. Those portions, whose locations correspond within the corner of the cavity, are oscillating independently at the resonant frequency of the third acoustic mode, f_3, and those within the side length correspond to oscillations at f_4.

To investigate the flow structures coexisting from the simultaneous dual excitation, PIV measurements were conducted using the same four measurement domains and pressure transducers from the preceding cases involving independent excitation. Due to the complexity of the acoustic signals, a band-pass Butterworth filter was utilized to extract each resonant frequency for phase averaging. Two sets of phase-averaged measurements, corresponding to each of the two

simultaneously excited modes, were conducted at a flow velocity of 91m/s where the pulsation amplitudes of the two modes were comparable. Figure 4-25 presents the average resolved vorticity fields due to phase-locking off the fourth mode's resonant frequency using PT2 located below. These measurements were conducted at four equal interval phase shifts, ϕ, separated by 90˚ along the fourth mode's resonant cycle at *f4*=1484Hz.

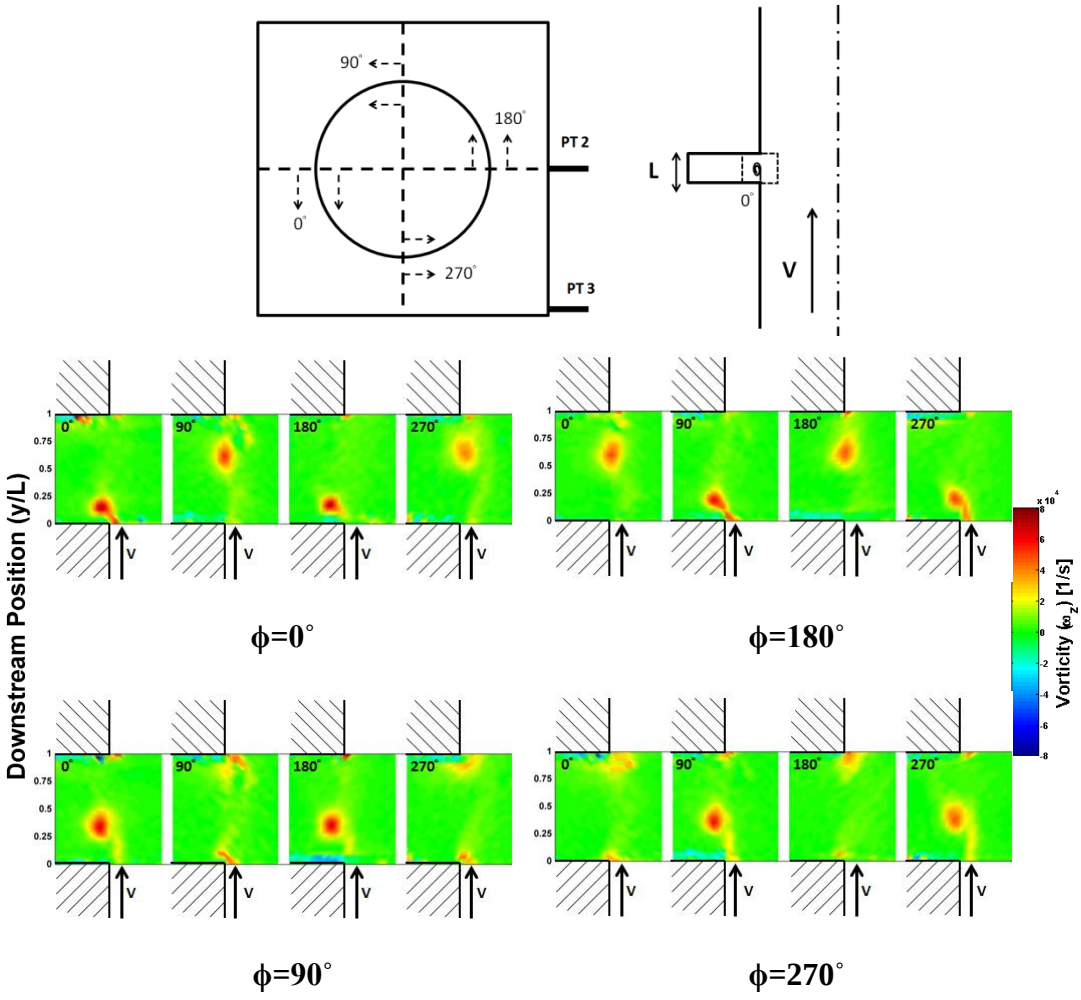

Figure 4-25: Phase-averaged vorticity fields during dual excitation corresponding to the fourth acoustic mode taken at four instants of the fourth mode acoustic cycle separated by 90˚ phase shifts, ϕ, *f4*=1484Hz, 91m/s

The phase-averaged vorticity fields of the fourth acoustic mode during the simultaneous excitation are consistent to the results from its independent excitation. The flow structure consists of two sets of parallel vortices 180˚ out of phase, analogous to its radial acoustic particle velocity distribution. Locations separated by a physical angle of 180˚ have the vortices in phase, and those projected domains that are orthogonal are completely out of phase. Through the phase-averaged vorticity fields, there is no evidence of vortices being shed from either the third acoustic mode or its first harmonic.

To investigate further, phase-averaging PIV was conducted through triggering of the third resonant frequency, *f3*=1033Hz, by the corner pressure transducer PT 3 located within the anti-node of the third acoustic mode. The measurements, Figure 4-26, are conducted at the same flow velocity, 91m/s, and the four projected domains are situated within the nodes of the third acoustic mode consisting of zero radial velocity fluctuations at this resonant frequency.

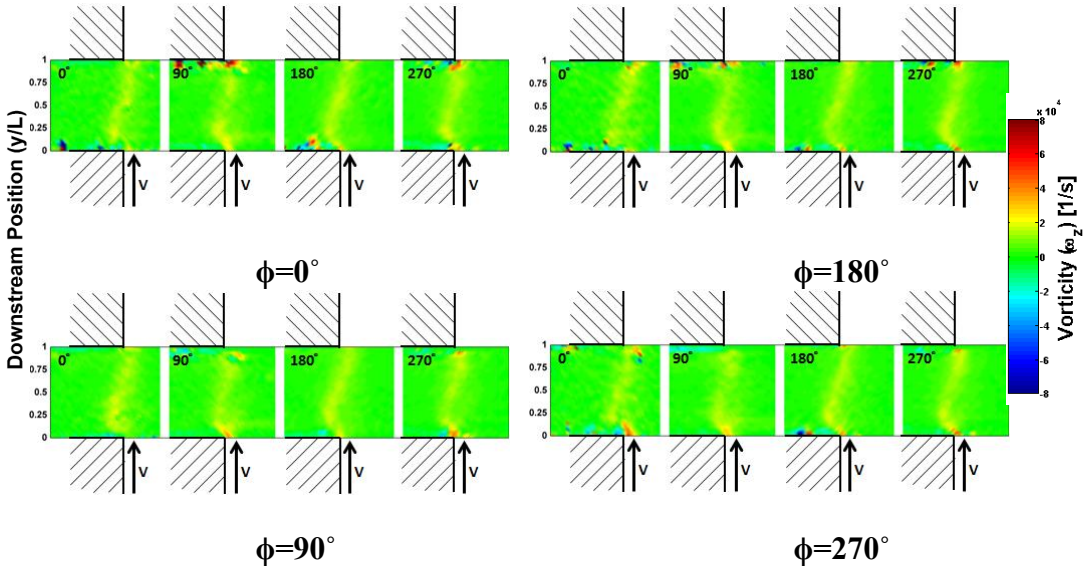

Figure 4-26: Phase-averaged vorticity fields during dual excitation corresponding to the third acoustic mode taken at four instants of the third mode acoustic cycle separate by 90˚ phase shifts, ϕ, *f3*=1033Hz, 91m/s

As shown in Figure 4-26, the vorticity fields are identical at each of the separate phase shifts. There are no coherent structures corresponding to the third resonant frequency or its harmonic. Despite the lack of vortices being present within the average vorticity field, each of the 250 instantaneous images consists of two sets of parallel vortices due to the simultaneous excitation of the fourth acoustic mode. One such instantaneous vorticity field is displayed in Figure 4-27. Once phase-averaged, shown in Figure 4-26, the phase-averaged vorticity field is smoothed out into the distributed paths which the fourth mode vortices are convected along the cavity length. This is due to the fact that the locations of the vortices differ in each of the 250 instantaneous images.

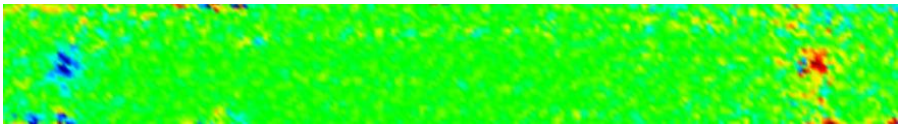

Figure 4-27: Instantaneous vorticity field through phase-triggering long the third mode's acoustic cycle illustrating a pair of vortices from the simultaneous excitation of the fourth mode

In these two sets of measurements, the four projected domains coincide to the large velocity fluctuations of the fourth mode and the nodal lines of the third. The formation of vortices occurred predominantly at the fourth mode's resonant frequency consistent to the results of its independent excitation. The simultaneous excitation of the third acoustic mode, however, had no effect on the initiation of disturbances, despite it having comparable pulsation amplitudes. If measurements were conducted within the corners of the cavity, coinciding to the maximum fluctuations of the third acoustic mode and the nodal lines of the fourth, the opposite behaviour would be expected. The four circumferential shear layer sections at the cavity corners would initiate vortices at the third mode's resonant frequency with negligible influence from the simultaneous excitation of the fourth mode.

These results verify that the independence of the circumferential portions along the shear layer circumference allow the simultaneous excitation of multiple

diametral acoustic modes. The non-uniform excitation not only allows specific circumferential portions to be excited, but neighbouring portions may oscillate independently and initiate vortices at separate resonant frequencies concurrently. These portions coincide to regions of significant radial velocity fluctuations akin to its acoustic mode shape. Despite this convoluted radial acoustic particle velocity distribution, the flow structures along the shear layer are coherent allowing the strong excitation of both acoustic modes simultaneously.

In the cases of the rectangular cavities, $W/H \neq 1$, the first and second acoustic modes were only excited independently and at separate flow velocities despite the dimensions varying slightly off unity, W/H=0.9-0.95, and having similar natural frequencies and onset resonance velocities. An explanation of this behaviour may be observed through comparisons of their radial acoustic particle velocity distributions along the circumference of the upstream cavity corner. These distributions of the W/H=0.9 cavity are displayed in Figure 4-28.

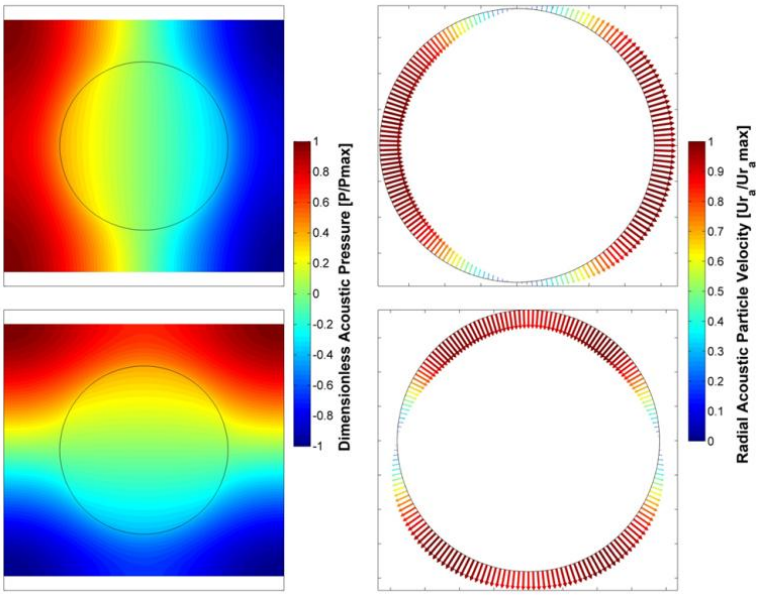

Figure 4-28: Acoustic mode shapes and radial particle velocity distributions of the first two acoustic modes, W/H=0.9 cavity

Unlike the previous case involving excitation of the third and the fourth acoustic modes, the regions of the maximum radial acoustic particle velocity are

not located within the nodes of the other excited acoustic mode. Instead, both acoustic modes have strong radial velocity fluctuations at the corners of the cavity. These fluctuations are expected to force the shear layer to oscillate at two separate frequencies. This may suppress any coherent oscillations of the shear layer. The preferential excitation of one mode over another may be due to acoustic energy being more trapped for the first acoustic mode than the second. This is because the energy is situated at larger radial distances from the attached piping.

4.4.3 Simultaneous Excitation of Two Degenerate Modes

The presence of asymmetry inherent within the rectangular cavities ensured that there is one unique modal shape for each trapped acoustic mode and its resonant frequency. This led to a stationary behaviour where the anti-nodes and nodal lines would remain fixed and situated to those locations resolved from the numerical simulations. With the introduction of symmetry, such as an axisymmetric or square cavity, the preferential orientation of the acoustic mode is now removed leading to multiple potential mode shapes that can only be satisfied through a spinning behaviour.

This is specifically observed during the excitation of the two degenerate modes within the square cavity. Due to the cavity cross-sectional dimensions being equivalent, two orthogonal mode shapes were resolved for the same resonant frequency. Hence the excitation of this acoustic mode shape did not have a preferred orientation and the acoustic mode tended to spin with the acoustic cycle representing one full rotation. Evidence of this spinning behaviour is shown in the four instantaneous acoustic pressure signals during its excitation, Figure 4-29. These time signals were recorded at a mean flow velocity of 63m/s and normalized by the maximum measured amplitude located within the corners. The field of view and the locations of the installed pressure transducers are labelled.

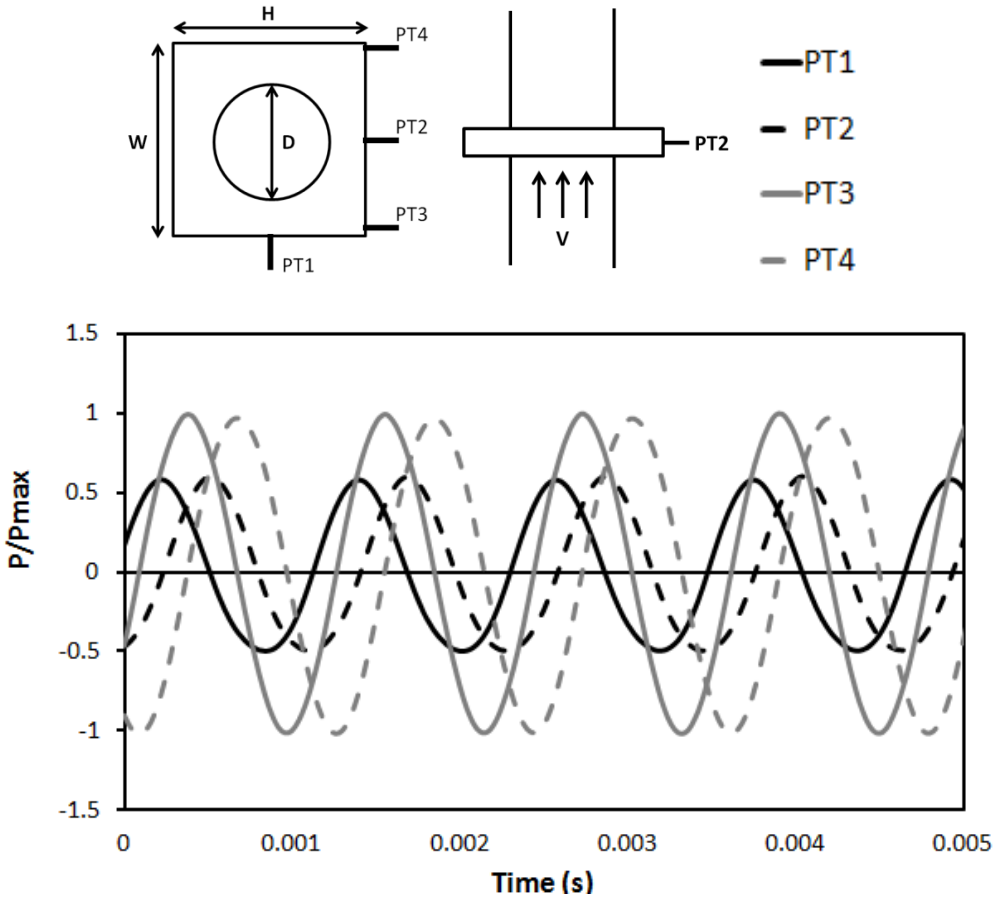

Figure 4-29: Instantaneous time signal illustrating the spinning behaviour of the degenerate mode for the square cavity, 63m/s

The spinning behaviour is confirmed through the relative phase angles of the acoustic pressure signals being equivalent to the physical enclosed angle of the measuring pressure transducers. For example, the pressure signals of the first and third transducers are 45˚ out of phase, equal to its separation angle, and those of the first and second are 90˚ out of phase, which is similar to the physical angle between the transducers. This is consistent to the definition of a fully spinning mode rotating in the counter-clockwise direction. However, the acoustic pressure amplitude is maximum within the corners of the cavity where the acoustic energy is trapped and localized further away from the pipe centerline. This is indicated by the larger recorded pressure amplitudes measured from PT3 and PT4.

At large pressure amplitudes associated with higher flow velocities, the direction of spin for the acoustic mode remained fairly stabilized in the counter-clockwise orientation as displayed in Figure 4-29. However, at lower flow velocities and pulsation amplitudes the direction of spin became intermittent and would vary randomly. For example, at 50m/s the mode was observed to be spinning counter-clockwise for 20s then switched to the clockwise direction for 8s.

To illustrate the modal shape and radial acoustic particle velocity distribution throughout the spinning mode's acoustic cycle, the two orthogonal mode model previously applied by Aly (2008) and Selle et al. (2006) was utilized. This model represents the spinning behaviour through super positioning two equal amplitude orthogonal stationary modes with a 90˚ temporal phase shift. The two orthogonal modes were the first and second trapped acoustic modes shown in Figure 4-30. The associated acoustic pressure and radial acoustic particle velocity distributions are normalized by the maximum magnitude along one whole cycle of the resultant spinning mode. Once again, emphasis is placed at the upstream cavity corner where the development of the vortical disturbances is initiated in the shear layer by the radial acoustic particle velocity distribution.

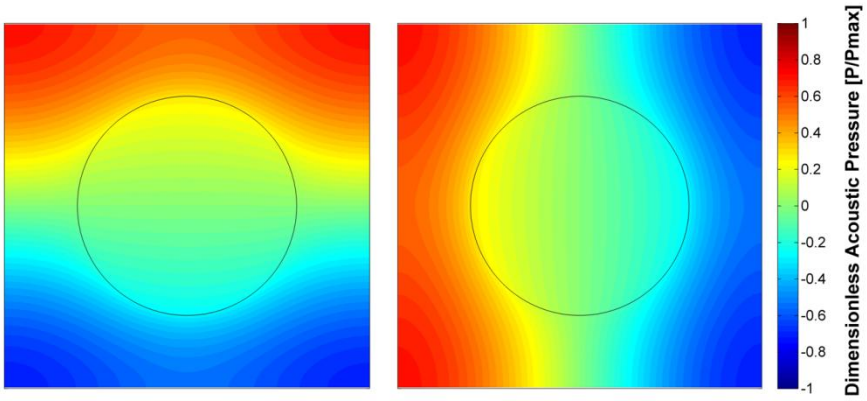

Figure 4-30: Super positioned orthogonal modes normalized by largest amplitude within the acoustic cycle of the resultant spinning mode

Eight frames of the acoustic pressure at 22.5˚ equal intervals of the phase, θ, are resolved in Figure 4-31. As displayed, the acoustic mode spins at its resonant frequency of 851Hz, completing one full rotation throughout an acoustic cycle. The initial position corresponds to the first orthogonal mode and the phase represents the physical angle measured in the counter-clockwise direction from the origin. Similar to the instantaneous time signals, the maximum acoustic pressure occurs when the nodal line is located within the corner of the cavity.

The upstream radial acoustic particle velocity distributions for each of the eight frames are presented in Figure 4-32. The acoustic particle velocity leads the acoustic pressure by 90˚ as indicated through comparisons of their distributions. As clearly shown, the radial acoustic particle velocity distribution is non-uniform and asymmetric about its nodal line. This suggests, once again, that only specific circumferential portions of the shear layer are being excited by the radial acoustic particle velocity fluctuations. However, due to the spinning behaviour, these excited circumferential sections are now varying spatially throughout its acoustic cycle. This unique excitation mechanism, now being a function of space and time, leads to a similarly complex three-dimensional flow field of propagating disturbances.

To investigate the flow structures associated with the spinning mode, qualitative two-dimensional phase-averaged PIV was conducted at the projected domains shown in Figure 4-33. The acoustic mode preferred to spin in the counter-clockwise direction; however, some switching did occur. Therefore a conservative 300 instantaneous flow-fields were measured at each phase to ensure a sufficiently averaged flow field with only those flow fields corresponding to the counter-clockwise direction were averaged. The phase-averaged vorticity fields, separated by a phase of 45˚, are presented in Figure 4-34. Measurements were conducted at a mean flow velocity of 59m/s and a resonant frequency of 851Hz.

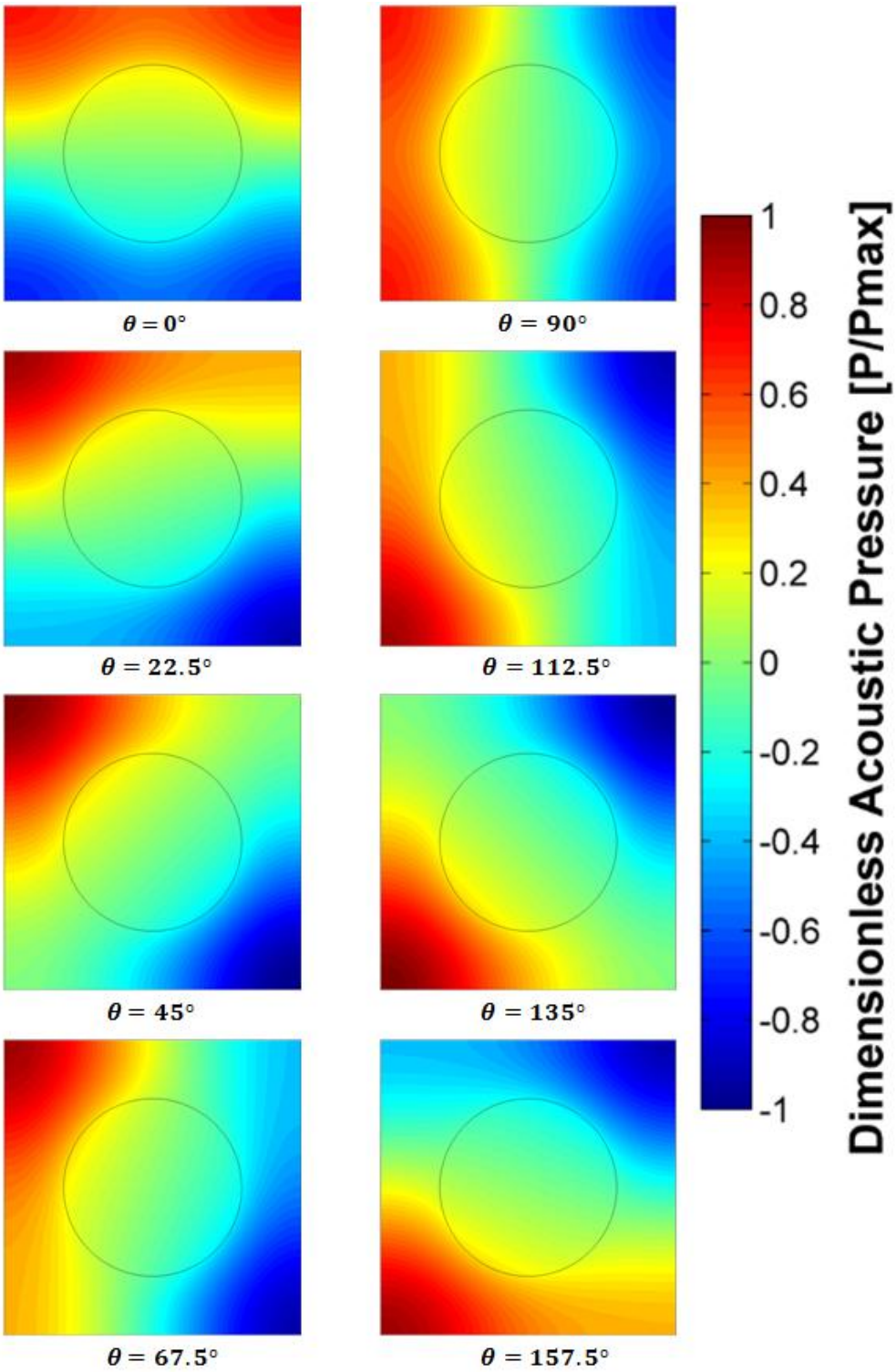

Figure 4-31: Instantaneous normalized acoustic pressure contours of spinning degenerate mode at phase, θ.

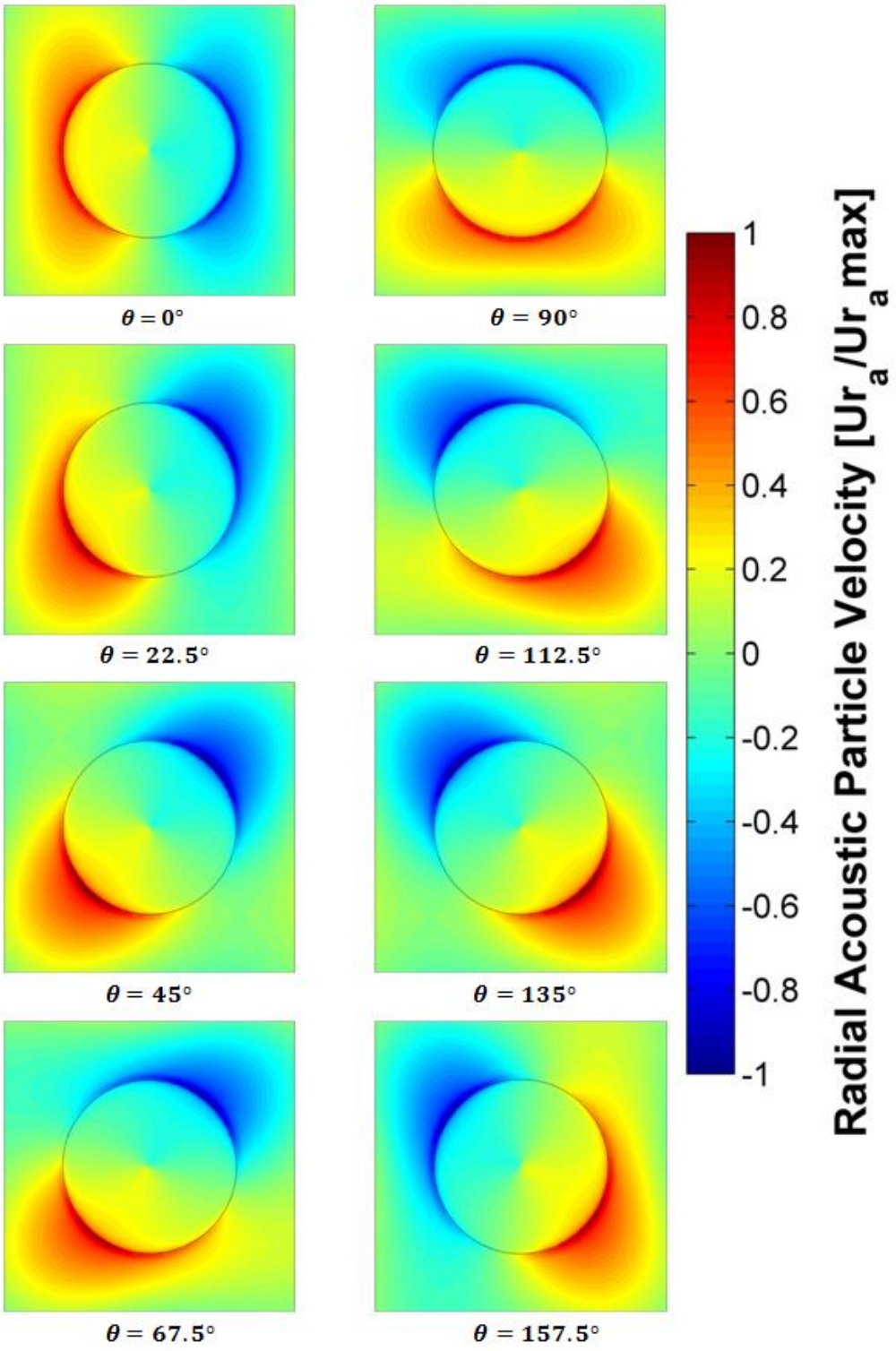

Figure 4-32: Instantaneous normalized radial acoustic particle velocity contours of spinning degenerate mode at phase, θ.

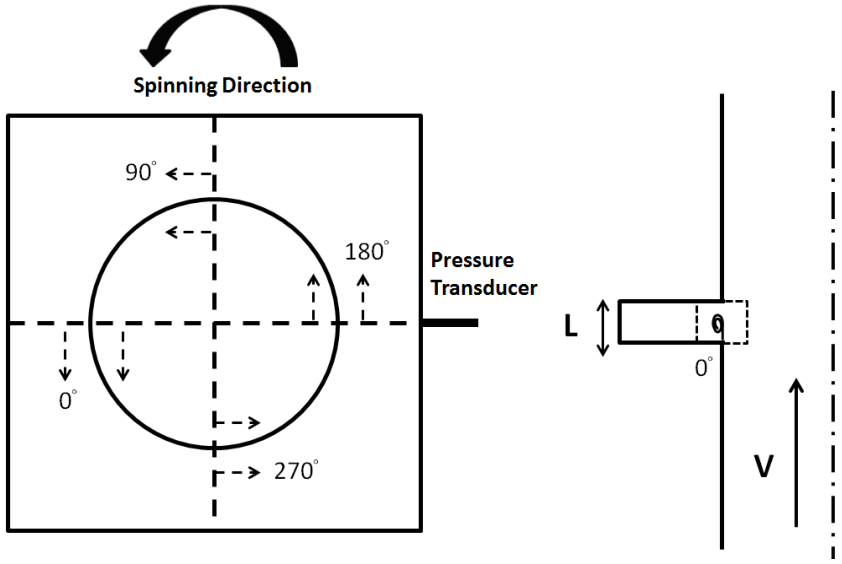

Figure 4-33: Projected measurement domains and spinning direction for the degenerate acoustic mode

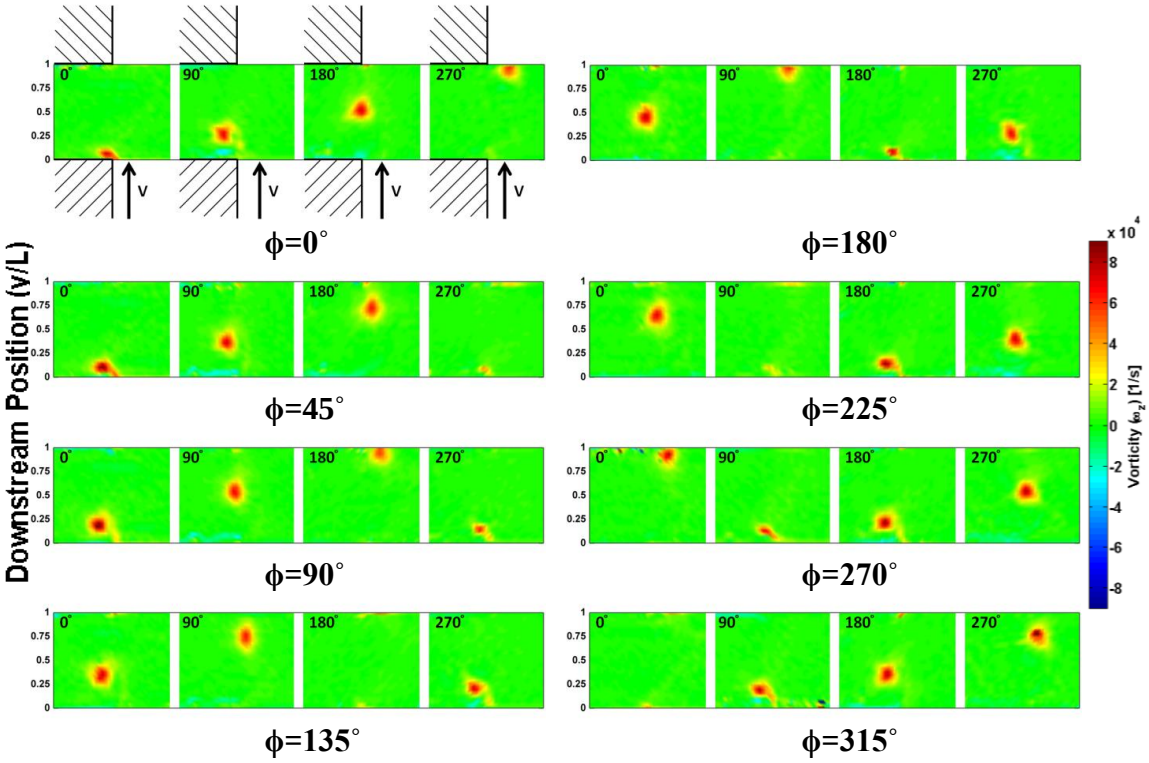

Figure 4-34: Flow visualization of phase-averaged vorticity fields displaying the helical propagation of disturbances along the four measurement domains at separate phase angles, ϕ, of the spinning degenerate mode, 59m/s, 851Hz. Note: The phase angles of the images do not correspond to the same phase, θ, from the previous Figures.

Through comparison of each of the phase-averaged vorticity fields, the downstream positions of the propagating disturbances are out of phase by the angle separating their projected measurement domains. The effect of the spinning of the acoustic mode on the flow structure is most apparent through observations of the $\phi = 0^{\circ}$ vorticity field in which the four vortices form a diagonal line in sequence of their measurement angle.

This behaviour is consistent to the counter-clockwise rotation of the acoustic mode and its radial acoustic particle velocity distribution. The excited circumferential sections are now varying spatially and so too is the initiation of the vortical structures. As displayed in Figure 4-32, the development of disturbances occurs all along the circumference of the shear layer near the upstream corner and not just at these four specific measurement locations. Thus, this vortical structure is of the *helical type*, similar, but spinning in opposite direction, to the smoke flow visualization illustrated in Figure 4-35 (right) taken from the excitation of a free round jet. The helix consists of one cycle of revolution along the cavity length and completes a revolution around the shear layer circumference every acoustic cycle. The helical nature is due to a combination of the spinning acoustic mode and the convective mean flow velocity.

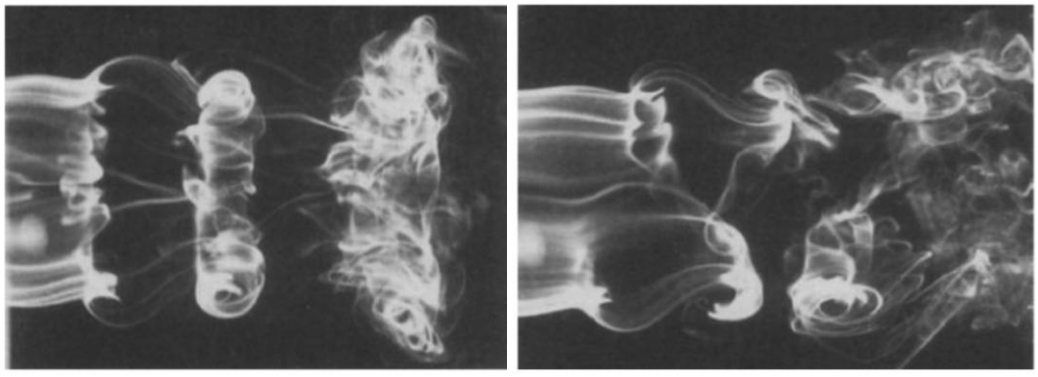

Figure 4-35: Smoke flow visualization of a torodial vortex (left) and helical vortex (right) from the external excitation of a free round jet (Kusek et al., 1990)

This structure is consistent with the numerical simulations conducted by Selle et al. (2006), and is significantly different from the torodial structures from the uniform excitation of longitudinal modes, Figure 4-35 (left).

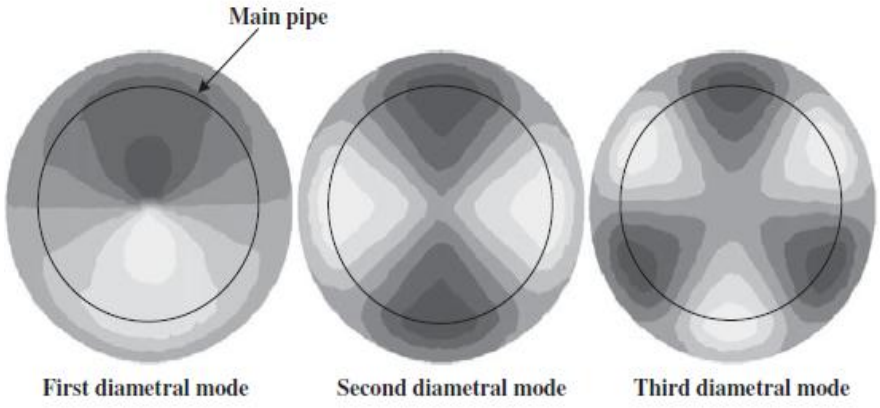

Figure 4-36: Radial acoustic particle velocity distribution of the diametral modes within an axisymmetric cavity with h=25.4mm, L/h=1 (Aly & Ziada, 2010)

A similar behaviour is expected from the spinning diametral modes within axisymmetric cavities. The radial acoustic particle velocity distributions for the first three diametral modes are illustrated in Figure 4-36 (Aly & Ziada, 2010). As shown, the first diametral mode is similar to the spinning acoustic mode within the square cavity, consisting of one nodal line. As the number of nodal lines increase, so does the number of circumferential sections that are strongly excited by the radial acoustic particle velocity fluctuations. The amount of nodal lines would be equivalent to the number of parallel helices propagating downstream by the mean flow velocity. Hence, the second diametral mode would consist of two parallel helical structures, and the third diametral mode would consist of three.

CHAPTER 5
CONCLUSIONS

5.1 Summary

The excitation of trapped diametral acoustic modes within rectangular cavities was investigated experimentally and numerically. Resonance of the first four trapped acoustic modes dominated the aeroacoustic responses of each of the three cavity geometries. Numerical simulations indicated that as the cavity became smaller, and more asymmetric, the trapped nature of two of the acoustic modes decreased. This behaviour was evident within the experimental results, where the pulsation amplitudes of the fourth acoustic mode decreased substantially with a reduction in the cavity width, *W*.

The resolved acoustic mode shapes were asymmetric, corresponding to a non-uniform radial acoustic particle velocity distribution. This is quite different compared to the uniform excitation of longitudinal acoustic modes and its resultant vortex ring structure. However, the associated diametral modes were excited strongly, indicating that a uniform excitation of the shear layer is not necessary for sustainment of strong acoustic resonance. Throughout the experimental results, three distinct modal behaviours were observed.

The most frequent behaviour was the independent excitation of a single stationary mode. Results illustrated that specific circumferential portions of the shear layer were being excited by the non-uniform acoustic particle velocity distribution, which is generated by the acoustic mode shape. The distribution of propagating disturbances was consistent and akin to the associated radial acoustic particle velocity distribution. Shear layer portions that had the radial particle velocity in phase generated propagating disturbances situated at the same downstream position throughout its acoustic cycle. Those portions that were out of phase had the downstream position of their vortices being separated by 180˚, as

illustrated from comparing their phase-averaged vorticity fields. Measurements conducted along the nodal lines, coinciding with zero radial acoustic particle velocity, observed the presence of weak vortical structures being propagated at the first harmonic frequency of the excited mode.

As well, evidence verified that the shear layer was able to excite two acoustic modes with different resonant frequencies simultaneously. The circumferential portions which are exposed to high acoustic particle velocity fluctuations by one acoustic mode were exposed to significantly smaller velocity fluctuations from the other, and vice versa. Thus, neighbouring portions of the shear layer were oscillating at different frequencies and amplitudes. Phase-averaged vorticity fields detailed that these neighbouring sections were highly independent from one another. The propagation of vortical structures within the anti-node was consistent with the previous independent excitation case, with the simultaneous excitation of the one acoustic mode having no direct influence on the other's development of vortical structures.

In the case of the symmetric square cavity, two resolved orthogonal mode shapes consisted of the same resonant frequency. This degenerate acoustic mode had no preferred orientation, leading to a spinning behaviour. Similar to the previous cases, the asymmetry of the diametral mode allowed only specific circumferential portions of the shear layer to be excited by the radial acoustic particle velocity. However, due to the spinning nature, these circumferential portions are spatially spinning 90° out of phase with the acoustic pressure. This led to the formation of a helical vortical structure, spinning about the shear layer circumference once every acoustic cycle.

5.2 Suggestions for Future Work

From the results of the current study, recommendations are presented for future passive suppression techniques. In previous studies, spoilers situated at the upstream cavity corner successfully eliminated the acoustic resonance of excited trapped diametral modes in axisymmetric cavities (Bolduc et al., 2014). However, these modifications introduced a significant amount of pressure drop which is highly undesirable in the application of isolation gate valves. Since the diametral modes were spinning within the axisymmetric cavity, the spoilers were installed all along the circumference of the upstream cavity corner.

In the case of gate valves/rectangular cavities the diametral acoustic modes are stationary and asymmetric. Only specific circumferential portions of the shear layer that coincide with large acoustic particle velocity fluctuations are being excited. Thus, spoilers would only need to be present along those shear layer sections to eliminate the acoustic resonance. This would reduce the pressure drop significantly in comparison to the installation along the whole shear layer circumference.

As well, varying the number of circumferential portions that consist of spoilers and observing the effects on the overall strength of excitation of the acoustic mode and corresponding increase in pressure drop should prove beneficial. If a sufficient reduction in acoustic pressure is achieved without placing the spoilers in all the circumferential sections, then additional spoilers are not necessary and pressure drop would be reduced. Nonetheless, the characteristics of the acoustic mode shape and its acoustic particle velocity distribution would need to be known in order to position these modifications effectively.

REFERENCES

Aly, K. M. A. (2008). Aerodynamic excitation of the diametral modes of an internal axisymmetric cavity (Doctoral dissertation). Hamilton, Ontario, Canada: McMaster University.

Aly, K., & Ziada, S. (2010). Flow-excited resonance of trapped modes of ducted shallow cavities. Journal of Fluids and Structures, 26(1), 92-120.

Aly, K., & Ziada, S. (2011). Azimuthal behaviour of flow-excited diametral modes of internal shallow cavities. Journal of Sound and Vibration, 330(15), 3666-3683.

Aly, K., & Ziada, S. (2012). Effect of mean flow on the trapped modes of internal cavities. Journal of Fluids and Structures, 33, 70-84.

Barannyk, O., & Oshkai, P. (2014). Investigation of diametral acoustic modes in a model of a steam control gate valve. Journal of Pressure Vessel Technology, 136(6), 061302.

Betts, P. L. (1972). Self-induced oscillations in an open water-channel with slotted walls. Journal of Fluid Mechanics, 55(03), 401-417.

Bolduc, M., Elsayed, M., & Ziada, S. (2014). Passive Control of Trapped Mode Resonance of Ducted Cavities. Journal of Pressure Vessel Technology, 136(5), 051311.

Bruggeman, J. C., Hirschberg, A., Van Dongen, M. E. H., Wijnands, A. P. J., & Gorter, J. (1991). Self-sustained aero-acoustic pulsations in gas transport systems: experimental study of the influence of closed side branches. Journal of Sound and Vibration, 150(3), 371-393.

Cattafesta, L., Williams, D., Rowley, C., & Alvi, F. (2003). Review of active control of flow-induced cavity resonance. AIAA paper, 3567, 2003.

Chevray R. (1984). Entrainment in turbulent flows: mechanisms and implications North-Holland: Elsevier Science Publishers B.V., 365-369.

Duan, Y., Koch, W., Linton, C. M., & McIver, M. (2007). Complex resonances and trapped modes in ducted domains. Journal of Fluid Mechanics, 571, 119-147.

Durst, F. (1976). Principles and practice of laser-doppler aneometry. Academic Press Inc.

Evans, D. V., & Linton, C. M. (1991). Trapped modes in open channels. Journal of Fluid Mechanics, 225, 153-175.

Evans, D. V., Levitin, M., & Vassiliev, D. (1994). Existence theorems for trapped modes. Journal of Fluid Mechanics, 261, 21-31.

Freymuth, P. (1966). On transition in a separated laminar boundary layer. Journal of Fluid Mechanics, 25(04), 683-704.

Hein, S., & Koch, W. (2008). Acoustic resonances and trapped modes in pipes and tunnels. Journal of Fluid Mechanics, 605, 401-428.

Heller, H. H., & Bliss, D. B. (1975). The physical mechanism of flow-induced pressure fluctuations in cavities and concepts for their suppression. AIAA paper, 491, 1975.

Ho, C. M., & Huang, L. S. (1982). Subharmonics and vortex merging in mixing layers. Journal of Fluid Mechanics, 119, 443-473.

Hourigan, K., Welsh, M. C., Thompson, M. C., & Stokes, A. N. (1990). Aerodynamic sources of acoustic resonance in a duct with baffles. Journal of Fluids and Structures, 4(4), 345-370.

Howe, M. S. (1980). The dissipation of sound at an edge. Journal of Sound and Vibration, 70(3), 407-411.

Huang, X. Y., & Weaver, D. S. (1991). On the active control of shear layer oscillations across a cavity in the presence of pipeline acoustic resonance. Journal of Fluids and Structures, 5(2), 207-219.

Karadogan, H., & Rockwell, D. (1983). Toward attenuation of self-sustained oscillations of a turbulent jet through a cavity. Journal of fluids engineering, 105(3), 335-340.

Keller, J. J., & Escudier, M. P. (1983). Flow-excited resonances in covered cavities. Journal of Sound and Vibration, 86(2), 199-226.

Kinsler, L.E., Frey, A.R., Coppens, A.B. & Sanders, J.V. (2000). Fundamentals of Acoustics. New York: John Wiley & Sons, Inc.

Kline, S. J., & McClintock, F. A. (1953). Describing uncertainties in single-sample experiments. *Mechanical engineering*, *75*(1), 3-8.

Knotts, B. D., & Selamet, A. (2003). Suppression of flow–acoustic coupling in sidebranch ducts by interface modification. Journal of Sound and Vibration, *265*(5), 1025-1045.

Kusek, S. M., Corke, T. C., & Reisenthel, P. (1990). Seeding of helical modes in the initial region of an axisymmetric jet. Experiments in Fluids, 10(2-3), 116-124.

Lacombe, R., Lafon, P., Daude, F., Crouzet, F., Bailly, C., & Ziada, S. (2013). Numerical and experimental analysis of flow-acoustic interactions in an industrial gate valve. 19th AIAA/CEAS Aeroacoustics Conference, May27-29, 2013 Berlin, Germany.

Lafon, P., Caillaud, S., Devos, J. P., & Lambert, C. (2003). Aeroacoustical coupling in a ducted shallow cavity and fluid/structure effects on a steam line. Journal of Fluids and structures, 18(6), 695-713.

Michalke, A. (1964). On the inviscid instability of the hyperbolic tangent velocity profile. Journal of Fluid Mechanics, 19(04), 543-556.

Michalke, A. (1965). On spatially growing disturbances in an inviscid shear layer. Journal of Fluid Mechanics, 23(03), 521-544.

Miksad, R. W. (1972). Experiments on the nonlinear stages of free-shear-layer transition. Journal of Fluid Mechanics, 56(04), 695-719.

Mohamed, S., & Ziada, S. (2014, July). PIV Measurements of Aeroacoustic Sources of a Shallow Cavity in a Pipeline. In ASME 2014 Pressure Vessels and Piping Conference. American Society of Mechanical Engineers.

Morse, P. (1948). Vibration and Sound, McGraw-Hill Book Company Inc.

Nakiboğlu, G., & Hirschberg, A. (2010, January). A numerical study of the aeroacoustic interaction of a cavity with a confined flow: effect of edge geometry in corrugated pipes. In ASME 2010 3rd Joint US-European Fluids Engineering Summer Meeting collocated with 8th International Conference on Nanochannels, Microchannels, and Minichannels (pp. 767-773). American Society of Mechanical Engineers.

NRC. (2002). Failure of Steam Dryer Cover Plate after a Recent Power Uprate. NRC Information Notice 2002-26. US Nuclear Regulatory Commission, Washington, D.C.

O'Connor, J., Acharya, V., & Lieuwen, T. (2015). Transverse combustion instabilities: Acoustic, fluid mechanic, and flame processes. Progress in Energy and Combustion Science, 49, 1-39.

Rayleigh, L., (1880). On the instability or instability of certain fluid motions. Proc. London Math. Soc, 11, 57-70.

Rockwell, D. (1983). Oscillations of impinging shear layers. AIAA journal, 21(5), 645-664.

Rockwell, D., & Naudascher, E. (1978). Review—self-sustaining oscillations of flow past cavities. Journal of Fluids Engineering, 100(2), 152-165.

Rockwell, D., & Schachenmann, A. (1982). The organized shear layer due to oscillations of a turbulent jet through an axisymmetric cavity. Journal of Sound and Vibration, 85(3), 371-382.

Rossiter, J. E. (1964). Wind tunnel experiments on the flow over rectangular cavities at subsonic and transonic speeds. Ministry of Aviation; Royal Aircraft Establishment; RAE Farnborough.

Selle, L., Lartigue, G., Poinsot, T., Koch, R., Schildmacher, K. U., Krebs, W., Prade, B., Kaufmann, P., & Veynante, D. (2004). Compressible large eddy simulation of turbulent combustion in complex geometry on unstructured meshes. Combustion and Flame, 137(4), 489-505.

Selle, L., Benoit, L., Poinsot, T., Nicoud, F., & Krebs, W. (2006). Joint use of compressible large-eddy simulation and Helmholtz solvers for the analysis of rotating modes in an industrial swirled burner. Combustion and Flame, 145(1), 194-205.

Smith, B. A., & Luloff, B. V. (2000). The effect of seat geometry on gate valve noise. Journal of pressure vessel technology, 122(4), 401-407.

Tam, C. K., & Block, P. J. (1978). On the tones and pressure oscillations induced by flow over rectangular cavities. Journal of Fluid Mechanics, 89(02), 373-399.

Tam, C. K. (1976). The acoustic modes of a two-dimensional rectangular cavity. Journal of Sound and Vibration, 49(3), 353-364.

Tollmien, W. (1935). A General Criterion for the Instability of Laminar Velocity Distributions

Tyler, J. M., & Sofrin, T. G. (1962). Axial flow compressor noise studies (No. 620532). SAE Technical Paper.

Worth, N. A , & Dawson, J. R.(2015). The effect of baffles on self-excited azimuthal modes in an annular combustor. Proceedings of the Combustion Institute, 35(3), 3283-3290.

Worth, N. A., & Dawson, J. R. (2013). Modal dynamics of self-excited azimuthal instabilities in an annular combustion chamber. Combustion and Flame, 160(11), 2476-2489.

Ziada, S. (2010). Flow-excited acoustic resonance in industry. Journal of Pressure Vessel Technology, 132(1), 015001.

Ziada, S., Bühlmann, E. T., & Bolleter, U. (1989). Flow impingement as an excitation source in control valves. Journal of Fluids and Structures, 3(5), 529-549.

Ziada, S., Ng, H., & Blake, C. E. (2003). Flow excited resonance of a confined shallow cavity in low Mach number flow and its control. Journal of fluids and structures, 18(1), 79-92.

APPENDIX A
ADDITIONAL RESULTS

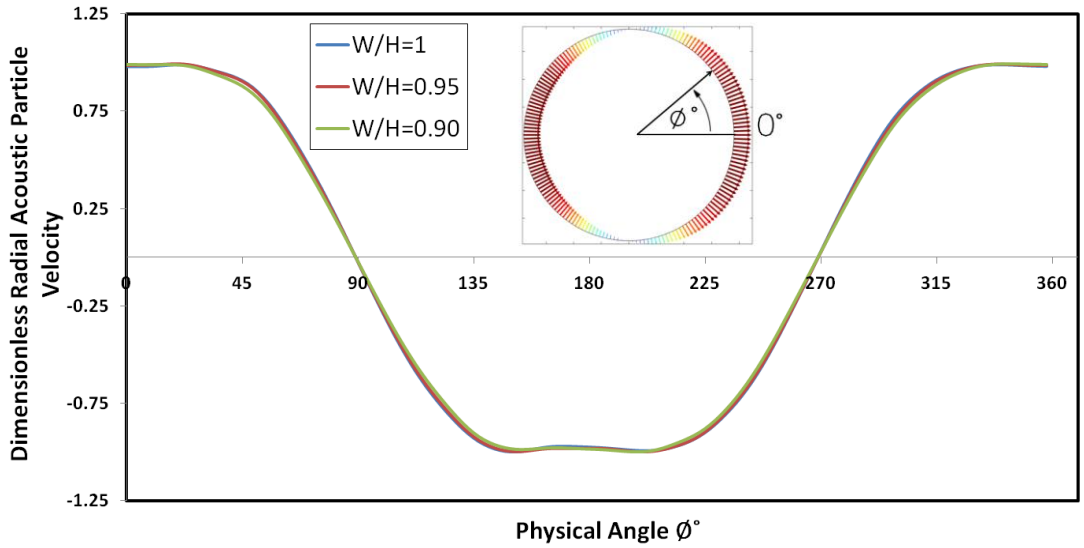

Figure A-1: Comparison of dimensionless radial particle velocity distribution for the first acoustic mode as a function of angle, Ø, upstream cavity corner of the three cavity geometries

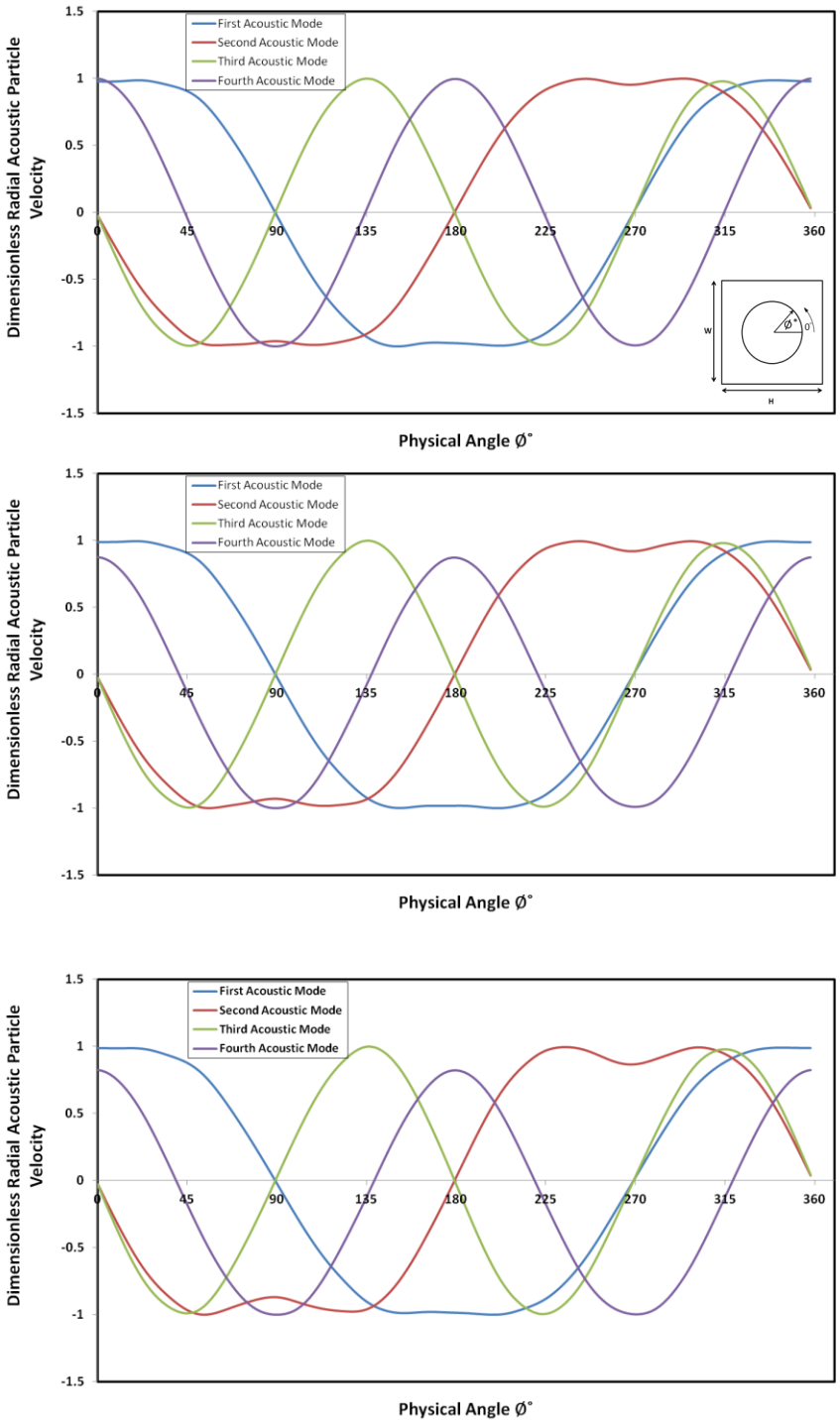

Figure A-2: Dimensionless Acoustic Particle velocity distributions of the four acoustic modes for the Top: *W/H*=1, Middle: W/H=0.95, Bottom: W/H=0.9, cavities

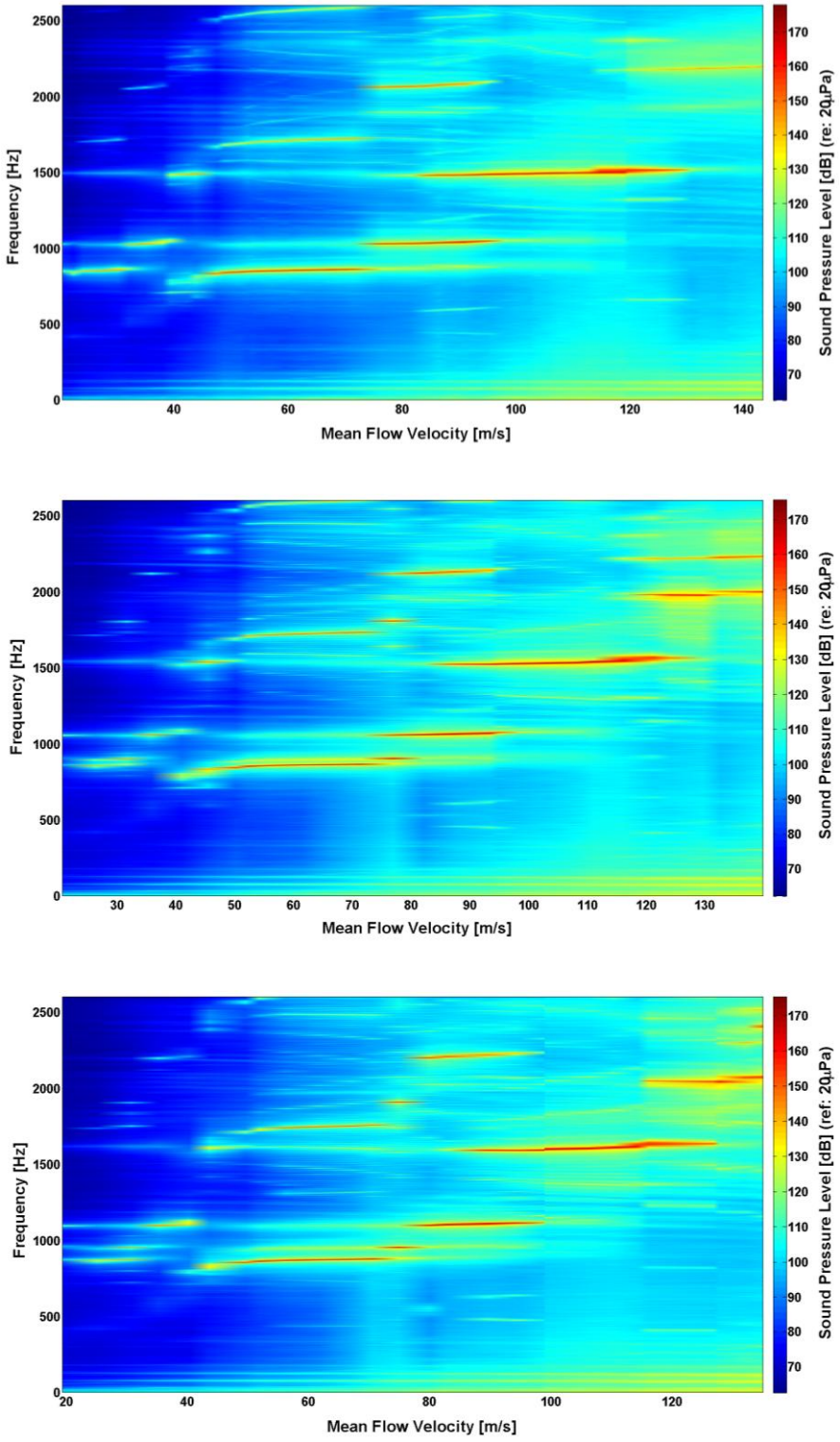

Figure A-3: SPL contour plot of the aeroacoustic response for the Top=*W/H*=1, Middle=W/H=0.95, Bottom=W/H=0.9 cavities

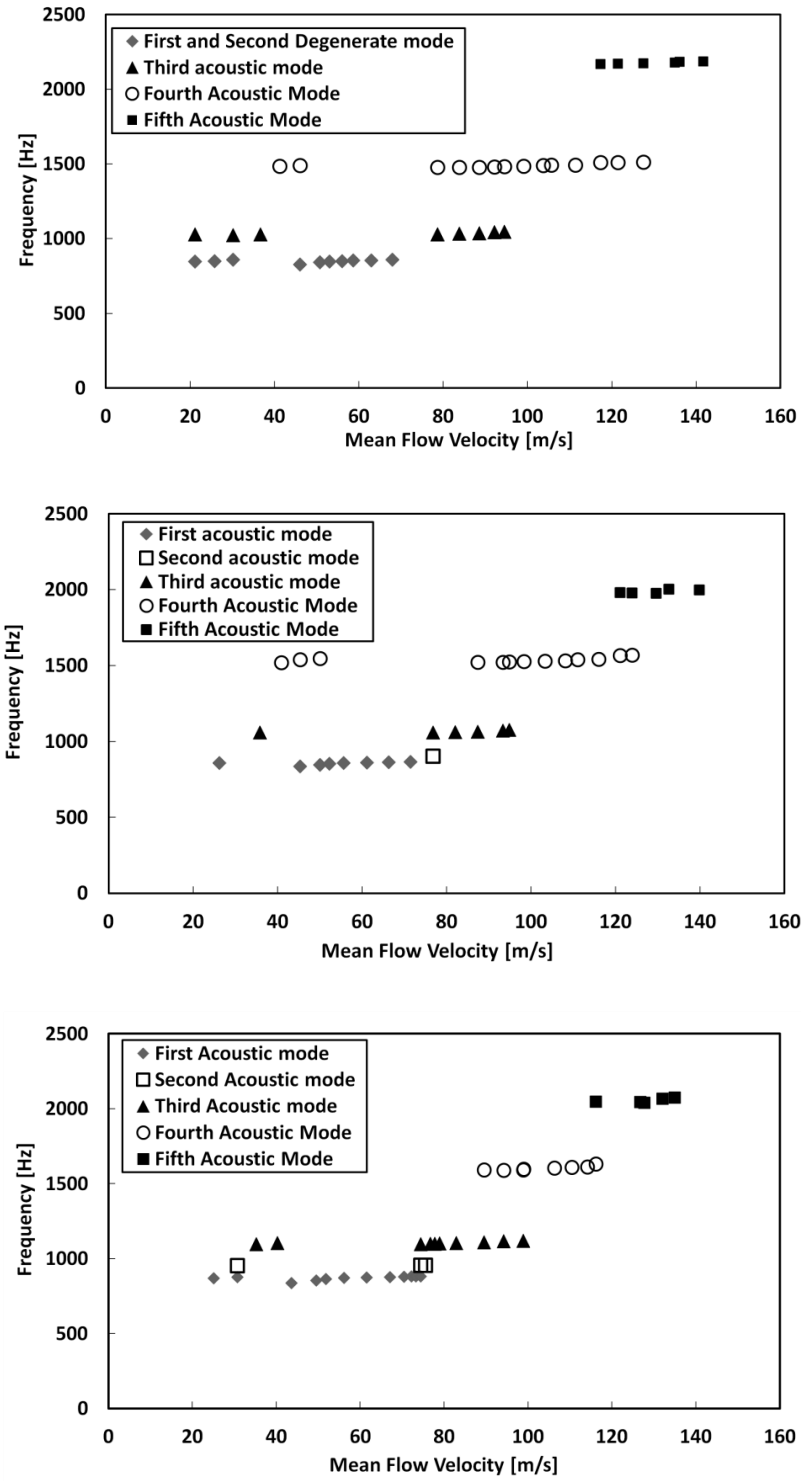

Figure A-4: Frequency [Hz] vs. Mean Flow Velocity [m/s] Top=*W/H*=1, Middle=W/H=0.95, Bottom=W/H=0.9 cavities

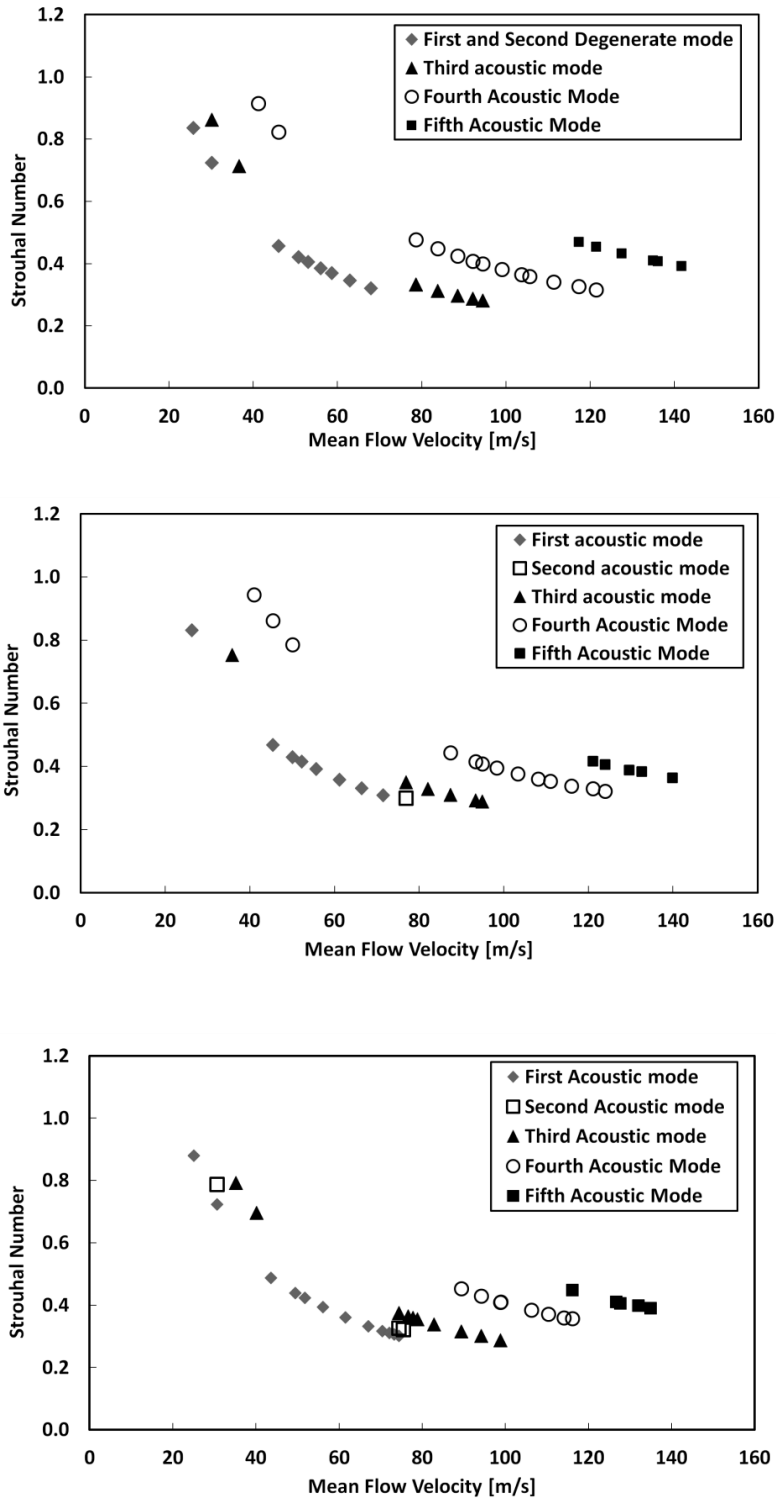

Figure A-5: Strouhal Number vs. Mean Flow Velocity [m/s] Top=*W/H*=1, Middle=W/H=0.95, Bottom=W/H=0.9 cavities

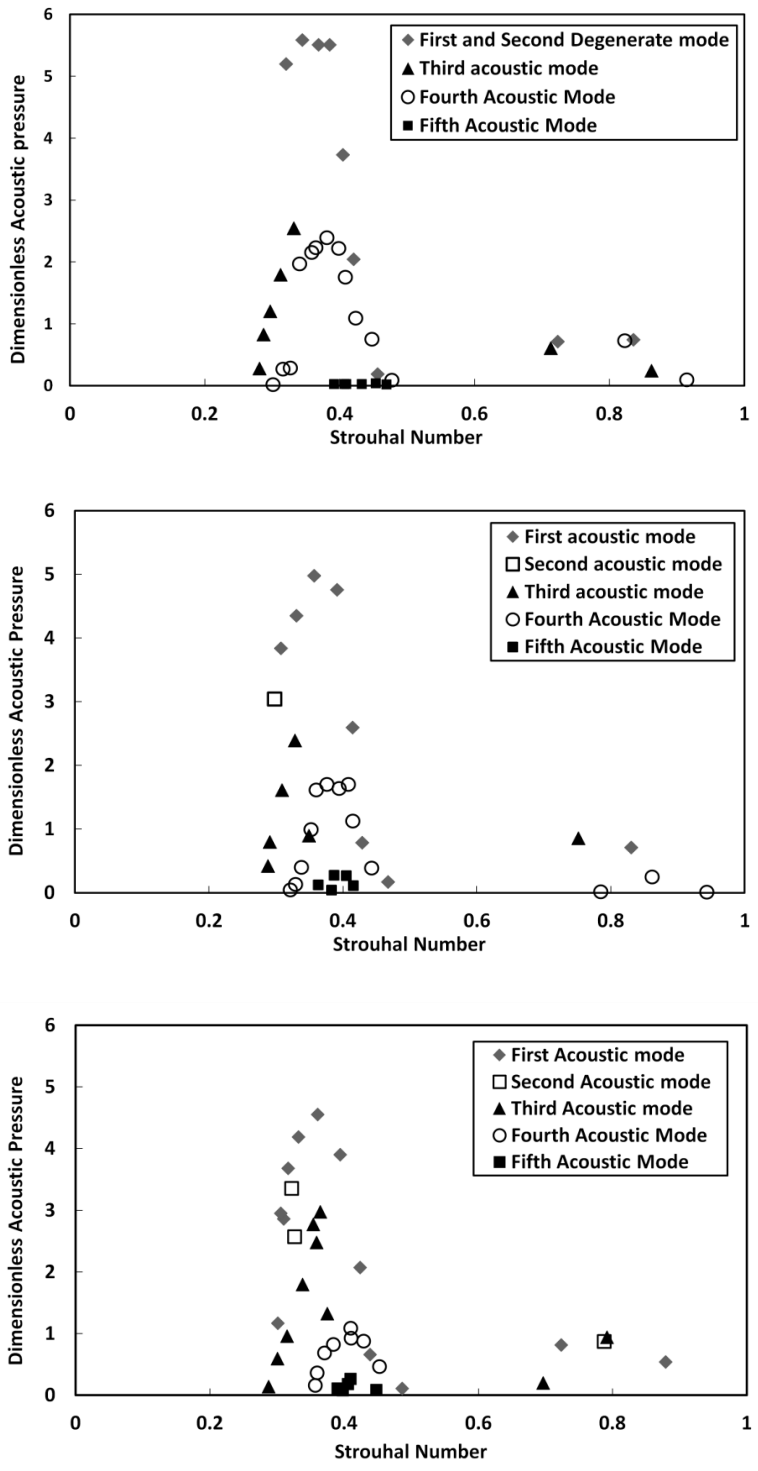

Figure A-6: Dimensionless Acoustic Pressure vs. Strouhal Number Top=*W/H*=1, Middle=W/H=0.95, Bottom=W/H=0.9 cavities

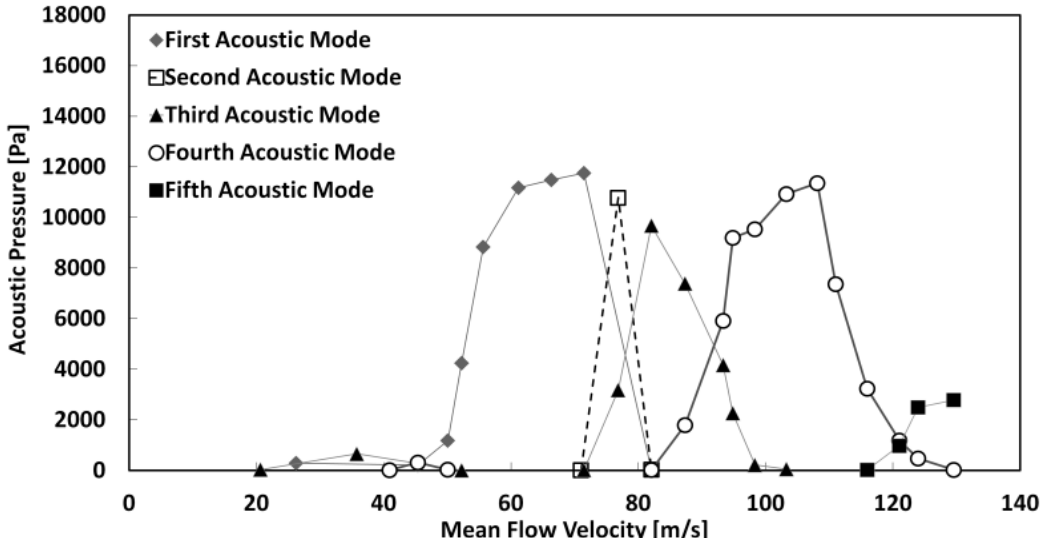

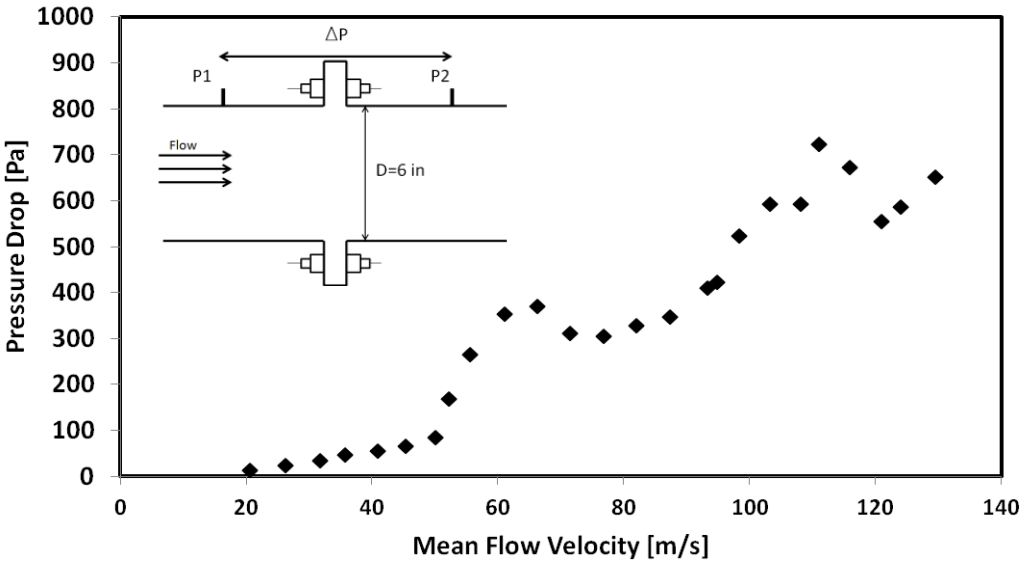

Figure A-7: Pressure drop for the rectangular cavity with W/H=0.95

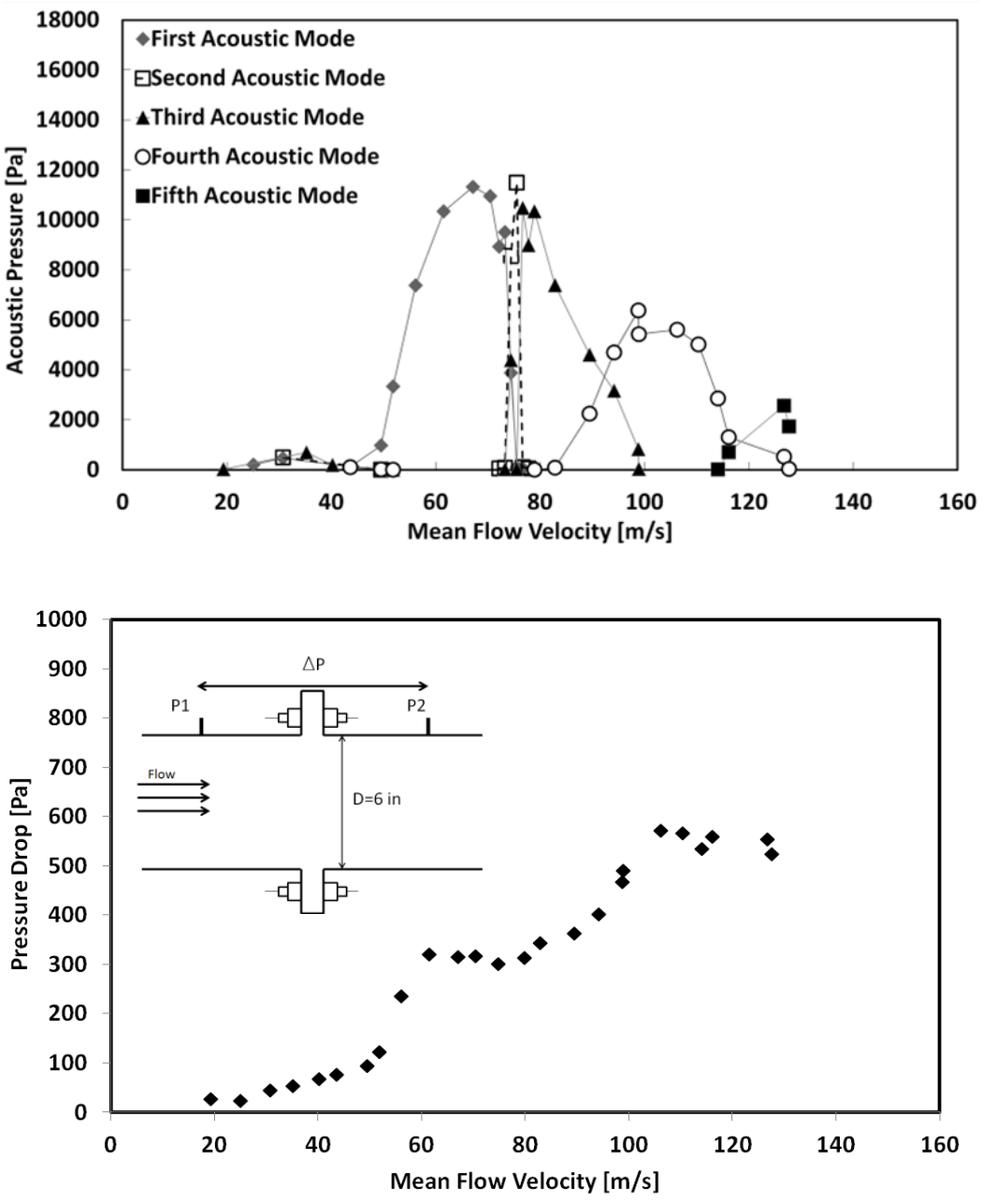

Figure A-8: Pressure drop for the rectangular cavity with W/H=0.90

APPENDIX B
UNCERTAINTY ANALYSIS

Acoustic Measurements

The frequency and recorded acoustic pressure of the strongly excited acoustic modes remained constant throughout their averaging. The acoustic measurements were obtained with a National Instruments NI-9233 data acquisition card accompanied with an anti-aliasing filter. As previously discussed, the excitation of the acoustic modes was found to be intermittent only at low flow velocities. To account for the intermittency, a sampling rate of 25kHz consisting of a conservative average of fifty, 1 second long, samples with a final resolution of δf=± 1Hz was utilized. Those measurements taken during the strong tonal excitation from the first shear layer mode had little influence from varying the number of samples that were averaged.

The uncertainty in the acoustic pressure measurement is due to the uncertainty in the calibration of the pressure transducers, ≈4%, the uncertainty in the repeatability of the acoustic pressure measurements is found to be around ≈5.2%, and the resolution of the pressure transducers around ≈4.8%. To account for these associated uncertainties, the quadratic sum method, detailed below in equation B-1, was utilized obtaining an uncertainty in acoustic pressure of ≈8.0%.

$$\delta R = \sqrt{\delta x_1{}^2 + \delta x_2{}^2 + \delta x_3{}^2 + .. + \delta x_n{}^2} \qquad \text{(B-1)}$$

Mean Flow Velocity

The uncertainty propagation of random uncertainties was resolved through the method proposed by Kline & McClintock (1953), Equation B-2. δR is the

uncertainty of the dependent variable and δX_i represents the uncertainty of the separate associated independent variables.

$$\delta R = \sqrt{\sum_{i=1}^{n} \left(\frac{\partial R}{\partial X_i}\delta X_i\right)^2} \tag{B-2}$$

The mean flow velocity was measured through a pitot-tube situated at the bell-mouth. The dynamic pressure was recorded using a differential pressure transducer calibrated with a Crystal pressure calibrator with a resolution accuracy of $\pm$ 5Pa, leading to an uncertainty of $\approx 2\%$. Utilizing Kline and McClintock's method, Equation B-3 is obtained. Thus, the mean flow velocity uncertainty through calibration is around 1.0%

$$\frac{\delta \mathrm{P}}{\mathrm{P}} = \sqrt{\left(\frac{2\delta U}{U}\right)^2} \tag{B-3}$$

The relative standard deviation (RSD),$\frac{\sigma}{U}$, in response of average reading of the pitot tube was found to be around $\approx$ 1.0%. Thus, the overall uncertainty of the mean flow velocity is around 1.5%

Dimensionless Numbers

From Kline and McClintock's method, the uncertainty of dimensionless parameters utilized within this study is evaluated. First, the uncertainty of the dimensionless acoustic pressure, $P^* = \frac{P}{0.5\rho U^2}$, is represented as a function of both acoustic pressure and mean flow velocity as represented in B-4.

$$\delta P^* = \sqrt{\left(\frac{\partial P^*}{\partial P}\delta P\right)^2 + \left(\frac{\partial P^*}{\partial U}\delta U\right)^2} \tag{B-4}$$

$$\frac{\delta P^*}{P^*} = \sqrt{\left(\frac{\delta P^*}{P}\right)^2 + \left(\frac{2\delta U}{U}\right)^2} \tag{B-5}$$

It can be demonstrated that the associated uncertainty of the dimensionless acoustic pressure may be represented as B-5. Utilizing the previous values of acoustic pressure and mean flow velocity, the uncertainty of the dimensionless acoustic pressure is around 8.5%.

Likewise, the uncertainty of the Strouhal Number, $St = \frac{fL}{U}$, may be represented by the uncertainty of its independent variables as shown below.

$$\delta St = \sqrt{\left(\frac{\partial St}{\partial L}\delta L\right)^2 + \left(\frac{\partial St}{\partial f}\delta f\right)^2 + \left(\frac{\partial St}{\partial U}\delta U\right)^2} \quad \text{(B-6)}$$

$$\frac{\delta St}{St} = \sqrt{\left(\frac{\delta L}{L}\right)^2 + \left(\frac{\delta f}{f}\right)^2 + \left(\frac{\delta U}{U}\right)^2} \quad \text{(B-7)}$$

Through additional measurements along the cavity perimeter, the tolerance in the cavity length, L, was 1% .The resolution of the acoustic measurements was δf=1Hz. Thus, the smallest resonant frequency, 851Hz, results in the largest $\frac{\delta f}{f}$ of 0.1%. This leads to an overall uncertainty of $\frac{\delta St}{St}$ is 1.8%.

Laser Doppler Velocimetry

Laser Doppler Velocimetry was utilized to resolve the radial velocity profile situated one pipe diameter upstream from the cavity mouth at both resonance and pre-resonance conditions. The measurements consisted of using a traverse with a minimum step size of 0.00625mm. Measurements were taken at intervals as small as 0.1mm.

The reproducibility of the measurements on the pre-resonance condition illustrated that the coefficient of variability ($\frac{\sigma}{U}$) of the mean flow past the boundary layer thickness was 1.0% through four reproduced tests. The smallest measured distance from the wall was 1mm. Those distances closer to the wall have significant velocity gradients and a lack of measured seeded particles.

Flow Visualization Uncertainty

The objective of these measurements was not to obtain a full quantitative representation of the three-dimensional flow field, but to visualize the downstream propagation of disturbances at specific circumferential sections along the shear layer and compare it to the distinct acoustic modal behaviours that were being observed. The phase-averaged measurements consisted of triggering the PIV along the acoustic cycle of the investigated mode. The sampling frequency was the maximum available from the NI-9233 data acquisition card at 50 kHz, resulting in a resolution of $2.0xE^{-5}$s.

The finite resolution introduces an uncertainty through triggering at specific phases of the acoustic cycle. The uncertainty is dependent on the resonant frequency and the relative size of its oscillation period to the sampling rate. From all measurements, the largest uncertainty coincides to the smallest period of the fourth acoustic mode with a maximum deviation of 5.34°. A conservative number of instantaneous images, 250-300, were taken at each phase to reduce this error through averaging.